

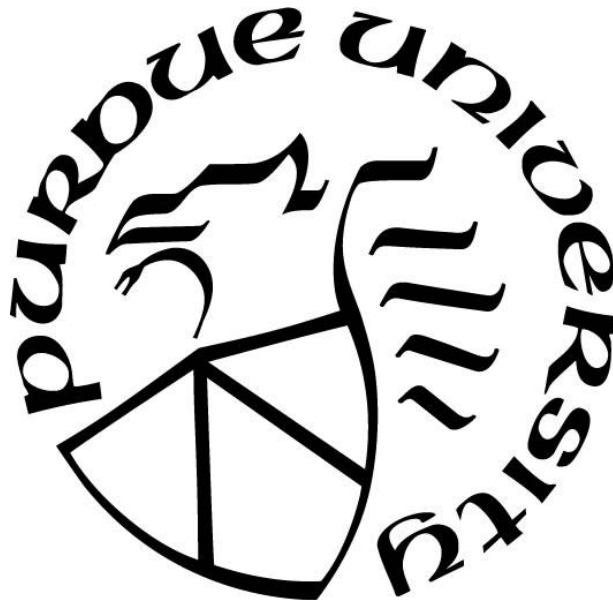
**THERMOMECHANICAL MEASUREMENTS OF ZIRCALOY-4:  
APPLICATION OF RAMAN THERMOMETRY AND NANO-  
MECHANICAL TESTING TECHNIQUES**

by  
**Hao Wang**

**A Dissertation**

*Submitted to the Faculty of Purdue University  
In Partial Fulfillment of the Requirements for the degree of*

**Doctor of Philosophy**



School of Aeronautics & Astronautics

West Lafayette, Indiana

December 2019

**THE PURDUE UNIVERSITY GRADUATE SCHOOL  
STATEMENT OF COMMITTEE APPROVAL**

**Dr. Vikas Tomar, Chair**

School of Aeronautics and Astronautics

**Dr. Maria A. Okuniewski**

School of Materials Engineering

**Dr. Gary J. Cheng**

School of Industrial Engineering

**Dr. Tyler N. Tallman**

School of Aeronautics and Astronautics

**Dr. Daniel Schwen**

Idaho National Laboratory

**Approved by:**

Dr. Gregory Blaisdell

*Dedicated to  
my parents  
and  
my wife*

## ACKNOWLEDGMENTS

First and foremost I would like to thank Dr. Vikas Tomar for his continuous guidance and support through this research. It has been an honor for me to work with him as a Ph.D. student. Prof. Tomar is an outstanding mentor. His patience, adamant work ethic, and inspiring nature have been a great source of motivation throughout my doctoral research. Without his guidance and persistent help, this dissertation would not be possible.

I am also thankful to Dr. Maria Okuniewski for her continued support throughout my Ph.D. study. She has personally guided me through the extremely time consuming material characterizations. I have been extremely lucky to have her as one of my supervisors who cared so much about my work.

I would also like to sincerely thank Dr. Daniel Schwen, Dr. Gary Cheng and Dr. Tyler Tallman for consenting to serve as my committee members. A special thanks to Dr. Daniel Schwen for his critical advises of my work during my preliminary examination, which helped me tremendously in improving my research.

The help and encouragement from my friends and colleagues are greatly appreciated as well. I would like to thank all of my past and current lab mates in the Interfacial Multiphysics Laboratory: Dr. Devendra Verma, Dr. Yang Zhang, Dr. Sudipta Biswas, Dr. Chandra Parakash, Debapriya Pinaki, Bing Li, Abhijeet Dhiman, and Ayotomi Olokun. The time spent with everyone made it an incredible experience, and provided me with many great friendships. I would also like to thank my frineds Dr. Jun-li Lin, Dr. Weicheng Zhong, Dr. Keyou Mao, and Jonova Thomas for their great help in technical discussions and experiments.

Last but not least, I would like to thank my parents and my wife. Thank you for encouraging me in all of my pursuits and inspiring me to follow my dreams. I always knew that you believed in me and wanted the best for me.

# TABLE OF CONTENTS

LIST OF TABLES .....	8
LIST OF FIGURES .....	9
ABSTRACT .....	12
INTRODUCTION .....	13
CHAPTER 1. MICROSTRUCTURE DEPENDENT THERMAL CONDUCTIVITY MEASUREMENT OF ZIRCALOY-4 USING AN EXTENDED RAMAN THERMOMETRY METHOD .....	15
1.1 Introduction.....	16
1.2 Material and Methods .....	17
1.2.1 Sample Preparation.....	17
1.2.2 Experimental Setup.....	19
1.2.3 Heat Transfer Model.....	20
1.2.4 Experiment Calibration.....	24
1.2.4.1 Correlation between Raman Peak Shift and Temperature.....	24
1.2.4.2 Laser Spot Size Determination .....	25
1.2.4.3 Laser Power Absorbed by Samples .....	27
1.3 Results.....	28
1.3.1 Microstructure Characterization .....	28
1.3.2 Elastic Modulus Distribution.....	31
1.3.3 Thermal Conductivity Distribution.....	32
1.4 Discussion.....	33
1.5 Conclusion .....	38
1.6 References.....	39
CHAPTER 2. CONSTITUTIVE MODELING OF ZIRCALOY HYDRIDE BASED ON STRAIN RATE DEPENDENT NANOINDENTATION AND NANO-SCALE IMPACT DATASET .....	45
2.1 Introduction.....	46
2.2 Experimental Setup.....	48
2.2.1 Sample Preparation.....	48

2.2.2	Nano-indentation Experiments .....	51
2.2.3	Nano-scale Impact Experiment.....	54
2.2.4	Indenter Tip Geometry .....	56
2.3	Numerical Method .....	57
2.3.1	Finite Element Model For Nanoindentation .....	57
2.3.2	Iteration Algorithm .....	59
2.3.3	Viscoplastic Power Law Model.....	60
2.3.4	Finite Element Model For Hydride Cracking.....	61
2.4	Results and Analyses .....	62
2.4.1	Elastic Modulus And Nanoindentation Hardness.....	62
2.4.2	Correction For Plastic Stress-Strain Curve.....	64
2.4.3	Power Law Model Fitting.....	65
2.4.4	FEM Simulation For Hydride Cracking .....	67
2.5	Discussion.....	69
2.6	Conclusions.....	70
2.7	References.....	72
CHAPTER 3. AMAGE MODELING OF HYDRIDED STRUCTURE BASED ON EXTENDED GURSON-TVERGAARD-NEEDLEMAN MODEL .....		79
3.1	Introduction.....	80
3.2	Model Description .....	81
3.2.1	Pressure Dependent Plasticity Model .....	81
3.2.2	Return Mapping Algorithm and Numerical Integration .....	82
3.2.3	Derivation of The Consistent Tangent Moduli.....	85
3.2.4	GTN Yield Function And Internal State Variables .....	88
3.2.5	Damage Description of Hydrided Structure .....	89
3.3	GTN UMAT Validation.....	90
3.3.1	A Single Plane Strain Element Under Tensile Loading .....	91
3.3.2	A 3D Cubic Element Under Tensile.....	93
3.4	Application of The Model.....	94
3.4.1	Axial Tensile Test.....	94
3.4.2	Ring Compression Test.....	98

3.5	Conclusions.....	103
3.6	References.....	104
	CHAPTER 4. CONCLUSION.....	108
	CHAPTER 5. FUTURE WORKS.....	110
	APPENDIX A. PARTIAL DERIVATIVES FOR GTN MODEL .....	111
	APPENDIX B. COEFFICIENTS FOR EQUATIONS (83) AND (84).....	113
	APPENDIX C. COEFFICIENTS FOR EQUATIONS (98) AND (99).....	115
	APPENDIX D. COEFFICIENTS FOR EQUATIONS (100) AND (101) .....	116
	PUBLICATIONS.....	117

## LIST OF TABLES

Table 1. Laser parameters for each sample.....	26
Table 2. Mean true spacing of platelets and basketweave laths in LIGs from samples 1 and 2... 31	31
Table 3. Elastic modulus in selected LIGs.....	32
Table 4. Thermal conductivity in selected LIGs.....	33
Table 5. Crystallographic orientation induced anisotropy in phonon thermal conductivity [55].	38
Table 6. Chemical composition of the as-received zircaloy 4 samples. ....	48
Table 7. Indenter geometry parameters .....	57
Table 8. A comparison of elastic modulus and nano-hardness of $\delta$ -hydride reported in literatures. .....	64
Table 9. Viscoplastic material parameters for $\delta$ -hydride.....	67
Table 10. Model parameters used for calibrations.....	92
Table 11. Model parameters used for axial tensile test and ring compression test ( $C_H$ is the hydrogen content in wppm). ....	97

## LIST OF FIGURES

Figure 1. (a) Dimension of the zircaloy sample; (b) photo of zircaloy sample, (c) SEM image of silicon coating surface around the notch tip, (d) SEM image of silicon coating at the sample edge with a thickness measured as 951nm.....	18
Figure 2. (a) Schematic of the setup of nanoindentation tests; (b) schematic diagram of nanoindentation and Raman thermometry scanning schedule; (c) schematic setup of Raman thermometry platform.....	20
Figure 3. Schematic of the thin film with a thick substrate in the cylindrical coordinate system.	20
Figure 4. (a) The DIP hot stage for calibration tests. (b) Linear correlation between temperature and Raman shift shift for the silicon coated zircaloy sample. ....	25
Figure 5. (a) Curve fittings to determine the laser spot size. (b) Schematic of the method to determine the laser absorbed power on the sample surface, laser power measurement points are numbered as 1-5.....	26
Figure 6. (a)-(b) BSE micrograph of specimen 1 and 2, respectively. (c)-(d) The processed images for identification of LIGs of specimen 1 and 2, respectively. (e)-(f) LIGs overlaid on the micrographs in (a, b), with labels for selected grains in samples 1 and 2 whose mean true spacing is tabulated in Table 2.....	30
Figure 7. Elastic modulus contour plot of (a) sample1, (b) sample2, indicating the specific regions measured via nanoindentation tests. Note that the LIGs identified with black lines in (a) and (b) correspond to those previously identified in the BSE micrographs in Figure 6.....	31
Figure 8. (a) Thermal conductivity contour plot of (a) sample 1 (b) and sample 2, indicating the specific regions measured via Raman thermometry. Note that the LIGs identified with black lines in (a) and (b) correspond to those previously identified in the BSE micrographs in Figure 6. ....	32
Figure 9. Correlation between mechanical and thermal properties in selected LIGs: (a) elastic modulus vs. mean true spacing, (b) thermal conductivity vs. mean true spacing.....	34
Figure 10. (a) BSE micrographs on sample 1. (b) EDS mapping of Fe element in the selected area.....	35
Figure 11. (a) Comparison between experimental measurements and Kapitza model prediction on the correlation of thermal conductivity and grain size, (b) thermal conductivity vs. average elastic modulus in selected LIGs. ....	37
Figure 12. (a) Dimensions of the zircaloy-4 sample, (b) SEM back-scattered electrons image of the as-received zircaloy microstructure. ....	49
Figure 13. Optical microscope images of the hydrided zircaloy-4 sample, (a) the cross-section of a hydrided zircaloy-4 sample, (b) hydride morphology near the Ni coating surface, (c) near-surface high-density hydride rim/blister layer, (d) uniformly distributed hydrides in the zircaloy-4 matrix; (e)-(f) EBSD orientation map and phase fraction map of the hydride rim/blister layer,	

(g)-(h) EBSD orientation map and phase fraction map of the zircaloy matrix with individual hydride precipitates. ....	50
Figure 14. (a) The nanoindentation platform inside a purge chamber, (b) schematic of the high temperature nanoindentation setup, (c) analysis of the indentation size effect on hydride at RT, (d) representative indentation curves on hydride at different temperatures. ....	52
Figure 15. (a) The linear regression analysis for the zero load/displacement correction, (b) comparison of indentation stress-strain curve without and with the zero load/displacement correction. ....	54
Figure 16. (a) The nanoindentation and nano-scale impact setup, (b) representative indenter displacement (blue curve) and velocity (red curve) history from a nano-scale impact test. ....	55
Figure 17. (a) SEM image of the indenter tip with a radius of 0.7 $\mu\text{m}$ . (b) Theoretical model of a conical indenter with a worn spherical tip [56]. ....	56
Figure 18. (a) Geometry and boundary conditions for the nanoindentation FEM model. (b) Stress (GPa) distribution during a nanoindentation test. (c) Plastic strain field during a nanoindentation test. ....	58
Figure 19. (a) Geometry and boundary conditions for the hydride cracking FEM model. (b) Stress field (kPa) induced by isotropic misfit strain distribution, (c) equivalent plastic strain field induced by isotropic misfit strain distribution. ....	62
Figure 20. Material properties of $\delta$ -hydride under different temperatures: (a) elastic modulus, (b) nanoindentation hardness (left axis) and yield stress (right axis). ....	63
Figure 21. 150°C experimental data and analysis, (a) nanoindentation load-displacement curve with mean (black curve) and variations (red shadow) of $\delta$ -hydride, (b) nanoindentation stress-strain curve of $\delta$ -hydride, (c) evolution of load-displacement curves during iterations, (d) evolution of plastic stress-strain curves during iterations. ....	65
Figure 22. Linear fitting process to determine parameters for the power law model: (a) nanoindentation data, (b) nano-scale impact data, (c) $\text{Log}(A)$ vs. $\text{Log}(\epsilon)$ . (d) The strength coefficient $K$ as a function of temperature, (e) the strain hardening exponent as a function of temperature, (f) the strain rate exponent $m$ as a function of temperature. ....	66
Figure 23. (a) Stress-strain response of $\delta$ -hydride at RT (black), 150°C (blue), and 300°C (red), (b) experimental and simulated load-displacement curves at different temperatures. ....	67
Figure 24. (a) Relation between fracture strength and hydride length at room temperature, (b) fracture strength of hydride at elevated temperatures, (c) global tensile strain at hydride cracking under elevated temperatures. ....	68
Figure 25. (a) Yield stress vs. temperature, (b) strain energy ratio vs. temperature. ....	70
Figure 26. (a) A 2D plane strain element under the uniaxial tensile test, (b) the von Mises stress as a function of strain in Y direction, (c) the void volume fraction as a function of strain in Y direction. ....	92

Figure 27. (a) A 3D cubic element used for the hydrostatic tensile test, (b) the von Mises stress as a function of strain in Y direction, (c) the void volume fraction as a function of strain in Y direction. ....	94
Figure 28. (a) Dimensions of the axial tensile specimen, (b) mesh of the FEM model, (c) comparison of stress-strain curves between experimental results and FEM predictions.....	95
Figure 29. Distribution of total void volume fraction at different stages (mid-plane cross-section of the tensile specimen): (a) crack initiation in the center of specimen, (b) crack propagation, (c) final failure.....	96
Figure 30. (a) comparison between total void volume fraction and porosity induce by hydride cracking at final failure, (b) hydride cracking porosity as a function of the distance from fracture surface (1200 wppm), (c) width reduction at the failure surface as a function of hydrogen concentration in the specimen.....	97
Figure 31. Details of the ring compression test model: (a) geometry of the specimen, (b) mesh of the specimen, (c) boundary conditions. ....	98
Figure 32. (a) Ring compression test device and specimen, (b) pressure distribution in the specimen during a ring compression test (mirror display from half ring model). ....	99
Figure 33. Normalized load–displacement curve of zircaloy-4 ring compression tests with circumferential hydrides at room temperature.....	100
Figure 34. Fracture of a hydrided zircaloy-4 specimen with low hydrogen content after ring compression tests, (a) ductile deformation with cracks at horizontal spots, (b) hydride morphology and crack development at different spots [35]. ....	100
Figure 35. FEM predicted crack profile for a specimen with hydrogen concentration of 300 wppm, the crack initiates on the outer surface at spot 1. ....	101
Figure 36. Fracture of a hydrided zircaloy-4 specimen with high hydrogen concentration after ring compression tests, (a) brittle fracture with cracks at vertical spots, (b) hydride morphology and crack development at different spots [35]. ....	102
Figure 37. FEM predicted crack profile for a specimen with hydrogen concentration of 500 wppm, crack initiate on the inner surface at spot 2 and 4.....	102
Figure 38. (a) FEM model and points selected for pressure ratio analysis, (b) the pressure ratio ( $P_2/P_1$ ) as a function of the displacement. ....	103

## ABSTRACT

Zirconium alloys (zircaloy) have been widely used in light water reactors due to their good thermomechanical properties, corrosion resistance, and low thermal neutron absorption rate. As one of the most important safety barriers, cladding is not only used to encapsulate nuclear fuel, but also to prevent the nuclear fission products from leaking into the coolant. During the operation of nuclear reactors, hydride will form in zircaloy and significantly degrade the tensile strength, ductility, fracture toughness, and creep behavior of the cladding, and eventually leading to the failure of cladding. Therefore, understanding the material properties of zircaloy and its hydrides is crucial to the safety of power plants. In this study, the mechanical Raman spectroscopy and nano-mechanical testing techniques were used to perform thermomechanical measurements and damage analysis of zircaloy-4. The Raman thermometry method was used to measure localized spatially resolved thermal conductivity and establish the potential linkage of microstructure to thermal and mechanical properties of zircaloy-4. The local thermal conductivity values showed to increase with increase in grain size. Nanoindentation and nano-scale impact techniques were used to obtain the viscoplastic constitutive relation of hydrides at elevated temperatures. Based on the obtained viscoplastic model, fracture strength of hydrides was predicted by using finite element method (FEM) simulations. An extended Gurson-Tvergaard-Needleman (GTN) model was used to study the macro-scale fracture behavior of hydrided zircaloy-4 structures. Good agreement between calculated and experimental results was obtained for various boundary conditions.

## INTRODUCTION

Zirconium alloys (zircaloy) have been widely used in light water reactors due to their good thermomechanical properties, corrosion resistance, and low thermal neutron absorption rate. As one of the most important safety barriers, cladding is not only used to encapsulate nuclear fuel, but also to prevent the nuclear fission products from leaking into the coolant. In normal reactor operations, the temperature in cladding is stabilized around 300°C. While, during transient events in reactor operations, the temperature of cladding increases rapidly up to 600°C. During the dry cask storage period, the cladding temperature remains above 200°C for decades. Moreover, during the operation of nuclear reactors, hydride will form in zircaloy cladding and significantly degrade the tensile strength, ductility, fracture toughness, and creep behavior of the cladding, and eventually leading to the failure of the structure. Therefore, understanding the material properties of zircaloy and its hydride is crucial to the safety of power plants. In this study, the mechanical Raman spectroscopy and nano-mechanical testing techniques were used to perform thermomechanical measurements and damage analysis of zircaloy-4.

Chapter 1 details the experiments that were conducted on two polycrystalline zircaloy-4 samples to obtain the microstructural dependence of thermal conductivity. The experiments were performed on a novel Raman spectroscopy platform. By introducing a thin silicon coating on the sample surface, the Raman thermometry method was extended to perform thermal conductivity measurements on a metallic sample. A heat transfer model was derived to relate the substrate thermal conductivity to the laser induced temperature increase on the thin film surface. Combining this heat transfer model with the Raman thermometry method, experiments were performed to measure localized spatially resolved thermal conductivity and establish the potential linkage of microstructure to thermal and mechanical properties of zircaloy-4 samples .

Chapter 2 details an experimental method to obtain the viscoplastic relation of  $\delta$ -hydrides. nanoindentation and nano-scale impact techniques were used to obtain the constitutive relation of  $\delta$ -hydrides at elevated temperatures. To prevent oxidation effects on the sample surface and the indenter tip, the purge chamber was filled with nitrogen gas during all high temperature experiments. FEM simulations with an iterative algorithm were used to determine the plastic stress-strain curves of  $\delta$ -hydride. Then a power law viscoplastic model was fitted to the data in order to describe the elastoplastic response of  $\delta$ -hydride. Based on the global tensile fracture

stress reported by Shi et al., the fracture strength of hydride was predicted by using FEM simulations. The ductile to brittle transition of the hydrided zircaloy structure has also been studied.

Chapter 3 details a modified Gurson-Tvergaard-Needleman model for fracture analysis of hydrided zircaloy structures. The model accounts the damage effects from both precipitate debonding in zircaloy matrix and hydride cracking. ABAQUS user defined subroutines UMAT was used to implement the extended GTN model into ABAQUS/Standard. Axial tensile tests and ring compression tests were studied by using 3D FEM simulations. The simulations satisfactorily reproduced experimental load-displacement curves. Furthermore, the model successfully predicted the width reduction and the hydride cracking porosity at the fracture surface in axial tensile tests. Good agreement between calculated and experimental results was also achieved for crack initiation prediction in ring compression tests.

Chapter 4 and 5 summarize the key findings of this work along with future recommendations.

**CHAPTER 1.**  
**MICROSTRUCTURE DEPENDENT THERMAL CONDUCTIVITY**  
**MEASUREMENT OF ZIRCALOY-4 USING AN EXTENDED RAMAN**  
**THERMOMETRY METHOD**

Hao Wang<sup>a</sup>, Jonova Thomas<sup>b</sup>, Maria A. Okuniewski<sup>b</sup>, Vikas Tomar<sup>a,\*</sup>

<sup>a</sup> School of Aeronautics and Astronautics, Purdue University-IN, 47907, USA

<sup>b</sup> School of Materials Engineering, Purdue University-IN, 47907, USA

\*Corresponding author, Phone: (765)-494-3006 Fax: (765) 494-0307 Email: tomar@purdue.edu

Manuscript Under Preparation.

**Abstract**

In this work, microstructural dependence of thermal conductivity of two polycrystalline zircaloy-4 samples was analyzed by using an extended Raman thermometry method. The thermal conductivity value was found to range from 11-13 Wm<sup>-1</sup>K<sup>-1</sup> for the analyzed samples. The local thermal conductivity values showed decrease with grain size decreasing. Thermal resistance from grain boundaries and inhomogeneous composition are identified as two potential contributors to the thermal conductivity suppression. The Kapitza thermal resistance model is shown to describe the measured dependence trend of thermal conductivity on grain size variation. Nanoindentations were performed to obtain the local elastic modulus for the analyzed samples. The thermal conductivity increases with elastic modulus increasing in each sample. Such result indicates a possibility that at room temperature phonon thermal conductivity makes an unneglectable contribution to the total thermal conductivity in zircaloy-4.

**Keywords:** Raman spectroscopy, Zircaloy-4, microstructure, thermal conductivity.

## 1.1 Introduction

Zirconium alloys (zircalloys) have been widely used in light water reactors due to their good thermomechanical properties, corrosion resistance, and low thermal neutron absorption rate [1]. Zircaloy cladding encapsulates nuclear fuels to prevent the nuclear fission products from leaking into the coolant [1]. In normal reactor operations, the temperature in cladding is stabilized around 300°C. While, during the transient events, the temperature of cladding increases rapidly up to 600°C. During the dry cask storage period, the cladding temperature remains above 200°C for decades. Therefore, understanding the material properties of zircaloy is crucial to the safety of power plants. Although thermal properties of zircaloy have been studied extensively during the past few decades [2-8], there are still some aspects that remain unknown, such as the relationship between the microstructure and local thermomechanical properties. The current research focuses on studying the microstructure dependence of thermal conductivity of zircaloy-4.

Typically, there are two types of thermal conductivity measurement techniques, steady state methods (comparative technique, radial heat flow method, parallel conductance method, and electrical heating methods) and transient methods (transient plane source method, laser flash method,  $3\omega$  method, and hot-wire method) [9, 10]. Due to the limitations of these experimental techniques, thermal conductivity is usually reported as an averaged effective value over the entire measured domain [10]. Recently, researchers used the spatially resolved time-domain thermoreflectance (TDTR) method to study the localized thermal conductivity in polycrystalline diamond [11]. TDTR is based on the monitoring of acoustic waves that are generated by the thermal strain induced by a pulsed laser. However, TDTR is applied notably to thin film materials (up to hundreds of nanometers thick). In this work, a novel extended Raman thermometry method is used to measure the thermal conductivity distribution at site specific locations in bulk specimens to provide a precise assessment on the localized thermal conductivity rather than an averaged value. The Raman thermometry was established by Perichon *et al.* [12] in 1999 and has been used broadly in thermal conductivity measurements, [13-22]. In comparison to other thermal conductivity measurement methods, Raman thermometry has multiple advantages including that not only it is a noncontact and nondestructive method, in addition it only requires a short time for data collection. The spatial resolution is typically a few microns, which makes it suitable for measurements of localized material properties. In a typical Raman thermometry measurement, a local temperature increase

is induced by laser heating effect. Based on the relationship between temperature and the Raman peak shift, [23, 24], local temperature information can be captured by a Raman thermometry camera. Thereafter, by using a proper heat transfer model, the thermal conductivity value can be obtained from the local temperature [25]. Besides being used on traditional solid samples, this method can also be extended to suspended nanowires [20], suspended membranes [14, 26, 27], and thin film samples [15, 18, 28].

The Raman spectroscopy method is not only used in thermal conductivity measurements, but also in stress distribution investigations. This technique is based on the Raman Stokes peak position which can be changed by both local stress and local temperature, while the line width broadening is only affected by the surface temperature. It provides a possible way to separate stress and thermal effects apart from Raman measurements. This method was first used by Abel et al.[13], while studying the temperature distribution of a micron-sized polycrystalline silicon beam with external loading. They showed that by utilizing the Raman technique both the stress and thermal affects could be separated, within a range of uncertainty [13]. Beechem et al. [29] measured the stress distribution in polycrystalline silicon by using the Raman Stokes peak shift and the temperature distribution by using Raman Stokes line width.

In this work, the Raman thermometry method was extended to perform thermal conductivity measurement on metallic samples by coating a thin silicon layer on the sample surface. A heat transfer model was derived to relate the substrate thermal conductivity to the laser induced temperature increase on the thin film surface. Combining this heat transfer model with the Raman thermometry method, experiments were performed to measure localized spatially resolved thermal conductivity and establish the potential linkage of microstructure to thermal and mechanical properties of zircaloy-4 samples.

## **1.2 Material and Methods**

### **1.2.1 Sample Preparation**

A cold-worked stress-relieved (CWSR) zircaloy-4 disk with a thickness of 1.5 mm was obtained from American Elements. According to the ASTM D5045 standard for three-point bending tests, the dimensions of the sample are shown in Figure 1 (a). Electrical discharge machining was used to machine specimens from the zircaloy-4 bulk material. A representative

specimen image is shown in Figure 1 (b). In order to reduce the roughness of the sample surface, mechanical polishing with 600, 1000, and 1200 grade SiC paper was first performed. Then samples were polished by using 1  $\mu\text{m}$  SiC suspension. Finally, as the finishing step, vibratory polisher with 0.05  $\mu\text{m}$  colloidal silica suspension solution were used to obtain satisfactory sample surface condition. An array of nanoindentations were performed around the notch tip to obtain local mechanical properties. To obtain the Raman signal, a thin silicon layer ( $\sim 1 \mu\text{m}$ ) was coated on the polished surface by using the chemical vapor deposition technique. Figure 1 (c) shows a scanning electron microscope (SEM) image of the silicon coating around the notch tip area on a zircaloy sample. Figure 1 (d) shows a SEM image of the silicon coating at the sample edge. The thickness of the silicon coating is measured as 951.3 nm, which is very close to the designed thickness ( $\sim 1 \mu\text{m}$ ).

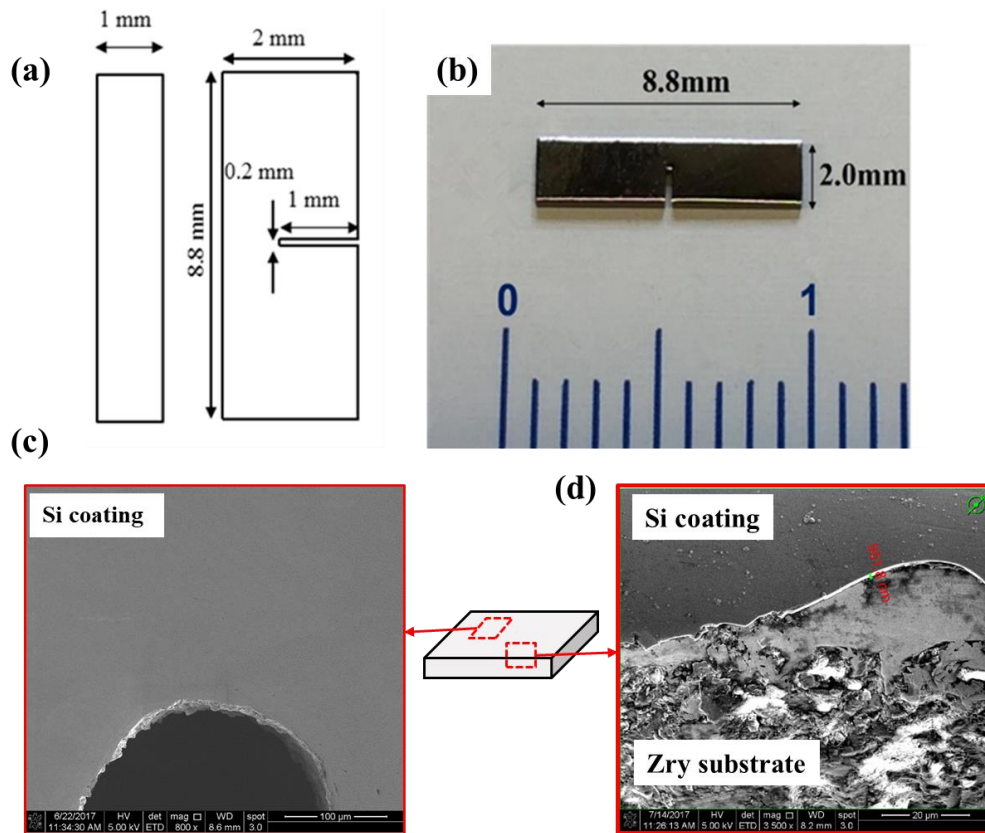


Figure 1. (a) Dimension of the zircaloy sample; (b) photo of zircaloy sample, (c) SEM image of silicon coating surface around the notch tip, (d) SEM image of silicon coating at the sample edge with a thickness measured as 951nm

Experimental procedure involves the following steps:

- (1) performing nanoindentation tests to analyze the microstructural dependence of the elastic modulus; and
- (2) performing load independent thermometry measurements to analyze the microstructural dependence of the thermal conductivity.

### 1.2.2 Experimental Setup

A multi-functional Nanotest platform from Micro Materials Ltd. [30-32] was used to perform all nanoindentation experiments. A schematic of the setup is shown in Figure 2 (a). During indentations, a calibrated electromagnetic coil was used to control the indentation load with a resolution of 1  $\mu\text{N}$ . The displacement of the indenter was recorded by measuring the voltage change of a capacitive transducer with a resolution of 0.01 nm. A Berkovich type diamond indenter was used to perform all nanoindentation tests. The indentation area ( $500\ \mu\text{m}\times 350\ \mu\text{m}$ ) is located around the notch tip of the zircaloy specimen, which is shown in Figure 2 (b). The spacing between indentations is 50  $\mu\text{m}$ . Samples were loaded to a peak load of 50 mN at a loading/unloading rate of 2.5 mN/s. The dwell time at peak load was selected as 5 s. The Young's modulus was obtained by using the Oliver and Pharr method to analyze the indentation load-depth curves [33].

Figure 2 (c) shows the experimental setup of the Raman thermometry. The sample was fixed on a three-dimensional (3-D) controllable platform. The platform also has a dual in-line package (DIP) hot stage to perform high temperature experiments. The laser used in this experiment is an Ar<sup>+</sup> laser with 514.5 nm wavelength (Modu-Laser, Inc., UT). The laser beam travelled through a single mode fiber, a collimator, a dichromic mirror, and finally was focused by a  $\times 40$  objective onto the sample surface. The reflected laser was collected by a spectrometer (Acton SP2500, Princeton Instruments, Inc., NJ) for further Raman peak shift analysis. The scanning area ( $500\ \mu\text{m}\times 350\ \mu\text{m}$ ) of the Raman thermometry test overlaps with the nanoindentation tests, as shown in Figure 2 (b). The spacing between scanning points is also 50  $\mu\text{m}$ .

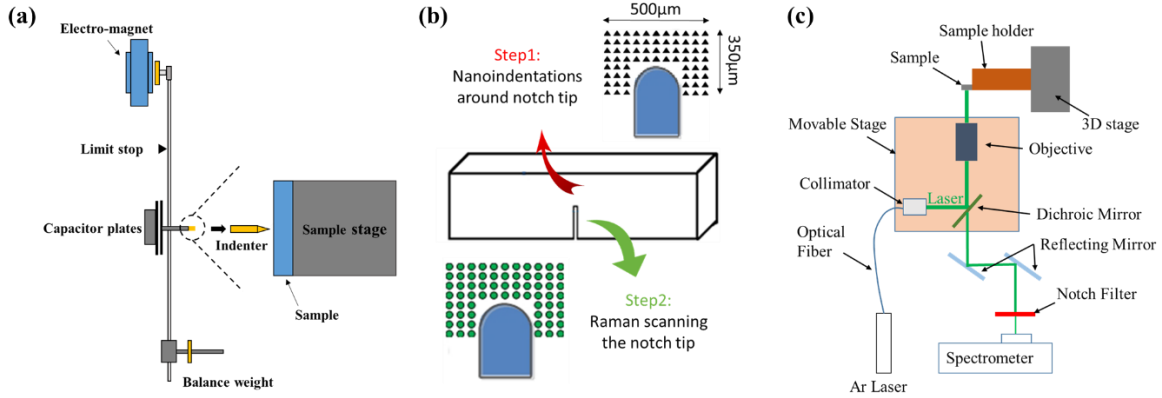


Figure 2. (a) Schematic of the setup of nanoindentation tests; (b) schematic diagram of nanoindentation and Raman thermometry scanning schedule; (c) schematic setup of Raman thermometry platform.

### 1.2.3 Heat Transfer Model

As discussed in the introduction, the Raman thermometry can only provide temperature information on the sample surface. Therefore, a proper correlation between the coating surface temperature rise and the substrate thermal conductivity needs to be established. Based on previous researches [16, 34], the heat transfer model for a thick substrate with a thin film was derived. In this case, the thickness of the substrate (1mm) is a thousand times larger than the coating layer thickness (1 $\mu$ m), thus the substrate can be treated as an infinite half-plane.

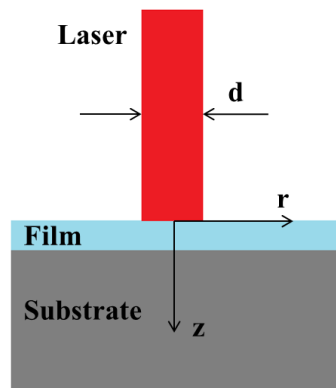


Figure 3. Schematic of the thin film with a thick substrate in the cylindrical coordinate system.

Two heat transfer equations can be used for this thin film and thick substrate structure:

$$\frac{\partial t_f(r, z)}{\partial r^2} + \frac{1}{r} \frac{\partial t_f(r, z)}{\partial r} + \frac{\partial^2 t_f(r, z)}{\partial z^2} = 0, \quad (1)$$

$$\frac{\partial t_s(r, z)}{\partial r^2} + \frac{1}{r} \frac{\partial t_s(r, z)}{\partial r} + \frac{\partial^2 t_s(r, z)}{\partial z^2} = 0, \quad (2)$$

where  $t_f$  is the film temperature,  $t_s$  is the substrate temperature, and  $r$  is the radial distance. The local temperature value can be normalized by using relation  $t(r, z) = T(r, z) - T_0$ , where  $T$  and  $T_0$  are the local temperature and the far field temperature (which can be considered as environmental temperature), respectively. Therefore,  $t(r, z)$  represents the local temperature increase due to the focused laser beam. By enforcing the continuity condition of heat flow and temperature at the interface between the substrate and the film, boundary conditions can be given as:

$$t_f(r, z) = t_s(r, z) \quad \text{at } z = \delta, \quad (3)$$

$$K_f \frac{\partial t_f(r, z)}{\partial z} = K_s \frac{\partial t_s(r, z)}{\partial z} \quad \text{at } z = \delta, \quad (4)$$

$$K_f \frac{\partial t_f(r, z)}{\partial z} = -f(r) \quad \text{at } z = 0 \quad \text{and } 0 < r < d/2. \quad (5)$$

Here,  $\delta$  is the thickness of the thin film,  $K_f$  is the thermal conductivity of the film, and  $K_s$  is the thermal conductivity of the substrate. Equation (3) represents the temperature continuity at the interface; Eq. (4) represents the heat flow continuity at the interface; and Eq. (5) represents the laser beam energy distribution on the thin film. A Gaussian function is used for the laser beam intensity distribution, which is described as,

$$f(r) = \frac{2P}{\pi R_0^2} \exp\left(-\frac{2r^2}{R_0^2}\right). \quad (6)$$

In Eq. (6),  $f(r)$  is the intensity distribution of the laser beam as a function of radial distance  $r$ ,  $R_0$  is the laser beam radius, and  $P$  is the power of the laser beam. These equations can be solved by using the Hankel transform. Taking the Hankel transform of the order zero to Eq. (1)-(5) leads to following equations,

$$\frac{d^2 T_f(\xi, z)}{dz} - \xi^2 T_f(\xi, z) = 0, \quad (7)$$

$$\frac{d^2 T_s(\xi, z)}{dz} - \xi^2 T_s(\xi, z) = 0. \quad (8)$$

The boundary conditions after transformation can be defined as,

$$T_f(\xi, \delta) = T_f(\xi, \delta), \quad (9)$$

$$K_f \frac{\partial T_f(r, \delta)}{\partial z} = K_s \frac{\partial T_s(r, \delta)}{\partial z}, \quad (10)$$

$$K_f \frac{\partial T_f(r, \delta)}{\partial z} = -\frac{P}{2\pi} \exp\left(-\frac{R_0^2 \xi^2}{8}\right). \quad (11)$$

For these transformed equations, the solutions will be in the following format,

$$T_f(\xi, z) = A(\xi)e^{\xi z} + B(\xi)e^{-\xi z}, \quad (12)$$

$$T_s(\xi, z) = C(\xi)e^{-\xi z}, \quad (13)$$

In Eq. (12),  $A(\xi)$  and  $B(\xi)$  are two coefficients which can be solved as,

$$A(\xi) = \frac{P}{2\pi K_f \xi} \frac{(K_f - K_s) \exp(-R_0^2 \xi^2 / 8)}{[K_s - K_f + \exp(2\xi\delta)(K_f + K_s)]}, \quad (14)$$

$$B(\xi) = \frac{P}{2\pi K_f \xi} \frac{(K_f + K_s) e^{2\xi\delta} \exp(-R_0^2 \xi^2 / 8)}{[K_s - K_f + \exp(2\xi\delta)(K_f + K_s)]}. \quad (15)$$

Substituting Eq. (14) and (15) into Eq. (12),

$$T_f(\xi, z) = \frac{P}{2\pi K_f \xi} \frac{\exp(-R_0^2 \xi^2 / 8)}{[K_s - K_f + \exp(2\xi\delta)(K_f + K_s)]} [(K_f - K_s)e^{\xi z} + (K_f + K_s)e^{-\xi z} e^{2\xi\delta}]. \quad (16)$$

By using the inverse Hankel transform, the temperature distribution on the film surface can be found as,

$$t_f(r, 0) = \int_0^\infty \xi T_f(\xi, 0) J_0(\xi r) d\xi. \quad (17)$$

In Eq. (17),  $J_0 = (ξr)$  is the Bessel function of zero order. The laser spot average temperature ( $\bar{t}$ ) can be calculated by integrating Eq. (17) over the laser spot area,

$$\begin{aligned}
\bar{t} &= \frac{1}{\pi R_0^2} \int_0^{R_0} t_f(r, 0) \cdot 2\pi r \cdot dr \\
&= \frac{2}{R_0^2} \int_0^\infty \xi \cdot T_f(\xi, 0) \int_0^{R_0} J_0(\xi r) \cdot r \cdot dr d\xi \\
&= \frac{2}{R_0} \int_0^\infty T_f(\xi, 0) \cdot J_1(\xi R_0) \cdot d\xi \\
&= \frac{PK_f}{R_0\pi(K_f + K_s)} \int_0^\infty \frac{\frac{K_f - K_s}{K_f + K_s} + \exp\left(-\frac{2\delta}{R_0}\lambda\right)}{\lambda\left(\frac{K_s - K_f}{K_f + K_s} + \exp\left(-\frac{2\delta}{R_0}\lambda\right)\right)} \exp\left(-\frac{\lambda^2}{8}\right) \cdot J_1(\lambda) \cdot d\lambda
\end{aligned} \tag{18}$$

In Eq. (18),  $\lambda = R_0\xi$ . The natural heat convection coefficient between sample and the surrounding air also needs to be considered [15]. In this setup, the sample can be simplified as a plane and the surrounding air flow can be considered as laminar flow. Then the Rayleigh number is,

$$Ra_L = \frac{g\beta\bar{t}L^3}{\alpha\nu}. \tag{19}$$

In Eq. (19),  $g$  is the gravity acceleration,  $\beta$  is the air thermal expansion coefficient,  $L$  is the sample height,  $\nu$  is the air kinematic viscosity, and  $\alpha$  is the air thermal diffusivity. The Nusselt number and the natural heat convection coefficient are given as,

$$\bar{Nu}_L = 0.68 + \frac{0.67Ra_L^{1/4}}{[1 + (0.492/Pr)^{9/16}]^{4/9}}, \tag{20}$$

$$\bar{h} = \bar{Nu}_L(\kappa_{air}/2R_0). \tag{21}$$

In Eq. (20) and (21),  $k_{\text{air}}$  is the air thermal conductivity which equals to  $0.0265 \text{ Wm}^{-1}\text{K}^{-1}$ . After considering the air convection contribution during the heat transfer process, the Eq. (18) can be modified as [15],

$$\tilde{\tau} = \frac{Pk_f[I_0(1) + I_1(1)]}{\sqrt{2\pi}R_0e(K_f + K_s)(\delta\bar{h}/K_f + 1)}, \quad (22)$$

In Eq. (22),  $I_0(1)$  is the zero-order modified Bessel function,  $I_1(1)$  is the first-order modified Bessel function, and  $\bar{h}$  is the natural heat convection coefficient. The thermal conductivity of an amorphous silicon thin film ( $K_f$ ) is reported as about  $2 \text{ Wm}^{-1}\text{K}^{-1}$  [35].  $R_0$  and  $P$  are the laser spot size and the sample absorbed laser power, respectively, which need to be calibrated in experiments. The desired thermal conductivity  $k_s$  can be obtained by solving Eq. (22).

## 1.2.4 Experiment Calibration

### 1.2.4.1 Correlation between Raman Peak Shift and Temperature

Calibrating the correlation between the Raman peak shift and the temperature is important for the Raman thermometry method to obtain temperature information on a sample surface. To achieve this, a test sample was mounted on the DIP hot stage to perform calibration runs at different temperatures. Figure 4 (a) shows a schematic of the DIP hot stage setup. The sample was fixed on the hot stage by using high temperature glue. The sample was heated to the desired experimental temperature by using thermocouples. The power of thermocouples was controlled by a feedback circuit to stable sample temperature at the target value. Calibration temperatures were selected based on the limitation of the coating technique. Temperatures higher than  $200^\circ\text{C}$  will cause delamination of the silicon layer. Therefore, the calibration temperature range was varied from  $20^\circ\text{C}$  to  $180^\circ\text{C}$  in increments of  $40^\circ\text{C}$ . During each temperature exposure, fifteen different points on the sample surface were scanned to measure the Raman Stokes peak. In this case, low laser power must be used to make sure the laser beam does not induce a detectable local temperature increase on the sample surface. Researchers reported this low laser power for silicon and silicon dioxide film Raman tests to be about  $1.1 \text{ mW}$  [15, 16]. In current tests, the laser with  $0.7 \text{ mW}$  power level was selected, which is the lowest power level achievable with a available Raman signal. Figure 4 (b) shows the temperature dependent Raman peak shift

relationship, demonstrating a linear trend. After the linear fitting process, the relationship was determined as,

$$\Delta\omega = 489.781 - 3.2 \times 10^{-3}T. \quad (23)$$

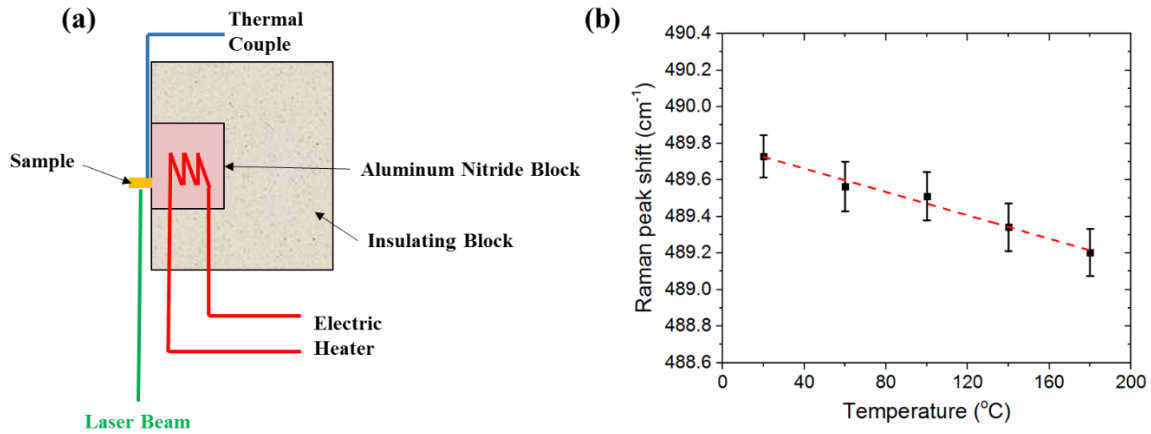


Figure 4. (a) The DIP hot stage for calibration tests. (b) Linear correlation between temperature and Raman shift shift for the silicon coated zircaloy sample.

#### 1.2.4.2 Laser Spot Size Determination

According to the wavelength of the laser and the numerical aperture of the objective lens, the theoretical spot diameter is calculated to be 966 nm. Nevertheless, in real practice, there are many other factors also influence the laser spot size, such as the surface quality of samples and the focusing distance. Therefore, the laser spot size is different from sample to sample; it needs to be measured for each case. Here, the laser spot size was determined by using the cleaved edge method [26]. First, the laser beam was focused on the sample surface near an edge. Then, the sample was moved slowly at a speed of 1  $\mu\text{m/s}$ , allowing the laser to scan across the edge. The sample moving distance and reflected laser intensity were both recorded simultaneously.

The laser intensity profile was fitted by using the Boltzmann equation (given in Eq. (24)). Differentiating the Boltzmann equation with respect to the sample moving distance leads to the changing rate of the reflected laser power (given in Eq. (25)). Then, the Gaussian peak function, Eq. (26), was used to fit the laser spot profile. The diameter of the laser spot was considered as

the full width at half maximum (FWHM) of the Gaussian peak function fitting result. A typical laser spot profile is shown in Figure 5 (a). The spot size determination was performed on each sample, the results are detailed in Table 1.

$$y = \frac{A_1 - A_2}{1 + e^{(x-x_0)/dx}} + A_2, \quad (24)$$

$$y' = (A_2 - A_1) \frac{e^{(x-x_0)/dx}}{(1 + e^{(x-x_0)/dx})^2 dx}, \quad (25)$$

$$y = y_0 + \frac{A \times \exp\left(\frac{-4 \ln(2) (x - x_c)^2}{w^2}\right)}{w\sqrt{\pi/4\ln(2)}}. \quad (26)$$

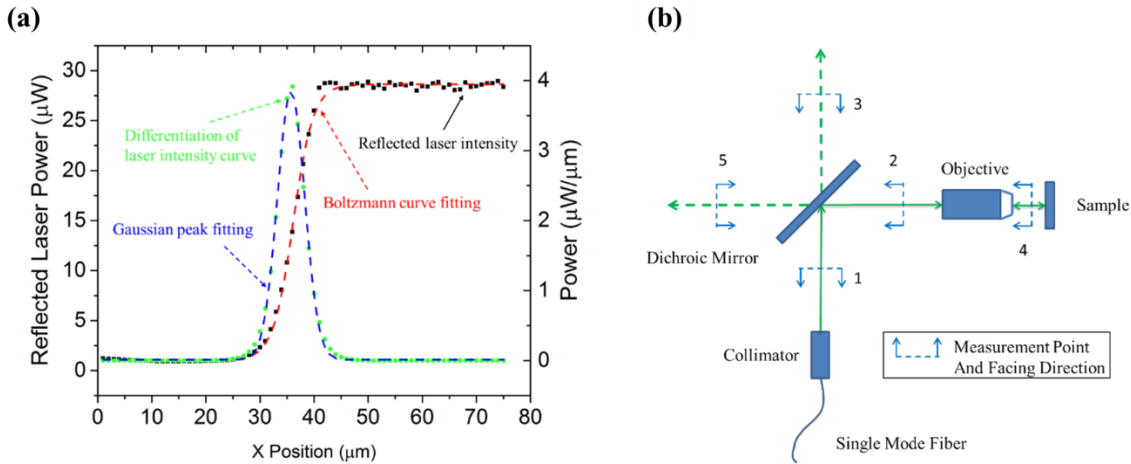


Figure 5. (a) Curve fittings to determine the laser spot size. (b) Schematic of the method to determine the laser absorbed power on the sample surface, laser power measurement points are numbered as 1-5.

Table 1. Laser parameters for each sample.

	Sample 1	Sample 2
Laser spot radius (μm)	2.3	2.5
Absorbed laser power (mW)	8.3	8.4

### 1.2.4.3 Laser Power Absorbed by Samples

The laser power absorbed by the sample cannot be measured directly. Therefore, an indirect measurement method was developed by previous researchers [22, 36]. It assumes that optical devices in the laser path have a constant energy dissipation ratio with respect to the incident laser power. Then the absorbed laser power can be calculated based on the laser power measured at five different points along the laser path. Figure 5 (b) shows the laser path and measurement locations. The laser power was measured by using a power meter (S140C+PM100USB, Thorlabs, Inc., NJ) at these locations. The laser intensity is denoted by  $I_i$ , where  $i$  represents the measurement location. The total laser intensity generated was measured as  $I_1$ . Most of the incoming laser power was reflected by the dichroic mirror; measured as  $I_2$ . A small portion ( $I_3$ ) of laser was not reflected by the dichroic mirror, rather it went through the mirror and was dissipated in the air.  $I_4$  denotes the laser power coming from the objective, and it was also the total laser power being delivered onto the sample surface. Then, most of the laser was absorbed or reflected by the sample. The reflected laser travelled back through the objective and dichroic mirror, and was measured as  $I_5$ . Based on the assumption that the dissipation ratio of the laser power through dichroic mirror and objective remains the same, following relationships can be defined:

$$I_4^R = I_4 - I_s, \quad (27)$$

$$I_2^R = \frac{I_4}{I_2} \times I_4^R, \quad (28)$$

$$I_5 = \frac{I_3}{I_1} \times I_2^R. \quad (29)$$

$$I_5 = I_4 - \frac{I_1 \times I_2 \times I_5}{I_3 \times I_4}. \quad (30)$$

In above equations,  $I_s$  denotes the sample absorbed laser power, which is the desired quantity. The superscript ‘R’ refers to reflection.  $I_2^R$  and  $I_4^R$  are the reflected laser intensity at points 2 and 4, respectively. These values cannot be measured directly, they can only be estimated according to above relations. Combining above equations and solving for  $I_s$  gives Eq. (30), which can be used to estimate the sample absorbed laser power. The absorbed laser power for each sample is detailed in Table 1.

## 1.3 Results

### 1.3.1 Microstructure Characterization

Figure 6 (a, b) show the backscattered electron (BSE) micrographs of samples that were subjected to Raman thermometry tests. Both platelet and basketweave grain morphologies are observed in the samples [37]. Grains comprising a collection of laths in a specific direction (platelets) are observed to have varying widths. In this study, grains that have several laths in a parallel direction (platelets) and grains with a basketweave morphology are collectively categorized as large individual grains (LIGs). Categorizing them in this fashion helps to determine the correlation between local grain microstructure and local material properties. Figure 6 (c, d) show the processed micrographs of Figure 6 (a, b), respectively. Various image processing tools such as image addition/subtraction, Gaussian blurring, and thresholding available in ImageJ [38] were used to provide an enhanced edge contrast to the microstructure. The raw BSE micrographs were first Gaussian blurred with a radius of 2 pixels and then subsequently subtracted from the raw micrographs. Therefore, the newly produced processed micrographs only indicate the edges of grain boundaries enhanced with a greater contrast. The processed micrographs are then thresholded to set the edges of the enhanced grain boundary pixels at a value of 255 and the remainder at 0. The processed micrographs presented in Figure 6 (c, d) therefore provide a visual assistance for manual categorization of LIGs in Figure 6 (e, f). The quantity of LIGs determined via visual assessment of samples 1 and 2 are 17 and 35, respectively.

A more detailed analysis of the spacing between platelets or individual basketweave laths is determined via a quantitative stereological assessment of the grains. If the platelets and lath morphologies from various grains are assumed to represent a similar microstructure to that of idealized lamellar phases in grains, then the total number of features by totaling length  $N_L$ , mean random spacing  $\sigma_r$ , and mean true spacing  $\sigma_t$  between laths from various grains can be determined by using Eqs. (31) and (32), respectively [39].

$$\sigma_r = \frac{1}{N_L}, \quad (31)$$

$$\sigma_t = 0.5 * \sigma_r. \quad (32)$$

From above equations, sample 1 ( $\sigma_t = 4.45 \pm 0.96\mu\text{m}$ ) has a slightly larger mean true spacing between laths in LIGs than sample 2 ( $\sigma_t = 3.47 \pm 1.32\mu\text{m}$ ). Previous researchers have shown that the lath size in zircaloy-4 can vary from  $1\mu\text{m}$  to  $7\mu\text{m}$ , based on variations in the cooling rate from the  $\beta$ -phase [40]. Several grains with large areas and clear lath structures on each sample were selected for further thermal conductivity analysis. The selected grains are numbered in Figure 6 (e, f). The mean true spacing in the selected grains are listed in Table 2.

In sample 1, most LIGs have parallel platelet structures with mean true spacing around  $4\mu\text{m}$ . While, in grain 4 of sample 1 the basketweave structure is coarser with a mean true spacing of  $6.3\mu\text{m}$ . In sample 2, most grains have fine parallel platelet structures with mean true spacing ranging from  $2\sim 4\mu\text{m}$ . Grain 1 has a coarse basketweave structure with a mean true spacing of  $5.5\mu\text{m}$ . Grains 4 and 6 have a basketweave grain structure with a mean true spacing of  $5.46\mu\text{m}$  and  $5.78\mu\text{m}$ , respectively. Therefore, selected grains can be grouped based on their mean true spacing. Typically, it can be observed in these two samples that grains with a mean true spacing under  $5\mu\text{m}$  have fine platelet structures. While grains with a mean true spacing greater than  $5\mu\text{m}$  may have different lath structures, i.e. either a coarse platelet structure or a basketweave structure.

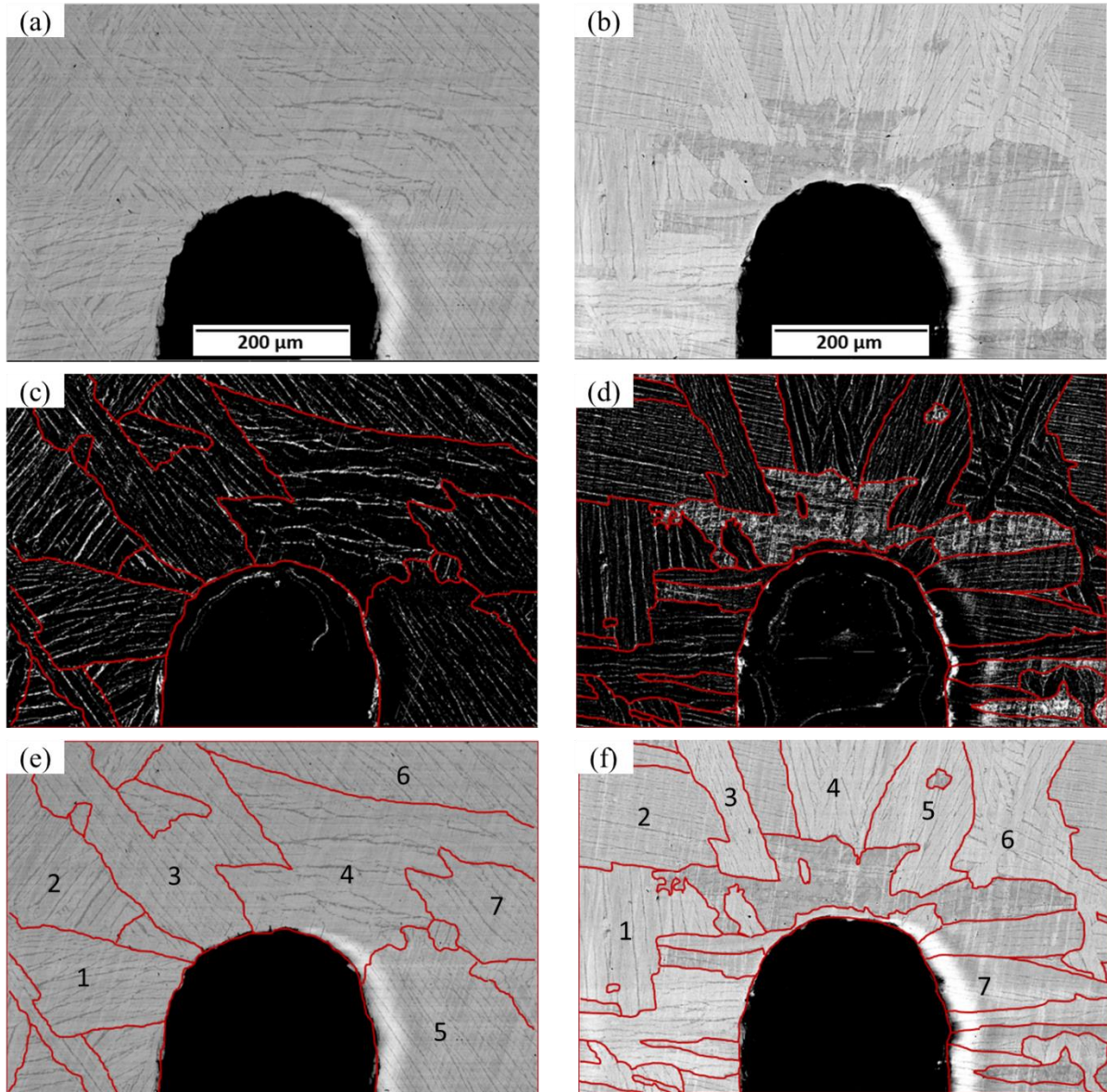


Figure 6. (a)-(b) BSE micrograph of specimen 1 and 2, respectively. (c)-(d) The processed images for identification of LIGs of specimen 1 and 2, respectively. (e)-(f) LIGs overlaid on the micrographs in (a, b), with labels for selected grains in samples 1 and 2 whose mean true spacing is tabulated in Table 2.

Table 2. Mean true spacing of platelets and basketweave laths in LIGs from samples 1 and 2.

	Mean True Spacing ( $\mu\text{m}$ )						
	Grain 1	Grain 2	Grain 3	Grain 4	Grain 5	Grain 6	Grain 7
Sample 1	3.99 $\pm$ 0.15	4.36 $\pm$ 0.23	3.34 $\pm$ 0.25	6.30 $\pm$ 0.36	3.59 $\pm$ 0.14	3.99 $\pm$ 0.13	3.92 $\pm$ 0.33
Sample 2	5.50 $\pm$ 0.57	2.35 $\pm$ 0.24	2.29 $\pm$ 0.32	5.46 $\pm$ 0.75	3.36 $\pm$ 0.32	5.78 $\pm$ 0.61	3.75 $\pm$ 0.49

### 1.3.2 Elastic Modulus Distribution

Figure 7 (a, b) depict the nanoindentation obtained elastic modulus contour plots and the corresponding LIG partitions (intercepted from the BSE micrographs in Figure 6) for both samples. Taking the average of all 70 measurement points, the average elastic moduli are 77.6 GPa and 80.3 GPa for samples 1 and 2, respectively. These values match well with the literature reported elastic modulus of zircaloy-4 as 80 $\pm$ 6.4GPa [41]. The larger LIG size in sample 1 leads to a more homogeneous elastic modulus. The average elastic modulus values in each LIG are detailed in Table 3. The grain numbering corresponds directly to Figure 7. Since grain 7 in sample 1 only contains two measurement points, it has been omitted in Table 3.

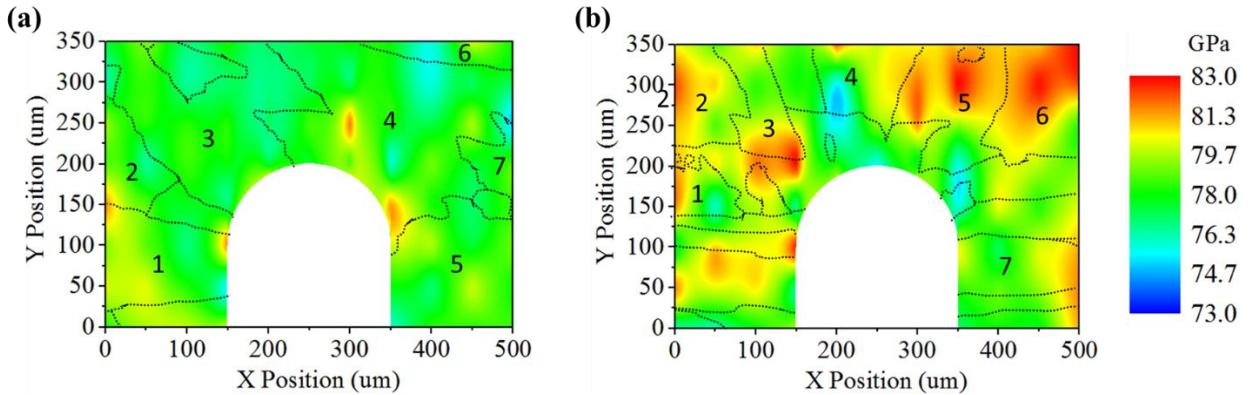


Figure 7. Elastic modulus contour plot of (a) sample1, (b) sample2, indicating the specific regions measured via nanoindentation tests. Note that the LIGs identified with black lines in (a) and (b) correspond to those previously identified in the BSE micrographs in Figure 6.

Table 3. Elastic modulus in selected LIGs.

	Elastic Modulus (GPa)						
	Grain 1	Grain 2	Grain 3	Grain 4	Grain 5	Grain 6	Grain 7
Sample 1	78.80±1.86	78.52±1.61	77.73±0.79	78.31±1.31	77.95±1.13	77.21±1.24	-
Sample 2	80.28±2.70	80.33±2.07	80.15±1.49	78.98±3.44	81.23±3.10	82.38±2.21	80.18±2.31

### 1.3.3 Thermal Conductivity Distribution

Figure 8 shows the room temperature Raman thermometry obtained thermal conductivity contour plots and the corresponding grain partitions (intercepted from the BSE micrographs in Figure 6) for both samples. Taking the average of all 70 measurement points, thermal conductivity values are  $12.2 \text{ Wm}^{-1}\text{K}^{-1}$  and  $11.5 \text{ Wm}^{-1}\text{K}^{-1}$  for sample 1 and sample 2, respectively. These values are very close to the values reported by other researchers [3-6, 42-44] ranging from  $12\sim 15 \text{ Wm}^{-1}\text{K}^{-1}$  for both zircaloy-2 and zircaloy-4. The small difference might be due to the thermal resistance at the interface between the silicon coating and the substrate. As shown in Figure 8, the thermal conductivity is not identical around the notch tip area. Generally, grain boundaries are considered as an obstacle for heat transmission, which is known as the Kapitza resistance [45, 46]. Therefore, regions with larger grains are expected to have relatively higher thermal conductivity values, due to a lower grain boundary (GB) fractional coverage. The average thermal conductivity values in selected LIGs are listed in Table 4.

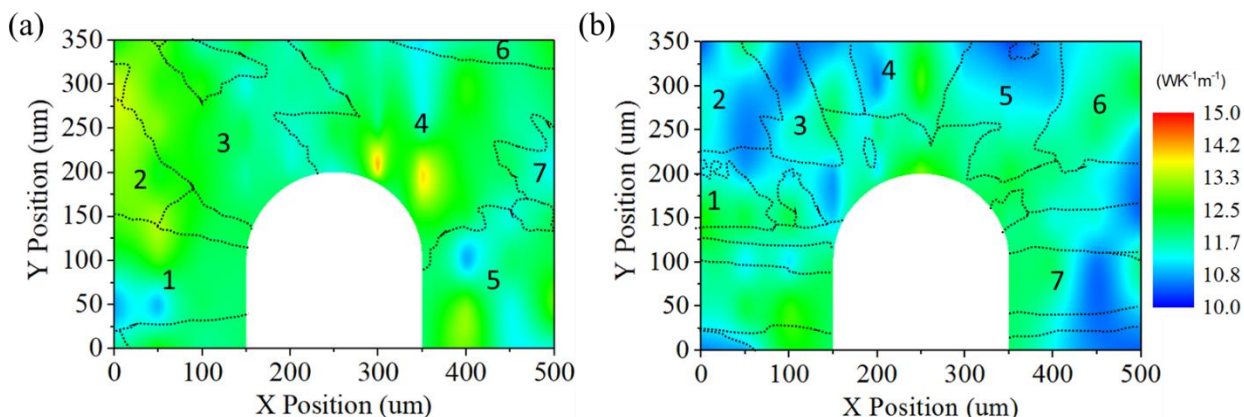


Figure 8. (a) Thermal conductivity contour plot of (a) sample 1 (b) and sample 2, indicating the specific regions measured via Raman thermometry. Note that the LIGs identified with black lines in (a) and (b) correspond to those previously identified in the BSE micrographs in Figure 6.

Table 4. Thermal conductivity in selected LIGs.

	Thermal Conductivity ( $\text{Wm}^{-1}\text{K}^{-1}$ )						
	Grain 1	Grain 2	Grain 3	Grain 4	Grain 5	Grain 6	Grain 7
Sample 1	11.84±0.61	12.2±0.34	12.14±0.46	12.08±0.69	11.94±0.76	11.81±0.48	-
Sample 2	11.96±0.53	11.21±0.41	11.34±0.43	11.59±0.70	11.37±0.39	11.58±0.41	11.27±0.58

#### 1.4 Discussion

One goal of this research is to establish the potential linkage of microstructure to localized thermal and mechanical properties in zircaloy-4. Utilizing the spatial mapping of the elastic modulus in Figure 7 and the thermal conductivity in Figure 8, connections to the microstructure are examined. Figure 9 (a) depicts the correlation between the mean true spacing and elastic modulus in selected LIGs based on the data summarized in Table 2 and Table 3. As shown, the elastic modulus does not show a clear dependence on the mean true spacing in selected LIGs. Experimental measurements have shown that the grain size can affect the elastic modulus of nanocrystalline metallic materials [47, 48]. The variation of elastic modulus may be attributed to the large volume fraction of atoms that are located at interfaces and/or surfaces and porosity [49, 50]. However, such grain size induced elastic modulus variation only happens in nanocrystalline materials. Especially when the volume fraction of the interfaces or/and surfaces becomes comparable to the volume fraction of the crystals. Considering the mean true spacing (2~7  $\mu\text{m}$ ) in current examined zircaloy samples, the grain size effects on the elastic modulus is neglectable. Figure 9 (b) depicts the correlation between the mean true spacing and average thermal conductivity in selected LIGs based on the data summarized in Table 2 and Table 4. As shown in Figure 9 (b), LIGs with larger mean true spacing have slightly higher thermal conductivity values.

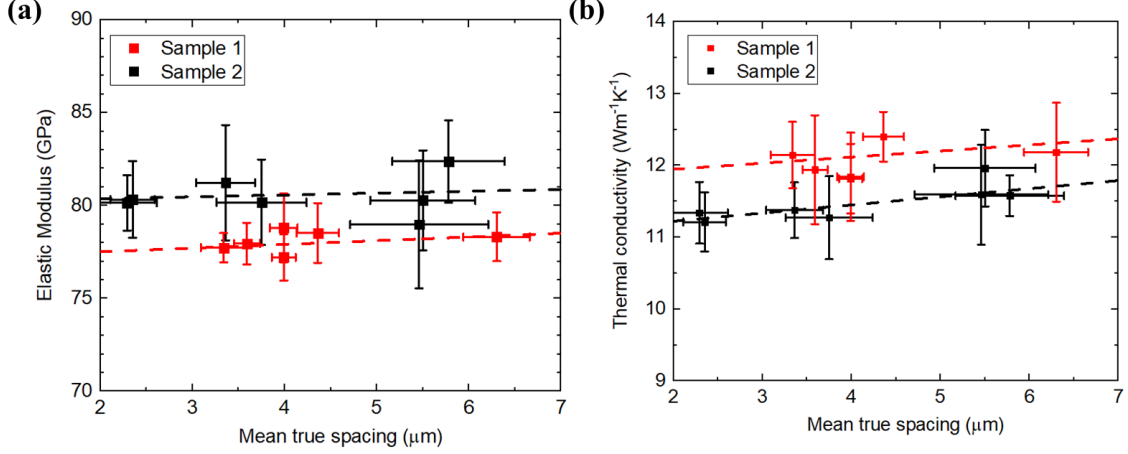


Figure 9. Correlation between mechanical and thermal properties in selected LIGs: (a) elastic modulus vs. mean true spacing, (b) thermal conductivity vs. mean true spacing.

According to the classical kinetic model, the thermal conductivity from both electrons and phonon can be expressed as the same form [51],

$$k = \frac{1}{3} C v \lambda \quad (33)$$

In Eq. (33),  $C$  is the specific heat per unit volume from electron/phonon,  $v$  is the average electron/phonon group velocity, and  $\lambda$  is the electron/phonon mean free path (MFP). In general, the local MFP for the heat carriers can be written following the Matthiessen's rule, given in Eq. (34),

$$\lambda_{\text{loc}} = [\lambda_{\text{bulk}}^{-1} + \lambda_{\text{def}}^{-1} + \lambda_{\text{GB}}^{-1}]^{-1}. \quad (34)$$

In Eq. (34),  $\lambda_{\text{bulk}}$  corresponds to the scattering between heat carriers in a bulk crystal,  $\lambda_{\text{def}}$  corresponds to the heat carrier scattering at defects such as impurities and dislocations, and  $\lambda_{\text{GB}}$  corresponds to the heat carrier scattering at GB. According to Eq. (34), there are two plausible contributors for the variation of local thermal conductivity. The first one is the inhomogeneous composition and impurity distribution, which leads to a decrease of electron and phonon MFPs. The second contributor is the thermal resistance induced by GBs. LIGs with smaller mean true spacing have closer GBs, thereby blocking free electrons and phonon waves [52]. Energy dispersive X-ray spectroscopy (EDS) was used to investigate elemental distribution within the sample. Figure 10 (a, b) show a BSE micrograph and the corresponding EDS map indicated by

the red box. The EDS results highlight the elemental distribution of Fe, indicating a significant enrichment along grain boundaries. Other elements (Ca, Zr, Cr, Ni, Cu, Zn, Sn, Al, and Si) were found to be distributed uniformly in the sample. Similar observations have also been reported in literature [53, 54].

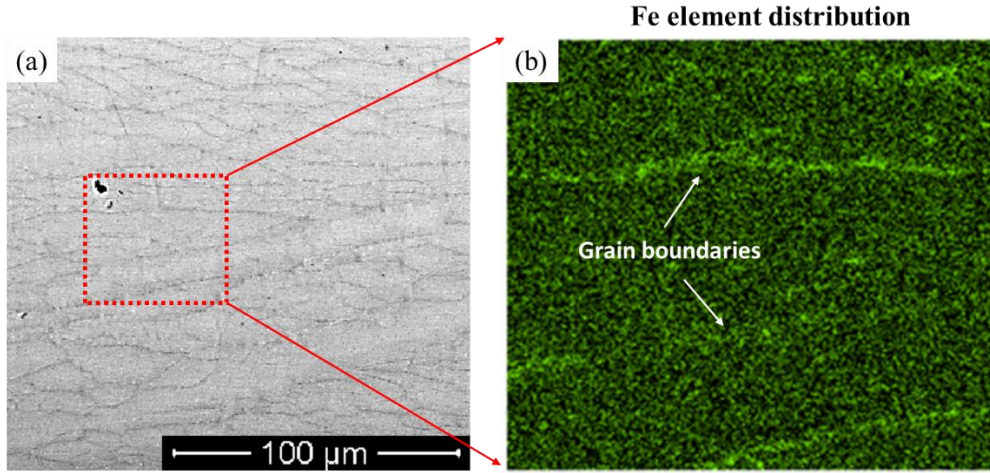


Figure 10. (a) BSE micrographs on sample 1. (b) EDS mapping of Fe element in the selected area.

Due to the complexity and anisotropic nature of the basketweave grain structure, there is no available model to predict thermal conductivity value for the basketweave grain structure. The most popular thermal conductivity model for polycrystalline materials is the Kapitza resistance model. In this model, the effective thermal conductivity for polycrystalline structures,  $K_{\text{eff}}$ , can be described as [45, 46],

$$K_{\text{eff}} = \frac{K_{\text{intra}}}{1 + R_k K_{\text{intra}}/d}. \quad (35)$$

In Eq. (35),  $K_{\text{intra}}$  is the thermal conductivity in the intragranular region or a single crystal structure,  $R_k$  is the Kapitza thermal resistance due to GBs, and  $d$  is the average grain size. The GB thermal resistance can be calculated by,

$$R_k = \frac{L_{\text{GB}}}{K_{\text{GB}}} = \frac{L_{\text{GB}}}{F_{\text{GB}} K_{\text{intra}}}. \quad (36)$$

In Eq. (36),  $F_{GB}$  is the suppression function defined as  $F_{GB} = \frac{K_{GB}}{K_{intra}}$ . Wu et al. [55] performed molecular dynamics (MD) simulations to study the thermal conductivity in  $\alpha$ -zirconium. Based on their study, the thermal conductivity at GB is only 12% of the bulk thermal conductivity. Therefore,  $F_{GB}$  can be approximated as 0.12.  $L_{GB}$  is the thickness of the GBs. Generally, a GB has a finite thickness of only a few angstroms. However, instead of considering a GB as a discrete thermal resistance locally, recent study shows GBs can exert their influence nonlocally, by increasing the heat carrier scattering rate in surrounding grains [11]. The influence range can be a few MFPs from the GB. Therefore,  $L_{GB}$  should be considered as the width of the GBs influence range. The heat carrier MFPs in metals and alloys are only a few nanometers. Thus,  $L_{GB}$  is estimated as 10nm for zircaloy. By taking  $K_{intra} = 12 \text{ Wm}^{-1}\text{K}^{-1}$ , the GB thermal resistance for zircaloy can be calculated as  $6.94 \times 10^{-9} \text{ m}^2\text{KW}^{-1}$ , which is comparable to the thermal resistances of the GBs ranging from  $10^{-10} \text{ m}^2\text{KW}^{-1}$  to  $10^{-9} \text{ m}^2\text{KW}^{-1}$  [56]. Figure 11 (a) depicts the comparison between experimental measurements and Kapitza model prediction on the correlation between thermal conductivity and grain size. The Kapitza resistance model predicts the effective thermal conductivity for a polycrystalline structure increases with the increase of average grain size, which is consistent with current Raman thermometry measurements that LIGs with larger mean true spacing have slightly higher thermal conductivity values. Moreover, according to the model prediction, the thermal conductivity suppression mainly happens when the grain size is smaller than  $2\mu\text{m}$ , while the mean true spacing in selected LIGs is in the range of  $2\mu\text{m}\sim 7\mu\text{m}$ . This also explains why the grain size induced thermal conductivity change is not very significant in current experimental measurements. It is also worth to notice that the Kapitza model assumes circular grains, thus deviations are expected when using it to predict thermal conductivity value for lamellar, platelets, or basketweave grain structures.

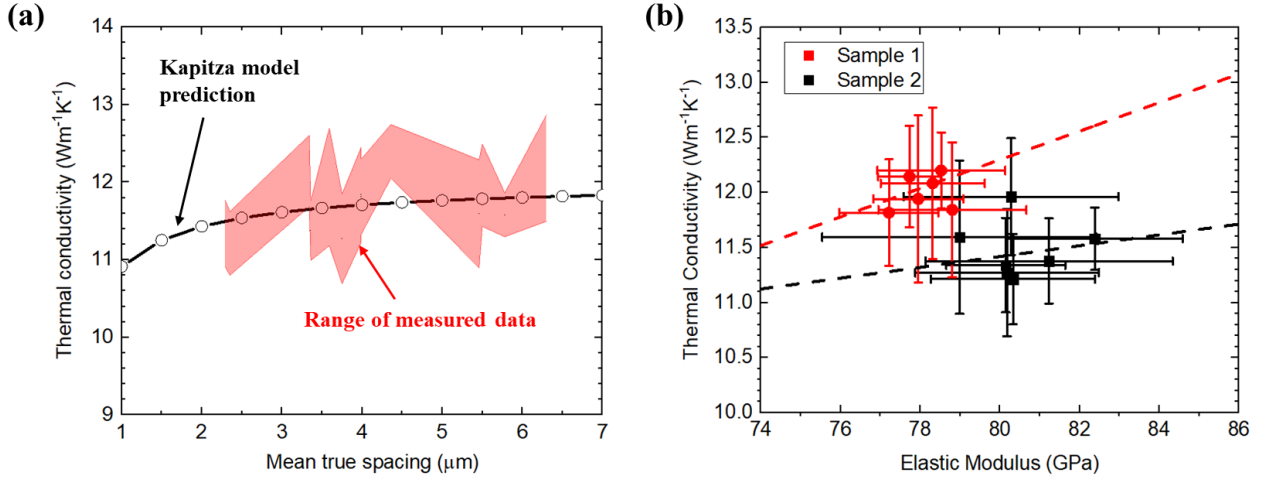


Figure 11. (a) Comparison between experimental measurements and Kapitza model prediction on the correlation of thermal conductivity and grain size, (b) thermal conductivity vs. average elastic modulus in selected LIGs.

Figure 11 (b) shows the correlation between the local thermal conductivity and the elastic modulus in selected LIGs based on the data summarized in Table 3 and Table 4. It is worth to notice that there is a clear difference in thermal conductivity and elastic modulus between sample 1 and 2. Sample 1 has a higher thermal conductivity and lower elastic modulus than sample 2. Such differences could be attributed to the variation in the fabricated microstructures. If the data from each sample is considered separately, the thermal conductivity shows a slight increasing trend with elastic modulus in each sample. In the Debye's model, the phonon group velocity equals to the velocity of sound, which can be estimated from the elastic modulus [57], as given in Eq. (37),

$$v_p = \sqrt{E/\rho}. \quad (37)$$

In Eq. (37),  $E$  is the elastic modulus and  $\rho$  is the density of solids. Thus, a higher elastic modulus leads to a higher phonon group velocity, which will further contribute to a larger phonon thermal conductivity. Generally, in metals and alloys, the electrons migration dominates the heat conduction [51]. While, based on the MD simulation results from Wu et al. [55], the phonon thermal conductivity contributes around 17.8% of the total thermal conductivity in  $\alpha$ -zirconium, which cannot be neglect in thermal conductivity analysis. Furthermore, they also studied the anisotropy of phonon thermal conductivity induced by grain orientations in  $\alpha$ -zirconium. Their

results are summarized in Table 5. As shown, MD simulations predict when the elastic modulus increases by 20GPa, the phonon thermal conductivity will increase by  $1.1 \text{ Wm}^{-1}\text{K}^{-1}$  in  $\alpha$ -zirconium. Such variation ratio between the elastic modulus and the phonon thermal conductivity is also close to our experimental observations. Therefore, the correlation between the local thermal conductivity and the elastic modulus may be attributed to the increase of the phonon thermal conductivity with the increasing elastic modulus.

Table 5. Crystallographic orientation induced anisotropy in phonon thermal conductivity [55].

<b>Orientation (<math>\alpha</math>-zirconium)</b>	<b>Elastic Modulus (GPa)</b>	<b>Phonon thermal conductivity (<math>\text{Wm}^{-1}\text{K}^{-1}</math>)</b>
[01 $\bar{1}$ 0]	104	2.8345
[2 $\bar{1}$ 10]	104	2.6661
[0001]	124	3.7769

## 1.5 Conclusion

For the first time, the Raman thermometry method has been extended to the thermal conductivity measurement of metallic samples by introducing a thin silicon coating. In this work, Raman thermometry method has been used to measure the thermal conductivity of notched polycrystalline zircaloy-4 samples. A heat transfer model was derived for this thin film system, relating the laser spot temperature on the film surface to the local thermal conductivity value of the substrate. To determine a potential relationship between microstructure, thermal conductivity, and mechanical properties, Raman thermometry and nanoindentation tests were performed, respectively, in various LIGs. The findings in this study are summarized as follows,

- (1) The thermal conductivity of zircaloy-4 measured in this study was found to range from 11-13  $\text{Wm}^{-1}\text{K}^{-1}$ , which is close to literature reported values ranging from 12~15  $\text{Wm}^{-1}\text{K}^{-1}$  [3-6, 42-44]. The small difference may be due to the thermal resistance at the interface between the silicon coating and the substrate, which is not considered in current heat transfer model.
- (2) LIGs with larger mean true spacing show slightly higher thermal conductivity values. This can be induced by the inhomogeneous composition/impurity distribution and the thermal resistance of GBs.
- (3) The correlation between thermal conductivity and grain size in selected LIGs follows the Kapitza resistance model prediction.

- (4) Based on measurements from selected LIGs, the thermal conductivity shows a slight increasing trend with the increase of the elastic modulus in each sample. Based on the classic kinetic model[51] and the Debye's model [57]. This may be attribute to the increase of the phonon thermal conductivity with the increase of the elastic modulus.

This research has demonstrated the determination of microstructure dependent thermal conductivity on zircaloy-4 samples by using the Raman thermometry method. This method can be easily extended to other morphologies, such as equiaxed grain structures. For future studies, a laser with lower wavelength and higher power can be used to improve the Raman signal quality, which may be helpful to reduce the measurement deviation. Other coating techniques and coating materials can also be used to enhance the temperature limitation and provide better Raman signals.

## 1.6 References

1. Konings, R., *Comprehensive nuclear materials*. 2011: Elsevier.
2. Anderson, W., C. Beck, A. Kephart, and J. Theilacker, *Zirconium Alloys*. Reactor Structural Materials: Engineering Properties as Affected by Nuclear Reactor Service, ASTM-STP, 1962. **314**: p. 62-93.
3. Fink, J. and L. Leibowitz, *Thermal conductivity of zirconium*. Journal Of Nuclear Materials, 1995. **226**(1-2): p. 44-50.
4. Murabayashi, M., S. Tanaka, and Y. Takahashi, *Thermal Conductivity and Heat Capacity of Zircaloy-2, - 4 and Unalloyed Zirconium*. Journal of Nuclear Science and Technology, 1975. **12**(10): p. 661-662.
5. Feith, A.D., *THERMAL CONDUCTIVITY AND ELECTRICAL RESISTIVITY OF ZIRCALOY-4*. 1966, General Electric Co., Cincinnati, Ohio. Missile and Space Div.
6. Scott, D., *Physical and Mechanical Properties of Zircaloy 2 and 4*. 1965, Westinghouse Electric Corp., Pittsburgh, Pa. Atomic Power Div.
7. Lucks, C. and H. Deem, *Progress Relating to Civilian Applications during June, 1958*. BMI-1273, 1958: p. 7-9.

8. Powers, A., *Application of the Ewing Equation for Calculating Thermal Conductivity from Electrical Conductivity*. 1953, Knolls Atomic Power Lab., Schenectady, NY.
9. Parrott, J.E. and A.D. Stuckes, *Thermal conductivity of solids*. Applied Physics Series. 1975, London: Pion. 10 , 157 p.
10. Tritt, T.M., *Thermal conductivity: theory, properties, and applications*. 2005: Springer Science & Business Media.
11. Sood, A., R. Cheaito, T. Bai, H. Kwon, Y. Wang, C. Li, L. Yates, T. Bougher, S. Graham, and M. Asheghi, *Direct visualization of thermal conductivity suppression due to enhanced phonon scattering near individual grain boundaries*. Nano letters, 2018. **18**(6): p. 3466-3472.
12. Perichon, S., V. Lysenko, B. Remaki, D. Barbier, and B. Champagnon, *Measurement of porous silicon thermal conductivity by micro-Raman scattering*. Journal of Applied Physics, 1999. **86**(8): p. 4700-4702.
13. Abel, M.R., S. Graham, J.R. Serrano, S.P. Kearney, and L.M. Phinney, *Raman thermometry of polysilicon microelectro-mechanical systems in the presence of an evolving stress*. Journal of Heat Transfer, 2007. **129**(3): p. 329-334.
14. Chen, S., Q. Li, Q. Zhang, Y. Qu, H. Ji, R.S. Ruoff, and W. Cai, *Thermal conductivity measurements of suspended graphene with and without wrinkles by micro-Raman mapping*. Nanotechnology, 2012. **23**(36): p. 365701.
15. Huang, S., X. Ruan, J. Zou, X. Fu, and H. Yang, *Raman Scattering Characterization of Transparent Thin Film for Thermal Conductivity Measurement*. Journal of Thermophysics and Heat Transfer, 2009. **23**(3): p. 616-621.
16. Huang, S., X. Ruan, J. Zou, X. Fu, and H. Yang, *Thermal conductivity measurement of submicrometer-scale silicon dioxide films by an extended micro-Raman method*. Microsystem Technologies, 2009. **15**(6): p. 837-842.
17. Lee, J.-U., D. Yoon, H. Kim, S.W. Lee, and H. Cheong, *Thermal conductivity of suspended pristine graphene measured by Raman spectroscopy*. Physical Review B, 2011. **83**(8): p. 081419.
18. Liu, X., X. Wu, and T. Ren. *A metrology of silicon film thermal conductivity using micro-Raman spectroscopy*. in *2010 IEEE International SOI Conference (SOI)*. 2010.

19. Puglia, D., L. Valentini, and J. Kenny, *Analysis of the cure reaction of carbon nanotubes/epoxy resin composites through thermal analysis and Raman spectroscopy*. Journal of applied polymer science, 2003. **88**(2): p. 452-458.
20. Soini, M., I. Zardo, E. Uccelli, S. Funk, G. Koblmüller, A.F. i Morral, and G. Abstreiter, *Thermal conductivity of GaAs nanowires studied by micro-Raman spectroscopy combined with laser heating*. Applied Physics Letters, 2010. **97**(26): p. 263107.
21. Yan, R., J.R. Simpson, S. Bertolazzi, J. Brivio, M. Watson, X. Wu, A. Kis, T. Luo, A.R. Hight Walker, and H.G. Xing, *Thermal conductivity of monolayer molybdenum disulfide obtained from temperature-dependent Raman spectroscopy*. ACS nano, 2014. **8**(1): p. 986-993.
22. Zhang, Y., M. Gan, and V. Tomar, *Raman thermometry based thermal conductivity measurement of bovine cortical bone as a function of compressive stress*. Journal of Nanotechnology in Engineering and Medicine, 2014. **5**(2): p. 021003.
23. Lo, H. and A. Compaan, *Raman measurements of temperature during cw laser heating of silicon*. Journal of Applied Physics, 1980. **51**(3): p. 1565-1568.
24. Pangilinan, G. and Y. Gupta, *Use of time-resolved Raman scattering to determine temperatures in shocked carbon tetrachloride*. Journal of Applied Physics, 1997. **81**(10): p. 6662-6669.
25. Reichling, M., T. Klotzbücher, and J. Hartmann, *Local variation of room-temperature thermal conductivity in high-quality polycrystalline diamond*. Applied Physics Letters, 1998. **73**(6): p. 756-758.
26. Cai, W., A.L. Moore, Y. Zhu, X. Li, S. Chen, L. Shi, and R.S. Ruoff, *Thermal transport in suspended and supported monolayer graphene grown by chemical vapor deposition*. Nano Letters, 2010. **10**(5): p. 1645-1651.
27. Chen, S., Q. Wu, C. Mishra, J. Kang, H. Zhang, K. Cho, W. Cai, A.A. Balandin, and R.S. Ruoff, *Thermal conductivity of isotopically modified graphene*. Nature Materials, 2012. **11**(3): p. 203-207.
28. Poruba, A., A. Fejfar, Z. Remeš, J. Špringer, M. Vaněček, J. Kočka, J. Meier, P. Torres, and A. Shah, *Optical absorption and light scattering in microcrystalline silicon thin films and solar cells*. Journal of Applied Physics, 2000. **88**(1): p. 148-160.
29. Beechem, T., S. Graham, S.P. Kearney, L.M. Phinney, and J.R. Serrano, *Invited article: simultaneous mapping of temperature and stress in microdevices using micro-Raman spectroscopy*. Review of Scientific Instruments, 2007. **78**(6): p. 061301.

30. Verma, D. and V. Tomar, *Structural-Nanomechanical Property Correlation of Shallow Water Shrimp (*Pandalus platyceros*) Exoskeleton at Elevated Temperature*. Journal of Bionic Engineering, 2014. **11**(3): p. 360-370.
31. Verma, D. and V. Tomar, *An investigation into environment dependent nanomechanical properties of shallow water shrimp (*Pandalus platyceros*) exoskeleton*. Materials Science and Engineering: C, 2014. **44**(0): p. 371-379.
32. Verma, D. and V. Tomar, *An investigation into mechanical strength of exoskeleton of hydrothermal vent shrimp (*Rimicaris exoculata*) and shallow water shrimp (*Pandalus platyceros*) at elevated temperatures*. Materials Science and Engineering: C, 2015. **49**(0): p. 243-250.
33. Oliver, W.C. and G.M. Pharr, *An improved technique for determining hardness and elastic modulus using load and displacement sensing indentation experiments*. Journal of materials research, 1992. **7**(6): p. 1564-1583.
34. Dryden, J., *The effect of a surface coating on the constriction resistance of a spot on an infinite half-plane*. Journal of Heat Transfer, 1983. **105**(2): p. 408-410.
35. Braun, J.L., C.H. Baker, A. Giri, M. Elahi, K. Artyushkova, T.E. Beechem, P.M. Norris, Z.C. Leseman, J.T. Gaskins, and P.E. Hopkins, *Size effects on the thermal conductivity of amorphous silicon thin films*. Physical Review B, 2016. **93**(14): p. 140201.
36. Gan, M. and V. Tomar, *An in situ platform for the investigation of Raman shift in micro-scale silicon structures as a function of mechanical stress and temperature increase*. Review of Scientific Instruments, 2014. **85**(1): p. 013902.
37. Holt, R., *The beta to alpha phase transformation in Zircaloy-4*. Journal of Nuclear Materials, 1970. **35**(3): p. 322-334.
38. Schneider, C.A., W.S. Rasband, and K.W. Eliceiri, *NIH Image to ImageJ: 25 years of image analysis*. Nature Methods, 2012. **9**(7): p. 671.
39. Underwood, E.E., *The mathematical foundations of quantitative stereology*, in *Stereology And Quantitative Metallography*. 1972, ASTM International.
40. Ni, J., Y. Zhao, L. Wang, Z. Zhang, and J. Xie, *Microstructure of Zircaloy-4 alloy during  $\beta$  phase quenching and determination of critical quenching diameter of its rods*. Nuclear Materials and Energy, 2018. **17**: p. 158-163.

41. Luscher, W.G. and K.J. Geelhood, *Material property correlations: comparisons between FRAPCON-3.4, FRAPTRAN 1.4, and MATPRO*. 2010, Pacific Northwest National Laboratory (PNNL), Richland, WA (US).
42. Agency, I.A.E., *Thermophysical properties database of materials for light water reactors and heavy water reactors*. 2006: International Atomic Energy Agency.
43. Hagrman, D., C. Allison, and G. Berna, *SCDAP/RELAP5/MOD 3.1 code manual: MATPRO, A library of materials properties for Light-Water-Reactor accident analysis. Volume 4*. 1995, Nuclear Regulatory Commission, Washington, DC (United States). .
44. International Atomic Energy, A., *Thermophysical properties database of materials for light water reactors and heavy water reactors : final report of a coordinated research project, 1999-2005*. Iaea-Tecdoc. 2006, Vienna: International Atomic Energy Agency. 397 p.
45. Nan, C.-W. and R. Birringer, *Determining the Kapitza resistance and the thermal conductivity of polycrystals: A simple model*. Physical Review B, 1998. **57**(14): p. 8264.
46. Yang, H.-S., G.-R. Bai, L. Thompson, and J. Eastman, *Interfacial thermal resistance in nanocrystalline yttria-stabilized zirconia*. Acta Materialia, 2002. **50**(9): p. 2309-2317.
47. Krstic, V., U. Erb, and G. Palumbo, *Effect of porosity on Young's modulus of nanocrystalline materials*. Scripta Metallurgica et Materialia, 1993. **29**(11): p. 1501-1504.
48. Shen, T.D., C.C. Koch, T.Y. Tsui, and G.M. Pharr, *On the elastic moduli of nanocrystalline Fe, Cu, Ni, and Cu-Ni alloys prepared by mechanical milling/alloying*. Journal of Materials Research, 2011. **10**(11): p. 2892-2896.
49. Fougere, G.E., L. Riester, M. Ferber, J.R. Weertman, and R.W. Siegel, *Young's modulus of nanocrystalline Fe measured by nanoindentation*. Materials Science and Engineering: A, 1995. **204**(1): p. 1-6.
50. Sanders, P., J. Eastman, and J. Weertman, *Elastic and tensile behavior of nanocrystalline copper and palladium*. Acta materialia, 1997. **45**(10): p. 4019-4025.
51. Bergman, T.L., F.P. Incropera, D.P. DeWitt, and A.S. Lavine, *Fundamentals of heat and mass transfer*. 2011: John Wiley & Sons.
52. Cahill, D.G., W.K. Ford, K.E. Goodson, G.D. Mahan, A. Majumdar, H.J. Maris, R. Merlin, and S.R. Phillpot, *Nanoscale thermal transport*. Journal of applied physics, 2003. **93**(2): p. 793-818.

53. Dong, Y., A.T. Motta, and E.A. Marquis, *Atom probe tomography study of alloying element distributions in Zr alloys and their oxides*. Journal of Nuclear Materials, 2013. **442**(1-3): p. 270-281.
54. Sundell, G., M. Thuvander, and H.-O. Andréén, *Enrichment of Fe and Ni at metal and oxide grain boundaries in corroded Zircaloy-2*. Corrosion Science, 2012. **65**: p. 10-12.
55. Wu, T.-Y., W.-S. Lai, and B.-Q. Fu, *Study of lattice thermal conductivity of alpha-zirconium by molecular dynamics simulation*. Chinese Physics B, 2013. **22**(7): p. 076601.
56. Crocombette, J.-P. and L. Gelebart, *Multiscale modeling of the thermal conductivity of polycrystalline silicon carbide*. Journal of Applied Physics, 2009. **106**(8): p. 083520.
57. Debye, P., *Zur Theorie der spezifischen Wärmen*. Annalen der Physik, 1912. **344**(14): p. 789-839.

## CHAPTER 2. CONSTITUTIVE MODELING OF ZIRCALOY HYDRIDE BASED ON STRAIN RATE DEPENDENT NANOINDENTATION AND NANO-SCALE IMPACT DATASET

Hao Wang<sup>a</sup>, Jonova Thomas<sup>b</sup>, Maria A. Okuniewski<sup>b</sup>, Vikas Tomar<sup>a,\*</sup>

<sup>a</sup> School of Aeronautics and Astronautics, Purdue University-IN, 47907, USA

<sup>b</sup> School of Materials Engineering, Purdue University-IN, 47907, USA

\*Corresponding author, Phone: (765)-494-3006 Fax: (765) 494-0307 Email: tomar@purdue.edu

Manuscript Under Preparation.

### Abstract

In this work, hydrogen was charged into zircaloy-4 samples to obtain  $\delta$ -hydride rim/blister structures. Nanoindentation and nano-scale impact experiments were performed on the hydride blister at elevated temperatures to obtain viscoplastic responses of  $\delta$ -hydride. By combining a finite element model with an iteration algorithm, the constitutive relation of  $\delta$ -hydride was revealed from test data. The power law model was used to represent the strain rate dependent plastic behavior of  $\delta$ -hydride. The Strength coefficient and the strain hardening exponent were found to decrease as temperature increased, which indicates softening behavior of hydride at high temperatures. The strain rate exponent remains as a constant with temperature increasing, which indicates the ductility of hydride does not change significantly at high temperatures. A finite element model was created to study the failure strength of  $\delta$ -hydride. The fracture strength of  $\delta$ -hydride was predicted at different temperatures. The ductile to brittle transition of the hydrided zircaloy structure has also been investigated.

**Keyword:**  $\delta$ -hydride, nanoindentation, nano-scale impact, viscoplastic model, fracture strength.

## 2.1 Introduction

As the primary nuclear fuel cladding material, zirconium alloys (zircaloy) are known for their outstanding thermomechanical properties and corrosion resistance at operating conditions [1]. However, during the operation of nuclear reactors, zircaloy cladding will chemically react with the high temperature coolant water, producing zirconium oxide and hydrogen. A small amount of hydrogen will diffuse into the cladding. Once the critical solubility limit is reached, second phase precipitates will form, which are known as zirconium hydrides [2]. Typically, there are four different phases of zirconium hydride:  $\zeta$ -phase ( $\text{ZrH}_{0.5}$ ),  $\gamma$ -phase ( $\text{ZrH}$ ),  $\delta$ -phase ( $\text{ZrH}_{1.5\sim 1.7}$ ), and  $\varepsilon$ -phase ( $\text{ZrH}_{1.75\sim 2}$ )[3]. In the reactor environment,  $\delta$ -phase hydrides are most often observed [3]. Moreover,  $\delta$ -hydrides are known to be extremely brittle at all temperatures and will significantly degrade the tensile strength, ductility, fracture toughness, and creep behavior of the cladding, and eventually leading to the failure of cladding [4, 5]. In the past five decades, extensive research has been conducted on the mechanical property changes of nuclear fuel cladding due to hydride precipitates [6-15]. It has been shown that there is an obvious transition from ductile failure to brittle failure in hydrided cladding, which depends on the temperature and hydride rim thickness [16-18]. Due to the limitation of experimental techniques, these tests were performed on large-scale “bulk” samples. Post fracture material characterization provides some insights into the hydride induced damage mechanism. However, mechanisms responsible for the ductile to brittle transition still cannot be revealed from macroscale tests, due to the complex microstructural features induced by the hydride formation at different length scales within the zircaloy matrix. In order to account for the microscopic features, constitutive models that incorporate local mechanical properties of embedded hydride precipitates at microscale are required [19].

Several advanced experimental techniques are available to obtain mechanical properties from hydride precipitates or bulk scale hydride blisters. Lin et al. [14] quantified the load partitioning phenomenon in  $\delta$ -hydride phase and  $\alpha$ -zirconium phase during uniaxial tensile loading by using high-energy synchrotron X-ray diffraction. Weekes et al. [20] studied the twinning and shear bands of  $\delta$ -hydride phase during micro-pillar compression tests. Chan et al. [21] performed micro-cantilever fracture tests to obtain the fracture toughness of  $\delta$ -hydride. Nanoindentation has been shown to be effective to obtain various local material properties at

elevated temperatures [22-32]. Nanoindentation has also been used to study the mechanical properties of  $\delta$ -hydride phase [9, 33-37]. Rico et al. [9] and Evans et al. [36] performed nanoindentation tests at room temperature and found Young's modulus and hardness of  $\delta$ -hydrides are significantly higher than the zircaloy matrix. Cinbiz et al. [37], Kese et al. [35], and Suman et al. [34] performed nanoindentation tests at elevated temperatures and found the elastic modulus and hardness of hydride both decrease as temperature increases. Overall, most nanoindentation experiments have been limited to measurements of nano-hardness and Young's modulus of hydrides. Recently, Rengel et al. [33] reported stress-strain curve of the hydrides based on their nanoindentation tests by using a spherical indenter. However, their experiments were performed only at room temperature, and the strain rate effect was not considered. Accounting for strain rate effects is essential for predicting time dependent deformation. Due to the complex nature of hydride assisted cracking, a more comprehensive strain rate dependent viscoplastic constitutive model needs to be established.

Studying the fracture strength of hydride is also an important topic. However, due to the small size of hydrides, it is very difficult to obtain the fracture strength of single-phase hydride. Most work in this area were performed to obtain the fracture properties on hydrided zircaloy structures, which shows an influence of hydride distribution on overall cladding ductility. There is very limited work on studying fracture strength of a single-phase hydride. Simpson et al. [38] performed fracture tests on compact tension specimens of single phase hydrides. The fracture toughness of hydrides was determined as decreasing with the increase of hydrogen/zirconium (H/Zr) ratio. The fracture toughness of  $\delta$ -hydride was reported varying from  $1 \text{ MPa}\sqrt{m}$  to  $3 \text{ MPa}\sqrt{m}$  as temperature goes up to  $300 \text{ }^\circ\text{C}$ . Chan et al. [21] performed micro-cantilever fracture tests at room temperature to obtain the fracture toughness of  $\delta$ -hydride. The fracture toughness was reported to be  $3.3 \text{ MPa}\sqrt{m}$ , which is slightly higher than the value obtained by Simpson et al. [38]. Based on the fracture toughness obtained from these tests,  $\delta$ -hydride is extremely brittle even at  $300 \text{ }^\circ\text{C}$ . This cannot answer why the failure process of hydrided zircaloy structure becomes ductile at high temperatures. Additionally, it also needs to be noticed that fracture toughness is different with fracture strength. Fracture toughness is a property which describes the ability of a material to resist pre-existing cracks, while fracture strength is the stress when a material fails or crack initiates. Shi et al. [39] studied the hydride fracture strength via acoustic

emission technique during uniaxial tensile tests. They reported the hydride fracture strength as a function of hydride length and temperature. However, the reported stress was the stress acting globally on the tensile specimen instead of the stress acting locally on the hydride. Furthermore, Leitch et al. [40] studied the elastic-plastic accommodation energy generated by the formation of plate-shaped hydride by using finite element models. Due to the lack of accurate stress-strain relation of hydrides, they used an elastic/perfectly plastic model for both the zircaloy matrix and hydride inclusion. Moreover, their assumption that the yield stress is the same for both phases does not hold at low temperatures [21].

In this research, nanoindentation and nano-scale impact techniques were used to obtain the constitutive relation of  $\delta$ -hydrides at elevated temperatures. High temperature experiments were performed inside a purge chamber, which was filled with nitrogen gas to minimize oxidation effects on the sample surface and on the indenter tip. Finite element simulations with an iterative algorithm were used to determine the plastic stress-strain curves of  $\delta$ -hydride. Then a power law viscoplastic model was fitted to the data in order to describe the elastoplastic response of  $\delta$ -hydride. Based on the global tensile stress reported by Shi et al. [39], the fracture strength of hydride was predicted by using finite element method (FEM) simulations. Furthermore, the ductile to brittle transition of the hydrided zircaloy structure has also been studied.

## 2.2 Experimental Setup

### 2.2.1 Sample Preparation

A recrystallization annealing (RXA) zircaloy-4 sheet from ATI Specialty Alloys and Components was used for this study. The chemical composition is shown in Table 6, which is very similar to the ASTM Standards B353-12 [41].

Table 6. Chemical composition of the as-received zircaloy 4 samples.

Elements	O	Sn	Fe	Cr	Al	Cu	Ni	Zn	Ca
Weight%	1.7	1.1	0.2	0.1	0.009	0.007	0.002	0.002	0.001

To minimize residual stresses, electrical discharge machining was used to cut specimens from the RXA zircaloy-4 sheet. Figure 12 (a) shows the dimension of the square sample. The

dimensions of the sample were determined to be  $1.2\text{cm} \times 1.0\text{cm}$ . Figure 12 (b) shows the microstructure of the as-received zircaloy-4 sample obtained via scanning electron microscopy (SEM).

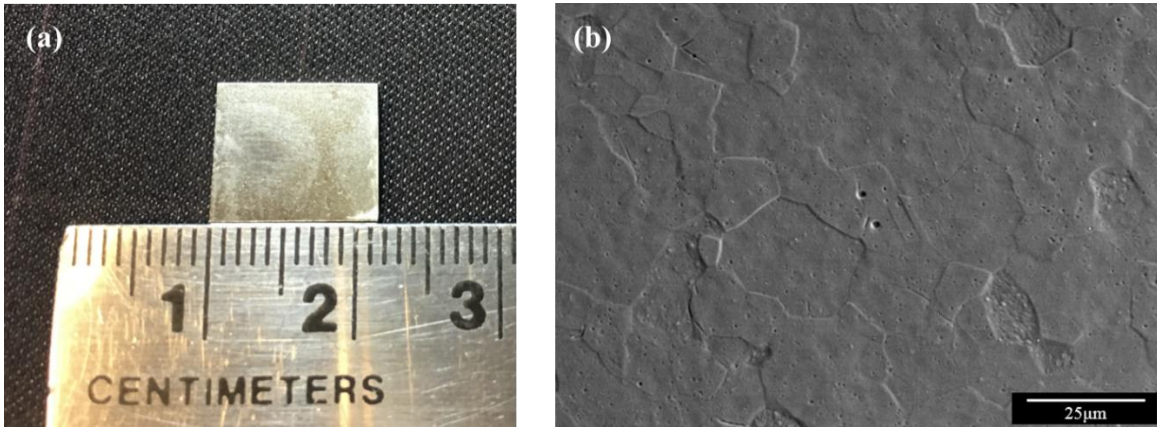


Figure 12. (a) Dimensions of the zircaloy-4 sample, (b) SEM back-scattered electrons image of the as-received zircaloy microstructure.

Two separate polishing steps were performed on the sample, (1) polishing the front surface of the sample to perform hydrogen charging, and (2) polishing the cross-section of the sample to perform nanoindentation and nano-scale impact experiments. Mechanical polishing with 600, 1000, 1200, and 2000 grade SiC papers, and  $1\ \mu\text{m}$  SiC suspension was performed for the front surface of the sample. A thin Ni film ( $\sim 300\ \text{nm}$ ) was then coated onto the polished surface of specimens by using the chemical vapor deposition technique, to enhance the hydrogen charging process and achieve desired near-surface hydride morphology [42]. Samples were heated up to  $400\ ^\circ\text{C}$  in a Sievert-type apparatus gas charging system to perform the hydrogen charging, and further details of the charging process can be found in literature [14, 43]. The samples remained in stress-free environment during the whole charging process, and the hydrogen concentration in these samples was calculated to be near 1200 weight part per million (wppm) post charging. To observe the hydride morphology, the sample was mounted in an epoxy holder with the cross-section exposed, as shown in Figure 13 (a). Then the cross-section was polished by using a mechanical polisher with 600, 1000, 1200, and 2000 grade SiC sheets, and  $1\ \mu\text{m}$  SiC suspension respectively. Finally, as the finishing step, a vibratory polisher with  $0.05\ \mu\text{m}$  colloidal silica suspension solution was used to obtain satisfactory sample surface condition. The sample

was etched with an acid solution of DI water, sulfuric acid, nitric acid, and hydrofluoric acid with a volume ratio of 10:10:10:1 for 5s to observe the hydride morphology by using optical microscopy. Figure 13 (b, d) depict optical microscope images of the cross-section of a hydrided zircaloy sample prepared using the above described method. Near the Ni coating surface, a hydride rich rim/blister structure was observed. The thickness of the hydride rim/blister structure was measured as 70  $\mu\text{m}$ , as shown in Figure 13 (b). Figure 13 (c) shows more details of the near-surface hydride rim/blister structure. Underneath the hydride rim/blister layer, smaller hydride precipitates evenly distribute in the zircaloy-4 matrix with random orientations, as shown in Figure 13 (d). Figure 13 (e, g) show the electron backscatter diffraction (EBSD) microstructure characterization of hydride rim/blister layer and zircaloy matrix respectively. Large equiaxed grains can be observed in zircaloy matrix, as shown in Figure 13 (g), while in the hydride rim/blister layer, all equiaxed zircaloy grains transfer to the lamellar zircaloy hydride grains, as shown in Figure 13 (e). Figure 13 (f, h) show the phase maps corresponding to Figure 13 (e, g) respectively. The  $\delta$ -hydride is colored as green and the  $\alpha$ -zircaloy matrix is colored as red. The volume fraction of  $\delta$ -hydride is about 95% in the hydride rim/blister layer.

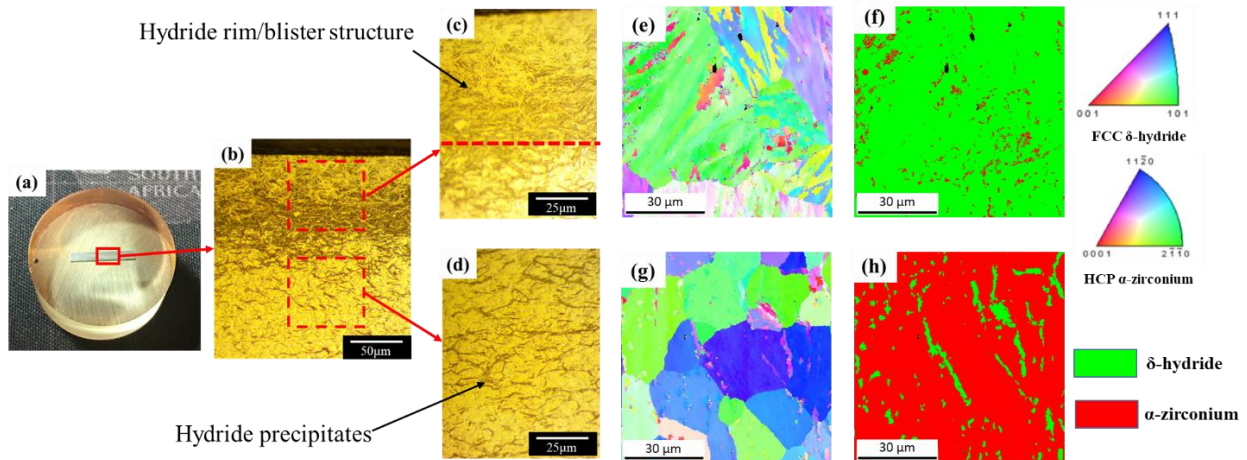


Figure 13. Optical microscope images of the hydrided zircaloy-4 sample, (a) the cross-section of a hydrided zircaloy-4 sample, (b) hydride morphology near the Ni coating surface, (c) near-surface high-density hydride rim/blister layer, (d) uniformly distributed hydrides in the zircaloy-4 matrix; (e)-(f) EBSD orientation map and phase fraction map of the hydride rim/blister layer, (g)-(h) EBSD orientation map and phase fraction map of the zircaloy matrix with individual hydride precipitates.

### 2.2.2 Nano-indentation Experiments

A multi-functional nanomechanical platform (Micro Materials Ltd., UK) [44-46] was used to perform all nanoindentation and nano-scale impact experiments at three different temperatures: room temperature (RT), 150°C, and 300°C. The platform sits inside a purge chamber, as shown in Figure 14 (a). During high temperature tests, the air inside the purge chamber was replaced by nitrogen (99.99% purity) to avoid any oxidation effects on sample surface and indenter tip. An oxygen meter (GREISINGER GOX-100) was used to monitor the oxygen concentration inside the purge chamber, and the oxygen concentration was maintained below 0.1% for all high temperature tests. When performing high temperature nanoindentation and nano-scale impact experiments, the indenter and the sample are required to be maintained at the same temperature to reduce the thermal drift effect. As a consequence, thermocouples were used for monitoring and controlling temperatures on the sample surface and the indenter tip. Other parts of the setup were maintained at room temperature via utilization of an insulated shield (see Figure 14 (b)).

Due to the small size of the hydride precipitates, a spherical diamond indenter with a radius of 0.7µm was used for experiments. The indenter tip geometry was calibrated under SEM, and a detailed description is provided in section 2.2.4. The room temperature machine compliance was calibrated on a fused silica sample as 0.27 nm/mN, and the high temperature machine compliance was calibrated on a sapphire sample as 0.40 nm/mN and 0.52 nm/mN for 150°C and 300°C, respectively. The indentation size effect of hydride was tested at RT to determine the peak load used for experiments. Figure 14 (c) shows the nano-hardness of hydrides as a function of the indentation depth. As shown, the indentation size effect of hydride ends at about 100nm. Therefore, a load of 3 mN with a loading/unloading rate of 0.15mN/s was used to carry out the experiments. Figure 14 (d) shows typical indentation curves on hydrides with a peak load of 3mN and a 5s dwelling period at different temperatures. The minimum indentation depth is about 200nm at RT, which avoids the indentation size effect of hydride. Twelve indents were performed on the hydride rim/blister layer at each temperature.

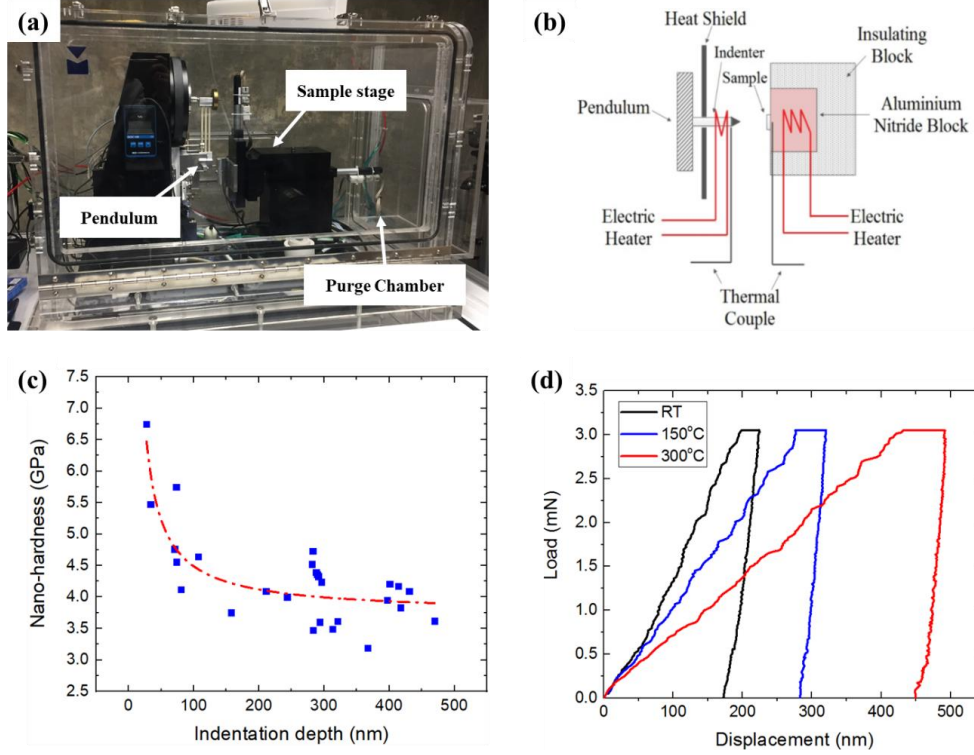


Figure 14. (a) The nanoindentation platform inside a purge chamber, (b) schematic of the high temperature nanoindentation setup, (c) analysis of the indentation size effect on hydride at RT, (d) representative indentation curves on hydride at different temperatures.

Following the Oliver and Pharr method, the Young's modulus and nano-hardness were obtained from the analyses of indentation load-depth curves [47].

$$E_r = \frac{\sqrt{\pi} S}{2 a_c}, \quad (38)$$

$$H = \frac{P_{\max}}{a_c}. \quad (39)$$

In Eq. (38),  $S=dP/dh$  denotes the slope of the initial unloading portion of a load-displacement curve (also known as the elastic stiffness),  $a_c$  is the projected area of the indentation at the contact depth, and  $P_{\max}$  is the maximum applied load.  $E_r$  is the reduced modulus, and can be expressed as shown in Eq. (40),

$$\frac{1}{E_r} = \frac{1 - \nu_s^2}{E_s} + \frac{1 - \nu_i^2}{E_i}. \quad (40)$$

In Eq. (40),  $E$  and  $\nu$  are the Young's modulus and the Poisson's ratio, respectively. The subscript  $i$  and  $s$  stand for the indenter and the specimen, respectively. Typically,  $E_i = 1141$  GPa and  $\nu_i = 0.07$  are used for a diamond indenter [48]. Moreover, Field et al. [49] reported the use of the stress-strain curve obtained from a nanoindentation for understanding material behavior at the microscale. The nanoindentation stress-strain in this study was obtained by using equations proposed by Kalidindi et al. [50].

$$\sigma_{\text{ind}} = \frac{P}{\pi a_c^2}, \quad \varepsilon_{\text{ind}} \approx \frac{h_e}{2.4a_c}. \quad (41)$$

In Eq. (41) and Eq. (42),  $P$  is the applied load, and  $h_e$  is the elastic depth, which was calculated from the load and the elastic stiffness [51].

$$h_e = \frac{3P}{2S}. \quad (42)$$

Eq. (43) shows the relationship between the contact depth and contact area.

$$h_c = h - \frac{1}{2}h_e; \quad a_c = \sqrt{2h_cR - h_c^2}, \quad (43)$$

In Eq. (43),  $h$  is the total depth,  $h_c$  is the contact depth, and  $R$  is the radius of the indenter.

The nanoindentation stress-strain data from experiments was considered as the quasi-static response of the material, the strain rate was determined to be around  $0.01 \text{ s}^{-1}$ . To obtain accurate stress-strain curves from nanoindentation, an important step is to perform the zero load/displacement correction, which helps to find the effective contact point and eliminates any artifacts created by unavoidable surface condition. At the initial elastic loading stage, a linear regression analysis was performed to obtain an effective zero load/displacement point [50]. The stiffness for a spherical indentation can be written as shown in Eq. (44).

$$S = \frac{3(P - P^*)}{2(h - h^*)}. \quad (44)$$

In Eq. (44),  $P$ ,  $h$ , and  $S$  are the measured load, displacement, and stiffness signal in the initial elastic loading stage, and  $P^*$  and  $h^*$  denote the load and displacement values at the actual contact point. Eq. (44) can be rearranged and plotted as  $P - \frac{2}{3}Sh$  versus  $S$ , (see Figure 15 (a)) with the linear portion of the slope and intercept representing  $-\frac{2}{3}h^*$  and  $P^*$ , respectively. As a

consequence, the actual load and displacement signal can be obtained via a linear regression analysis, and the corrected nanoindentation stress-strain curve are calculated, as shown in Figure 15 (b).

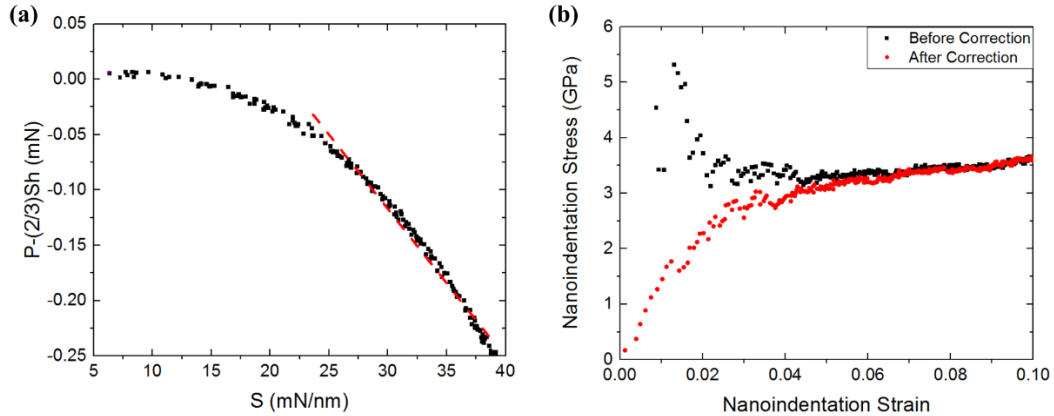


Figure 15. (a) The linear regression analysis for the zero load/displacement correction, (b) comparison of indentation stress-strain curve without and with the zero load/displacement correction.

### 2.2.3 Nano-scale Impact Experiment

In order to obtain the elastoplastic response of the  $\delta$ -hydride at higher strain rates, nano-scale impact tests were performed on the same platform. The schematic setup of pendulum is shown in Figure 16 (a). Before each impact, the pendulum was pulled at both ends, with the pre-defined force applied by the electromagnet at the top and the solenoid at the bottom. At impact, the solenoid releases the pendulum, and the indenter accelerates under the electromagnetic loading until it collides with the sample. The load that was applied to the pendulum was pre-defined as 0.2mN and remained constant during the whole impact. The displacement history of the indenter revealed information on strain rate, strain, and stress during the impact.

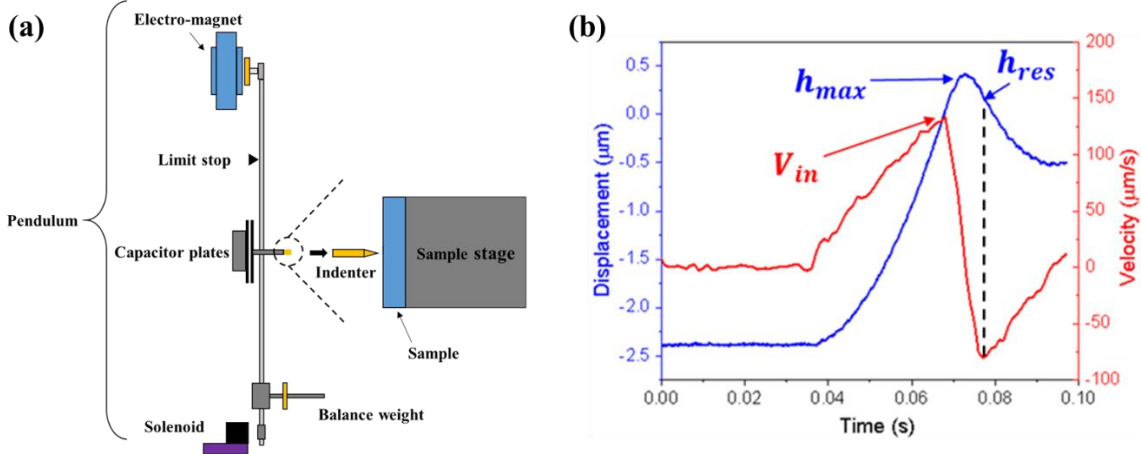


Figure 16. (a) The nanoindentation and nano-scale impact setup, (b) representative indenter displacement (blue curve) and velocity (red curve) history from a nano-scale impact test.

A typical displacement (blue curve) versus time history during the first penetration cycle is shown in Figure 16 (b). The sample surface is defined as zero displacement position, and positive displacement means penetration into sample. Since the indenter was pulled away from the sample surface before the impact, displacement starts from negative. The maximum penetration depth ( $h_{max}$ ) can be identified directly from the displacement history, and the indenter velocity (red curve) was obtained by taking first order time derivative to the displacement curve. The indenter is accelerated until it collides with the sample, and as a consequence, the maximum of the velocity trace is the initial contact velocity ( $V_{in}$ ). After contact, the indenter decelerates and bounces off the sample surface. Post deceleration and bouncing off sample surface, the indenter is re-accelerated via electromagnetic loading. Hence, the residual depth ( $h_{res}$ ) can be identified correlating to the minimum of the velocity trace. Although, the strain rate varies during the impact process, an average strain rate can be approximated by using Eq. (45) [52],

$$\dot{\epsilon} \approx \frac{V_{in}}{h_{max}}, \quad (45)$$

The strain rate in the nano-scale impact experiments determined by using Eq. (45) approached  $300 \text{ s}^{-1}$ . The strain calculation is same as Eq. (41), while the stress calculation was slightly different. In the stress calculation, the indenter load  $P$  is replaced by an effective force [53],

$$\sigma = F_{eq}/\pi a_c^2, \quad (46)$$

In Eq. (46),  $F_{eq}$  is the effective force during the impact penetration, and according to energy conservation principle,  $F_{eq}$  can be calculated with Eq. 10 [54],

$$\int_0^{h_{res}} F dh = F_{eq} \cdot \Delta h = \frac{m(V_{in}^2 - V_{out}^2)}{2}, \quad (47)$$

In Eq. (47),  $m$  is the effective mass of the pendulum, which was calibrated by dynamic hardness tests on a quartz sample at room temperature as 48g. Furthermore, the stress-strain data of both indentation and nano-scale impact were fitted by using the power law viscoplastic constitutive model, and ten impact experiments were performed on the hydride rim/blister layer at each temperature [55].

#### 2.2.4 Indenter Tip Geometry

Since both the nanoindentation stress and strain depend on the contact area of the indenter, characterizing indenter tip radius and curvature is very crucial to obtain the accurate stress-strain curves from nanoindentation tests. The topography of the indenter tip was obtained by a SEM microscope, as shown in Figure 17 (a).

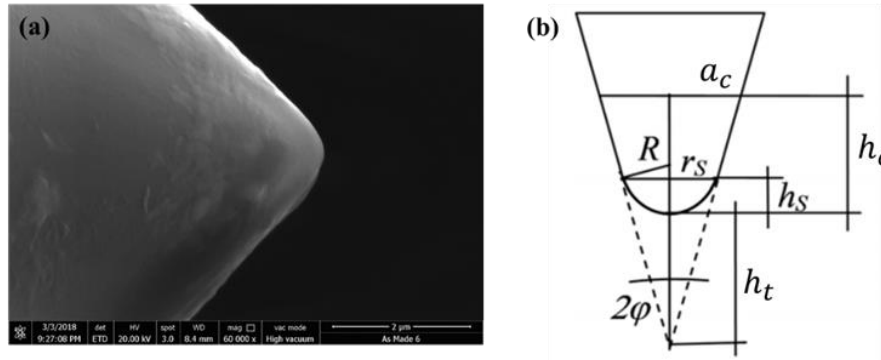


Figure 17. (a) SEM image of the indenter tip with a radius of 0.7  $\mu\text{m}$ . (b) Theoretical model of a conical indenter with a worn spherical tip [56].

The indenter used was a rigid conical-spherical indenter. Figure 17 (b) shows the spherical part of the indenter which is defined at the apex of the conical indenter. The radius  $R$  of the spherical part is calculated from the tip defect  $h_t$  and the cone angle  $\varphi$ , using the following Eq. (48) [56],

$$R = \frac{h_t}{\frac{1}{\sin \varphi} - 1}. \quad (48)$$

The transition depth  $h_s$  between the spherical and the conical parts of a conical-spherical indenter, was calculated using Eq. (49), and the contact area,  $a_c$ , was calculated using Eq. (50),

$$h_s = R(1 - \sin \varphi). \quad (49)$$

$$a_c = \sqrt{2Rh_c - h_c^2} \quad \text{for } h_c \leq h_s, \quad (50)$$

$$a_c = (h_t + h_c) \tan \varphi \quad \text{for } h_c \geq h_s.$$

The indenter parameters obtained via assessment of SEM image is detailed in Table 7. The indenter parameters were also used to analyze experimental data and create the indenter part in the FEM model.

Table 7. Indenter geometry parameters

$\varphi$	$h_t$ ( $\mu\text{m}$ )	$h_s$ ( $\mu\text{m}$ )	$R$ ( $\mu\text{m}$ )
46	0.271	0.194	0.688

## 2.3 Numerical Method

### 2.3.1 Finite Element Model For Nanoindentation

An axisymmetric finite element model was created in the ABAQUS v6.14 program to reproduce load-displacement curves of nanoindentation experiments, and isotropic material properties have been used in current model. The Poisson's ratio for the zircaloy-4 matrix and  $\delta$ -hydride used in the FEM model are 0.342 and 0.37 respectively [37, 57]. Since both the elastic modulus and the hardness of  $\delta$ -hydride are much smaller than diamond (less than 10%), the

indenter can be modeled as an analytical rigid object [58]. The model geometry is shown in Figure 18 (a), and the geometry of the indenter was determined based on the SEM image assessment (see Figure 17). The size of the matrix is  $10\mu\text{m} \times 10\mu\text{m}$ , and a partition area of  $2\mu\text{m} \times 2\mu\text{m}$  was created to refine the mesh near the indentation site. The depth of the indentation was less than  $0.5\mu\text{m}$ , and as a consequence, the bottom side of the matrix is not affected by the indentation, which was fixed in both x and y direction. The left side along the symmetric axis, is fixed in x direction and allowed to move freely in y direction. Furthermore, a displacement-controlled boundary condition was used in nanoindentation simulations to calculate the reaction force which is then compared to the experimental load-displacement curves. The friction between the indenter and the material was neglected as a consequence of indenter penetration depth being small [33]. The two dimensional (2-D) non-linear geometry and the finite sliding contact hypothesis was also used for all the simulations. A reduced integration scheme was then applied in the region far from the contact point to reduce computational costs. The minimum size of the element at the contact region was set to 10 nm. Figure 18 (b, c) shows a typical stress distribution and plastic strain field around the indenter during an indentation test.

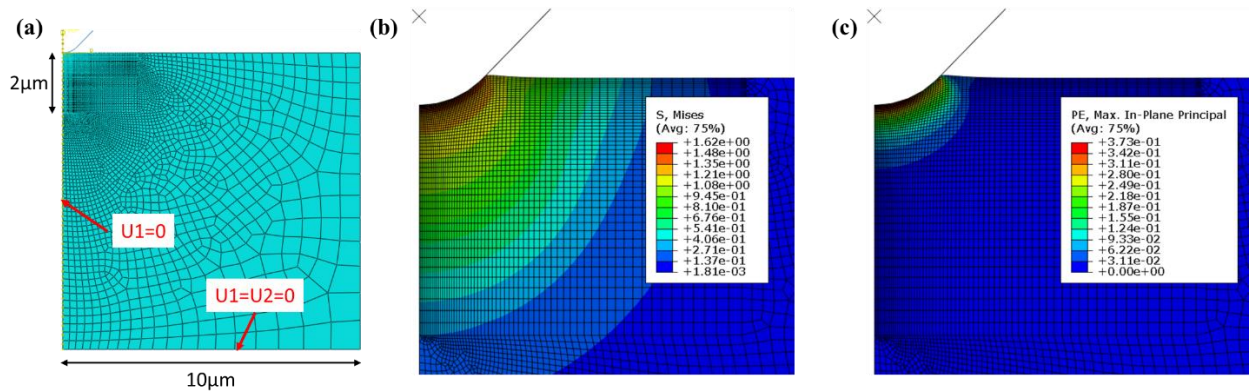


Figure 18. (a) Geometry and boundary conditions for the nanoindentation FEM model. (b) Stress (GPa) distribution during a nanoindentation test. (c) Plastic strain field during a nanoindentation test.

### 2.3.2 Iteration Algorithm

The stress state in the material under a nanoindenter is very complicated. Hence, the stress-strain relation obtained from nanoindentation tests are considered as effective ones. It is known that the stress-strain relation obtained from nanoindentation experiments generally overestimate material strength in comparison to the relations obtained from macroscale tests. In this work, an iteration algorithm proposed by Rengel, et al. [33] was used to correct the effective stress-strain relation for the material. Experimental load-displacement curves produced from nanoindentation tests were reproduced by using the FEM simulations and the iterative algorithm in tandem. As a consequence, the stress-strain relation used in the FEM simulations is considered as the true effective stress-strain relation for the material. The original iteration algorithm performs the correction in a pointwise fashion, and the correction at a certain strain is based on the difference between load-displacement curves at the corresponding displacement point. Hence, the correction amount at different strain is different, and over-correction tend to occur when a large difference is present between the experimental and FEM predicted load-displacement curves. To mitigate this issue, modifications were made on this iteration algorithm by replacing the pointwise correction with an averaged correction ratio.

By using the stress-strain curve obtained from nanoindentation tests, the first iteration load-displacement ( $P_1 - h_1$ ) curve was obtained from the FEM simulation. Comparing with the experimental data ( $P_{\text{exp}} - h_{\text{exp}}$ ), the new stress-strain data can be determined in an iterative fashion using Eq. (51).

$$\sigma_{i+1}(\varepsilon) = \delta \cdot \sigma_i(\varepsilon) \cdot \frac{1}{n} \sum_{j=1}^n \frac{P_{\text{exp}}(d_j)}{P_i(d_j)} + (1 - \delta) \cdot \sigma_i(\varepsilon). \quad (51)$$

In Eq. (51),  $d$  is the displacement,  $\delta$  is a parameter that changes linearly from 0.4 to 1 in 10 iterations, and is dependent on the current iteration number,  $\varepsilon$  is the effective plastic strain that corresponds to the value of displacement, and  $n$  is the total number of data points on the experimental load-displacement curve. Additionally, the relation between  $\varepsilon$  and  $d$  can be established by using Eq. (52) and Eq. (53),

$$t = \frac{d - d_{\min}}{d_{\max} - d_{\min}}, \quad (52)$$

$$\varepsilon = \varepsilon_{\max} \cdot t^{\alpha} . \quad (53)$$

In Eq. (52) and Eq. (53),  $t$  is the interpolation parameter varying in the range (0,1),  $d_{\max}$  is the maximum displacement value,  $d_{\min}$  is the displacement value where the stress-strain curve separates approximately from initial experimental one, and  $\alpha$  is an exponent equal to 1 in this study. More information about parameters in this iteration algorithm is detailed by Rengel et al. [33] elsewhere. Since isotropic material properties has been assumed in FEM simulations, the converted stress-strain relation should be considered as an isotropic effective stress-strain relation. The converted effective stress-strain curve also provides other important information (such as yield stress, hardening exponent, etc.) about the material.

### 2.3.3 Viscoplastic Power Law Model

Depending on the type of stress, the stress-strain behavior of hydride can be identified by two different correlations [59]. Before yielding, Eq. (54) representing Hooke's law was used to describe the elastic deformation; whereas,

$$\sigma = \varepsilon \cdot E. \quad (54)$$

After yielding, a power law model proposed by Fields et al. [55] was used to describe the plastic deformation (see Eq. (55)). Since this model accounts for the strain-hardening and the strain rate sensitivity, it has been widely used to describe the viscoplastic behavior in different materials,

$$\sigma = K\varepsilon^n \left( \frac{\dot{\varepsilon}}{\dot{\varepsilon}_0} \right)^m = K\varepsilon^n (\dot{\varepsilon}^*)^m. \quad (55)$$

In Eq. (18),  $K$  is the strength coefficient,  $n$  is the strain hardening exponent,  $m$  is the strain rate exponent, and  $\dot{\varepsilon}_0$  is the reference strain rate, which is considered as  $1 \text{ s}^{-1}$  in this study. Following the method proposed by Tsai et al. [60], these material parameters can be determined by assuming an effective viscoplastic stress-strain curve in the form, as shown in Eq. (56),

$$\sigma = A \cdot \varepsilon^n. \quad (56)$$

In Eq. (56),  $A$  is presented as a function of the effective plastic strain rate  $\dot{\varepsilon}^*$ ,

$$A = K(\dot{\epsilon}^*)^m. \quad (57)$$

By linearly fitting the obtained nanoindentation and nano-scale impact stress-strain data on the log–log scale by using Eq. (56), the values of A and n can be determined as the intercept and the slope respectively. Additionally, via Eq. (57), the parameters K and m can be determined in a similar fashion. Once the parameters K, n, and m are determined, material behavior at different strain rates can be predicted. The yield stress is given as the non-zero intersection of Eq. (54) and Eq. (55), which can be written as Eq. (58),

$$\sigma_y = \left[ \frac{K}{E^n} (\dot{\epsilon}^*)^m \right]^{\frac{1}{1-n}}. \quad (58)$$

### 2.3.4 Finite Element Model For Hydride Cracking

The Fracture strength of hydride estimated via the FEM models in this study was based on the global tensile fracture stress reported by Shi et al. [39]. A 2-D axisymmetric FEM model was created in the ABAQUS v6.14 program to calculate the stress in a single hydride precipitate at crack initiation. Figure 19 (a) shows the dimension of the simulation domain. The width of simulation domain was fixed as 20 $\mu\text{m}$ , and the height was set as 1.5L, where L is the length of the hydride precipitate. The hydride precipitate was modeled in an oblate spheroid shape with a fixed thickness of 3  $\mu\text{m}$ . The length of the hydride varies from 20  $\mu\text{m}$  to 160  $\mu\text{m}$ , and a uniaxial tensile loading was applied on the top edge of the domain during deformation. The left edge was modeled as the central axis and fixed in the x direction, the bottom edge was fixed in the y direction. Triangular element (CAX3) with a size of 0.2 $\mu\text{m}$  was used in the hydride phase. Quadrilateral element (CAX4) was used in the zircaloy-4 matrix phase, the maximum element size was 1 $\mu\text{m}$  at edges of the domain. Both the hydride and the zircaloy-4 matrix were considered as isotropic materials, and the viscoplastic constitutive relation obtained in current work was input as material properties of the hydride phase. Additionally, the model proposed by Geelhood et al. [59] was used as the elastoplastic material properties of the zircaloy-4 matrix. The Poisson's ratio for the zircaloy-4 matrix and  $\delta$ -hydride used in the FEM model are 0.342 and 0.37 respectively [37, 57].

Formation of  $\delta$ -hydride precipitates in a zircaloy matrix leads to generation of misfit strains (a consequence of volume expansion), and for a  $\delta$ -hydride plate lying on near-basal planes, the

volume expansion was estimated to be 17.2% [61]. In current FEM model, the misfit strain distribution was implemented isotopically, and the misfit strain was distributed equally in different directions as 0.054 [40]. The misfit strain was modeled with a pre-defined field prior to tensile loading, and Figure 19 (b, c) shows the stress field and equivalent plastic strain field induced by isotropic misfit strain distribution. The FEM model was used primarily to assess the variation in fracture strength of the  $\delta$ -hydride with respect to (1) hydride length, and (2) different temperatures (RT, 150°C, and 300°C).

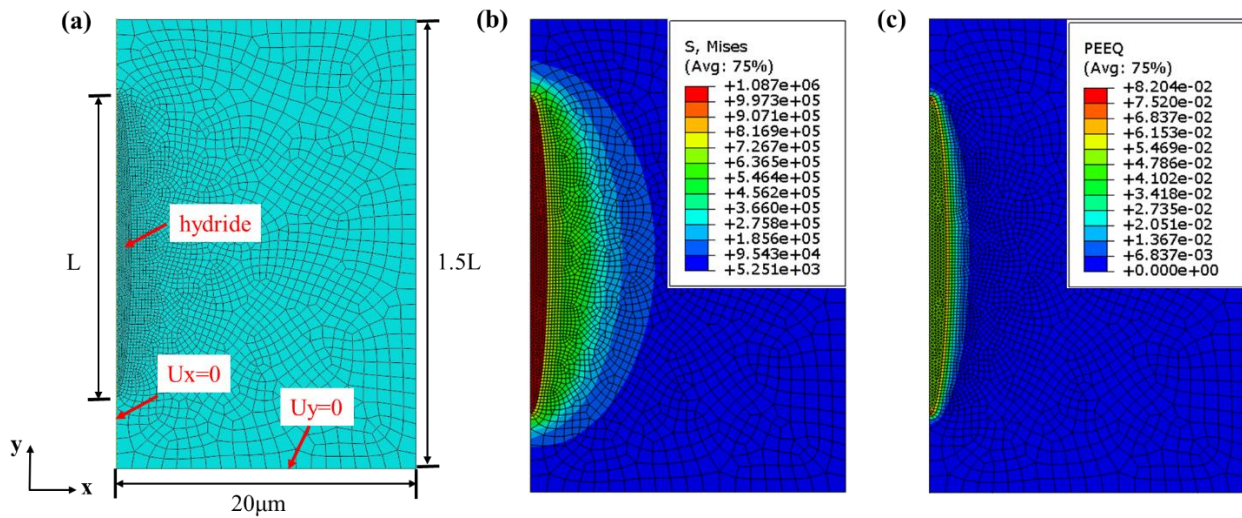


Figure 19. (a) Geometry and boundary conditions for the hydride cracking FEM model. (b) Stress field (kPa) induced by isotropic misfit strain distribution, (c) equivalent plastic strain field induced by isotropic misfit strain distribution.

## 2.4 Results and Analyses

### 2.4.1 Elastic Modulus And Nanoindentation Hardness

The elastic modulus was calculated from measured reduced modulus by using Eq. (40). As shown in Figure 20 (a), the elastic modulus of  $\delta$ -hydride was measured as  $91.65\pm 4.35$  GPa,  $87.11\pm 4.54$  GPa, and  $78.72\pm 4.88$  GPa (mean  $\pm$  standard deviation) at RT, 150°C, and 300 °C, respectively. The elastic modulus of  $\delta$ -hydride decreases at elevated temperatures, and this trend corroborates with the findings from other researchers [34, 35, 37]. Additionally, the elastic modulus is observed to drop by 14% as temperature increases to 300 °C. Figure 20 (b) shows the nanoindentation hardness of  $\delta$ -hydride, which was measured as  $4.02\pm 0.21$  GPa,  $2.71\pm 0.19$  GPa,

and  $1.60 \pm 0.13$  GPa at RT, 150 °C, and 300 °C, respectively. The nanoindentation hardness of  $\delta$ -hydride decreases as a function of increasing temperature, and is corroborated with the findings from other researchers [34, 37]. Table 8 details the reported mechanical properties of  $\delta$ -hydride from different nanoindentation tests. The large variations observed in both elastic modulus and nano-hardness in Table 8, may be attributed to influences from different sample preparation methods and indenters used. More importantly, some works used very small nanoindentation loads without considering the indentation size effect [36].

Eq. (59) details the empirical relationship that can be used to calculate the yield stress of a material from the nanoindentation hardness [62],

$$H = c \cdot \sigma_y. \quad (59)$$

In Eq. (22),  $c$  is a constrain factor, and a value of 5.04 reported by Kese et al. [35] was used in this study to relate the nanoindentation hardness to the yield stress of  $\delta$ -hydride. The right axis of Figure 20 (b) shows the yield stress of  $\delta$ -hydride estimated by using Eq. (59). The estimated yield stress is very close to values reported from other experimental methods, such as compression tests on bulk hydrides [13], micro-cantilever fracture tests [21], and micro-pillar compression tests [20].

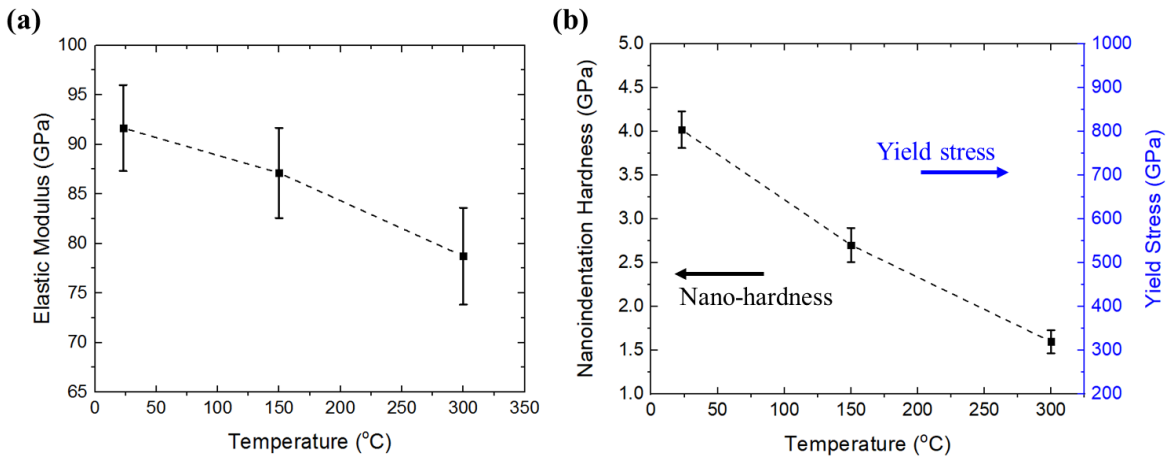


Figure 20. Material properties of  $\delta$ -hydride under different temperatures: (a) elastic modulus, (b) nanoindentation hardness (left axis) and yield stress (right axis).

Table 8. A comparison of elastic modulus and nano-hardness of  $\delta$ -hydride reported in literatures.

	Young's modulus (GPa)			Nano-hardness (GPa)			Test Method
	25°C	150°C	300°C	25°C	150°C	300°C	
Siddharth et al. [34]	133.18	115	100	4.6	3	2.1	Nanoindentation
Cinbiz et al. [37]	97.46	96.4	95	4.1	3	2.8	Nanoindentation
Kese et al. [35]	115	109	106	5.3	5.2	5.3	Nanoindentation
Rico et al. [9]	92	-	-	2	-	-	Nanoindentation
Evans et al. [36]	155	-	-	4.6	-	-	Nanoindentation
Rengel et al. [33]	99	-	-	4.5	-	-	Nanoindentation
Menibus et al. [63]	80-95	-	-	5.8	-	-	Nanoindentation
Pan et al. [64]	90-100	87-95	80-90	-	-	-	Internal Friction
Puls et al. [13]	80-95	-	-	-	-	-	Compression
Chan et al. [21]	80-85	-	-	-	-	-	Micro Cantilever

#### 2.4.2 Correction For Plastic Stress-Strain Curve

As described in section 2.3.2, the stress-strain relation can be obtained from the loading part of the nanoindentation load-displacement curve. For example, Figure 21 shows the analysis of the 150 °C nanoindentation data. Figure 21 (a) depicts the loading part of load-displacement curves with both mean (black curve) and variations (red shadow), and Figure 21 (b) shows the corresponding nanoindentation stress-strain curve calculated from the load-displacement curve in Figure 21 (a).

By using the FEM model and iteration algorithm described in sections 2.3.1 and 2.3.2, corrections can be performed to reveal the true stress-strain relation of the hydride phase. By inputting the stress-strain relation obtained from nanoindentation tests to the FEM model, a predicted load-displacement curve was obtained. Additionally, based on the difference between the predicted curve and the actual load-displacement curve from experiments, a new stress-strain curve was calculated using Eq. (14). A Matlab script was programmed to run FEM simulations and perform iterations (detailed in sections 2.3.1 and 2.3.2) automatically. Figure 21 (c, d) depicts the evolution of the load-displacement curves and plastic stress-strain curves at different iterations. Red curves are the load-displacement curve and the plastic stress-strain curve obtained from experiments; while, gray curves are outputs from FEM simulations at each iteration step. The black arrows in Figure 21 (c, d) shows the changing directions of these curves during iterations. After performing 8 iterations, the FEM predicted load-displacement curve perfectly matches with the experimental one. The yield stress of  $\delta$ -hydride after correction is nearly 500 MPa at 150°C,

and is very close to the value estimated from nanoindentation hardness experiments. Similar analyses were performed on the test data at RT and 300 °C.

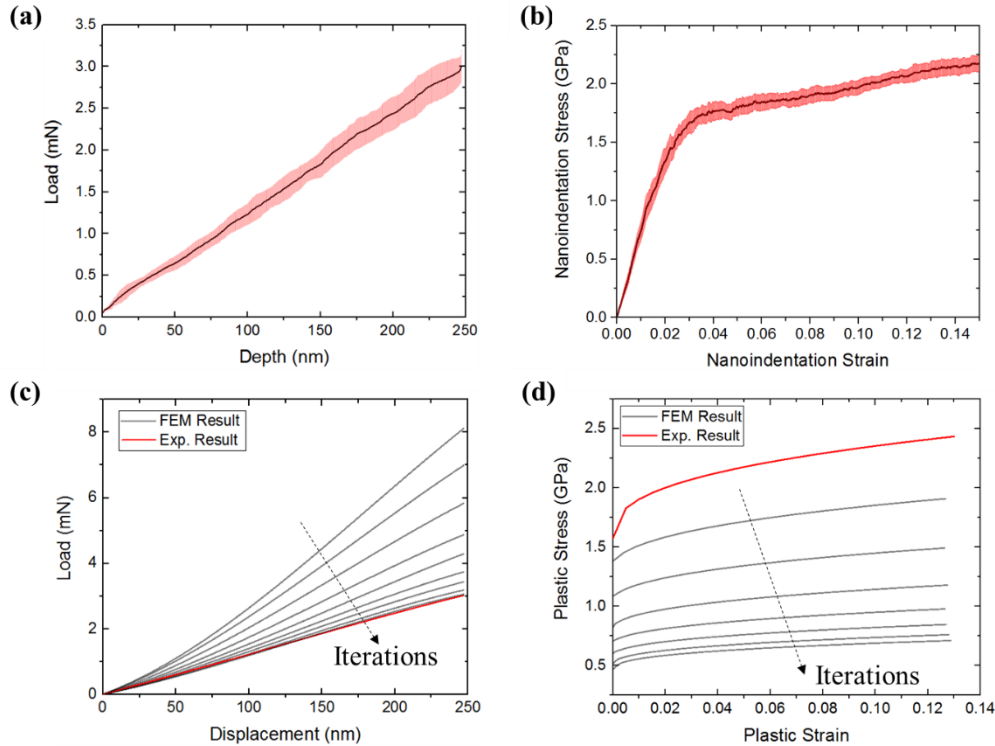


Figure 21. 150°C experimental data and analysis, (a) nanoindentation load-displacement curve with mean (black curve) and variations (red shadow) of  $\delta$ -hydride, (b) nanoindentation stress-strain curve of  $\delta$ -hydride, (c) evolution of load-displacement curves during iterations, (d) evolution of plastic stress-strain curves during iterations.

### 2.4.3 Power Law Model Fitting

The stress-strain relation from nanoindentation and nano-scale impact tests were fitted by using the power law viscoplastic model detailed in section 0. Figure 22 shows the linear fitting of RT experimental data which was used to determine the model parameters. A linear regression analysis was performed on the plastic portion of the nanoindentation stress-strain curve (see Figure 22 (a)). Furthermore, the slope and y-axis intercept from the line regression analysis reveals the strain hardening exponent  $n$  and  $\log(A)$  at  $\dot{\epsilon} = 0.01s^{-1}$ , respectively. Figure 22 (b) depicts the linear regression analysis for nano-scale impacts, and the intercept with y-axis is  $\log(A)$  at  $\dot{\epsilon} = 300s^{-1}$ . Additionally, repeating the linear regression analysis on  $\log(A)$  vs.  $\log(\dot{\epsilon})$

(see Figure 22 (c)), assists in determining the strain rate exponent  $m$  (slope) and  $\log(K)$  (y-axis intercept), respectively.

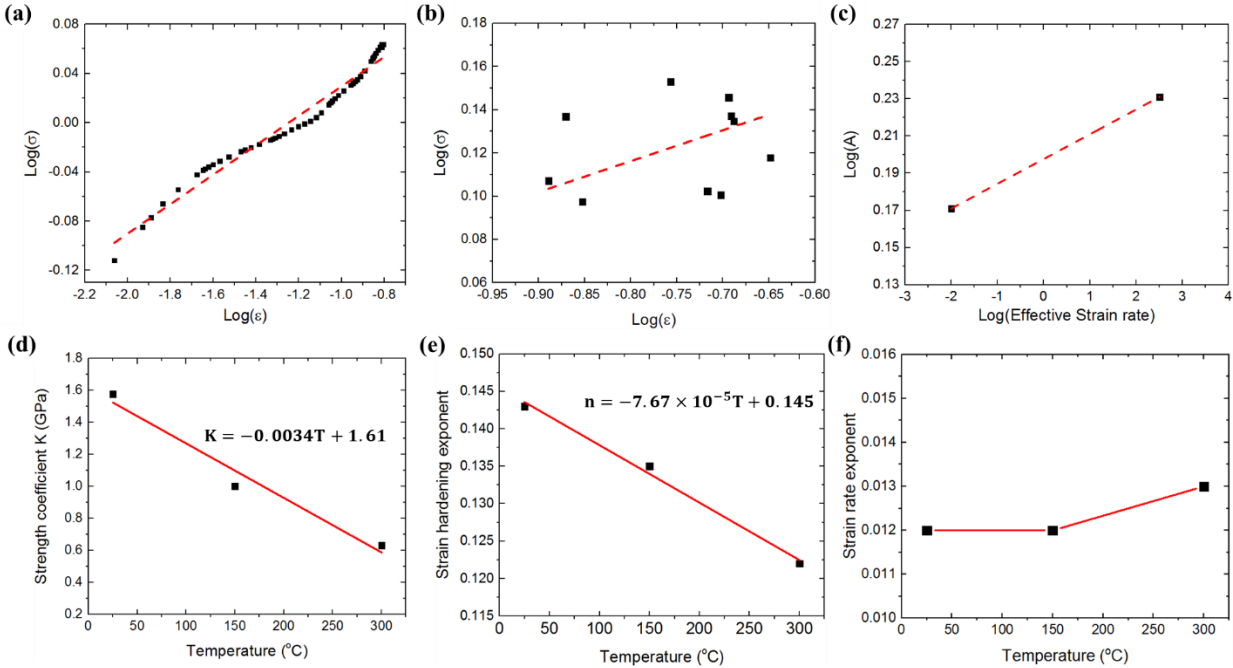


Figure 22. Linear fitting process to determine parameters for the power law model: (a) nanoindentation data, (b) nano-scale impact data, (c)  $\text{Log}(A)$  vs.  $\text{Log}(\dot{\epsilon})$ . (d) The strength coefficient  $K$  as a function of temperature, (e) the strain hardening exponent as a function of temperature, (f) the strain rate exponent  $m$  as a function of temperature.

Similar assessments were performed on the test data at  $150^{\circ}\text{C}$  and  $300^{\circ}\text{C}$ , and the power law viscoplastic model parameters ( $k$ ,  $n$ , and  $m$ ) determined in this study is summarized in Table 9. Figure 22 (d - f) show the changes in trend of  $K$ ,  $n$ , and  $m$  at different temperatures. Figure 23 (a) shows the comparison between fitted power law viscoplastic model (dashed lines) and experimental results (dotted symbols). The graph reveals that the yield stress at elevated temperatures match with values estimated from nanoindentation hardness tests. Figure 23 (b) shows the comparison between experimental (solid lines) and FEM simulated (dash lines) load-displacement curves at different temperatures. Since creep properties were not measured in current study, the dwelling time in FEM simulation is set as zero. Unloading initiates spontaneously when the maximum load was reached. As shown in Figure 23 (b), the FEM simulation results agree well with experimental results.

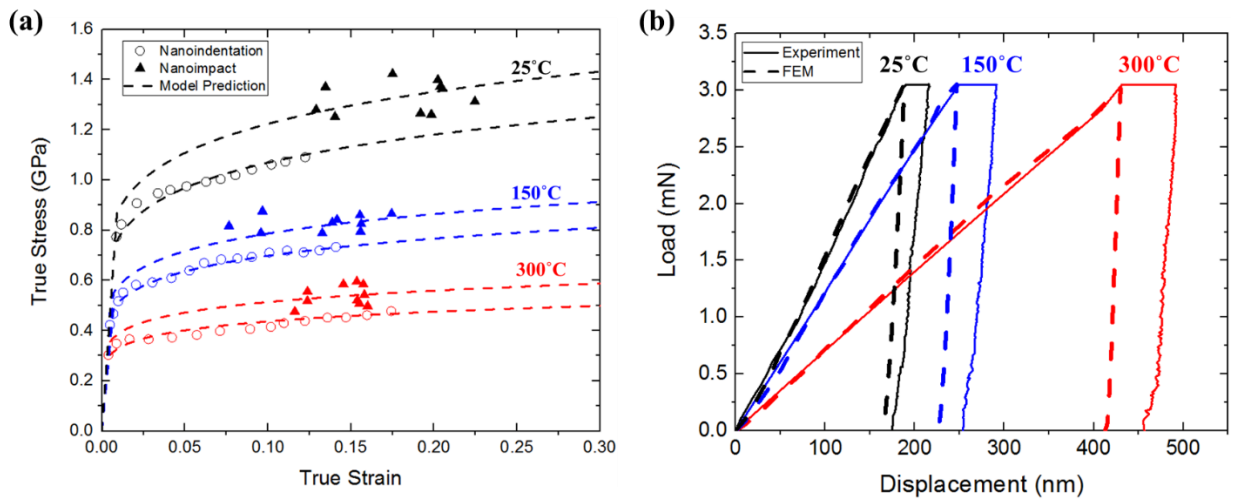


Figure 23. (a) Stress-strain response of  $\delta$ -hydride at RT (black), 150°C (blue), and 300°C (red), (b) experimental and simulated load-displacement curves at different temperatures.

Table 9. Viscoplastic material parameters for  $\delta$ -hydride

	K (GPa)	$n$	$m$
RT	1.577	0.143	0.012
150°C	1.002	0.135	0.012
300°C	0.631	0.122	0.013

#### 2.4.4 FEM Simulation For Hydride Cracking

FEM simulations calculated hydride fracture strength in the current study was compared to the global tensile stresses reported by Shi et al. [39]. Figure 24 (a) shows the relation between hydride fracture strength vs. hydride length at RT, and tensile stresses vs. hydride length reported by Shi et al. [39]. Shi et al. [39] reported the following: (1) when the hydride length is smaller than 80 $\mu$ m, the fracture strength of hydride decreases linearly, and (2) when the hydride length is larger than 80 $\mu$ m, the fracture strength remains as a constant. Interestingly, the FEM simulations on hydride cracking in the current study corroborates the findings reported by Shi et al. [39]. The model used in this study clearly shows the following: (1) when the hydride length is larger than 80 $\mu$ m, the hydride fracture is constant (~1030MPa). (2) The fracture strength increases as

hydride length decreasing. (3) The maximum fracture strength is nearly 1070MPa. Furthermore, it should be noted that the variation of the fracture strength with respect to hydride length is relatively small, (~40MPa), and the fracture strength of hydride at room temperature was determined to be ~1030MPa. In conclusion, the fracture strength of the hydride (at room temperature) determined from this study appears to be in a close proximity to fracture strength estimated from micro-scale fracture tests [20, 21].

Additionally, the relation between hydride fracture strength and temperature was also determined. The hydride length selected for the FEM simulations were 120  $\mu\text{m}$ . From Figure 24 (b), it is evident that the fracture strength of hydride decreases with temperature increasing. The hydride fracture strength calculation in the current study is only valid up to 200°C as a consequence of change in the failure mechanisms of the hydrided zircaloy. At temperatures above 200°C, the failure mechanism of hydrided zircaloy structure changes from brittle hydride cracking to ductile failure of zircaloy-4 matrix [15, 65]. A linear regression was performed to fit the relation between the hydride fracture strength and temperature, which predicts the fracture strength is about 400MPa at 300°C. The tensile strain of the simulation domain at hydride fracture is shown in Figure 24 (c), reveals the brittle-ductile transition at a temperature range spanning between 100 °C and 150°C. Furthermore, the simulation results on brittle-ductile transition in the current study is also corroborated via experimental observations from other researches [66, 67].

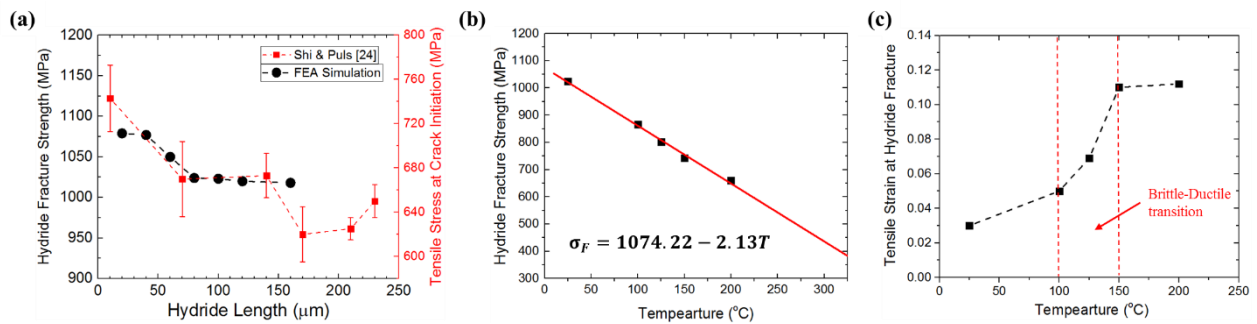


Figure 24. (a) Relation between fracture strength and hydride length at room temperature, (b) fracture strength of hydride at elevated temperatures, (c) global tensile strain at hydride cracking under elevated temperatures.

## 2.5 Discussion

As shown in Figure 22 (d, e), both  $K$  and  $n$  decreases as a function of increasing temperature. This trend indicates the softening behavior of hydride at high temperatures. In current study, the strain rate exponent ( $m$ ) appeared to remain nearly constant at room and elevated temperatures. Furthermore, the lack of information available on the strain rate exponent of hydrides prevented the comparison between results from this study and values reported from other test methods. Two factors that influence the strain rate exponent values are: (i) dislocation interaction induced work hardening; (ii) dislocation annihilation and dislocation offset induced flow softening. At low temperatures, the strain rate exponent has small values as a consequence of the dislocation pile-up and dislocation tangles, while at higher temperatures, diffusion becomes more dominant and facilitates more slip systems to activate. Such changes help the flow softening takes the lead, which can offset the effect of work hardening emerging in high strain-rate deformation. For most metals, the strain rate exponent increases slowly at low temperatures, and increases rapidly as temperature approach more than half the melting temperature [68]. Generally, the strain rate exponent can be used to estimate the tensile ductility of materials [69]. As a consequence, the strain rate exponent remains as a constant with increasing temperature. Such observed trend indicates the lack of change in ductility of hydrides at high temperatures [38].

Experiments from Shi et al. [39] revealed that higher stress levels are required to crack small hydrides [39]. The FEM simulation from the current study corroborates the observations reported by Shi et al. [39]. The variation of fracture strength with respect to hydride length can be attributed to the difference of hydride aspect ratio and misfit residue strain level. Understanding the ductile to brittle transition mechanism in hydrided zircaloy structures is crucial for developing methods to prevent structural failure. The deformation behavior of the ductile zircaloy matrix changes comparatively small over the narrow ductile to brittle transition temperature range (100~150°C). Therefore, it has been hypothesized that there may be a rapid change in the hydride fracture deformation behavior near the ductile to brittle transition temperature [2]. Figure 24 (b) shows that the fracture strength of hydride changes linearly with temperature, and there is no rapid change near the ductile to brittle transition temperature. Another plausible explanation is the variation of yield stress of hydride and zircaloy matrix. As seen in Figure 25 (a), at low temperatures, the yield stress of  $\delta$ -hydride is significantly higher than zircaloy matrix. The resulting mismatch in the work-hardening capability is believed to

impose a higher stress in the hydride precipitates before macroscopic plastic deformation of the matrix. While, as temperature increasing, the yield stress of hydride drops more rapidly than zircaloy matrix and the opposite is observed at the ductile to brittle transition temperature range. At temperatures above 200°C, the yield stress of hydride is observed to be lower than the zircaloy matrix. The strain energy may provide more insight into the deformation behavior of the structure. Figure 25 (b) depicts the strain energy ratio of both phases at different temperatures. As shown, before the transition, hydride phase contributes about 10~12% of the total strain energy. The ratio drops rapidly at the transition temperature region, and at 200°C, the strain energy of hydride is less than 1%. The changing trend in Figure 25 (b) indicates that an increase in temperature facilitates the zircaloy matrix to dictate the plastic deformation of the structure. As a consequence, increase in temperature will result in reduction of tensile stress build up in the hydride phase, and inherently diminish the probability of hydride cracking.

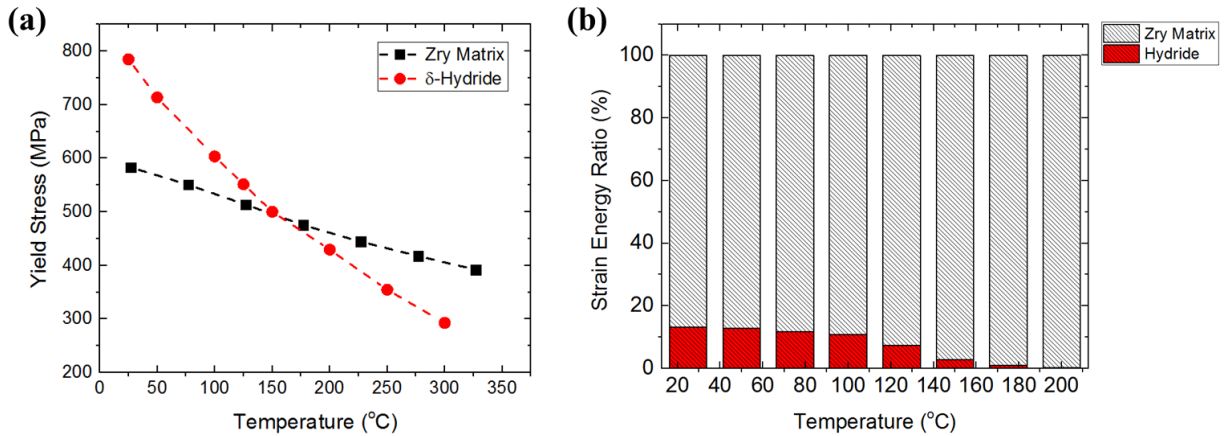


Figure 25. (a) Yield stress vs. temperature, (b) strain energy ratio vs. temperature.

## 2.6 Conclusions

In this study, a method combining nanoindentation, nano-scale impact, and FEM models was developed to obtain a constitutive relation of  $\delta$ -hydride at elevated temperatures. The experimental data was fitted with a power law viscoplasticity model to represent the plastic behavior of  $\delta$ -hydride. Furthermore, a novel approach was used to determine the temperature and strain rate dependent constitutive relation of  $\delta$ -hydride, and a FEM model was developed to estimate the failure strength of hydrides at different temperatures. The FEM model also

facilitated in providing a better understanding of the ductile to brittle transition mechanism in hydrided zircaloy structures. In conclusion, the novel findings of current study are as follows:

- (1) The strength coefficient (K) and strain hardening exponent (n) of hydride decrease with increase in temperature. The observed trend indicates the softening behavior of hydride at elevated temperatures.
- (2) The strain rate exponent (m) of hydride remains almost as a constant as temperature increasing (up to 300°C). The observed trend indicates the lack of change in ductility of hydrides at high temperatures.
- (3) The fracture strength of hydride changes linearly with temperature, and there is no rapid change near the ductile to brittle transition temperature range.
- (4) At room temperature, the hydrides possess a higher yield stress than the zircaloy matrix. An increase in temperature causes the yield stress of hydride decrease more rapidly than that of the zircaloy matrix, the opposite is observed at the ductile to brittle transition temperature range.
- (5) The variation of yield stress of the hydride and the zircaloy matrix can be a plausible reason for the ductile to brittle transition, and the strain energy ratio reveals that at high temperatures (above 200 °C), the plastic deformation is dominated by the zircaloy matrix. A consequence of plastic deformation being dominated by the zircaloy matrix is the reduction in tensile stress buildup and cracking in hydride precipitates.

Few of the limitations in current study are: (1) only two group tests are available for strain rate analysis, and (2) assumption of isotropic material properties for both zircaloy matrix and hydride precipitates. As a solution, indenters with larger tip radius can be used to achieve more strain rates. Furthermore, future studies involving the combination of EBSD measured grain orientation and nano-mechanical experimental methods have been planned, the novel approach of combining nanoindentation, nano-scale impact, and FEM simulations provides the first insight on viscoplastic constitutive relation of  $\delta$ -hydride, and warrants the necessity to be a standalone study.

## **Acknowledgements**

The samples were prepared by Dr. Jun-Li Lin at University of Illinois at Urbana-Champaign and this effort was supported by the U.S. DOE NEUP under contract number IRP-12-4728. This contribution is gratefully acknowledged. HW and VT Acknowledge support from DE-NE0008558.

## 2.7 References

1. Konings, R., *Comprehensive nuclear materials*. 2011: Elsevier.
2. Arthur T. Motta, Laurent Capolungo, Long-Qing Chen, Mahmut Nedim Cinbiz, Mark R. Daymond, Donald A. Koss, Evrard Lacroix, Giovanni Pastore, Pierre-Clément A. Simon, Michael R. Tonks, Brian D. Wirth, and M.A. Zikry, *Hydrogen in zirconium alloys: A review*. Journal of Nuclear Materials, 2019. **Volume 518**: p. Pages 440-460.
3. Barraclough, K. and C. Beevers, *Some observations on the deformation characteristics of bulk polycrystalline zirconium hydrides*. Journal of Materials Science, 1969. **4**(6): p. 518-525.
4. Motta, A.T., L. Capulongo, L.-Q. Chen, M.N. Cinbiz, M. Daymond, D.A. Koss, E. Lacroix, G. Pastore, P.-C. Simon, and M. Tonks, *Hydrogen in zirconium alloys: A review*. Journal of Nuclear Materials, 2019.
5. Puls, M.P., *The effect of hydrogen and hydrides on the integrity of zirconium alloy components: delayed hydride cracking*. 2012: Springer Science & Business Media.
6. Arsene, S. and J. Bai, *A new approach to measuring transverse properties of structural tubing by a ring test*. Journal of testing and evaluation, 1996. **24**(6): p. 386-391.
7. Arsène, S., *Effet de la microstructure et de la température sur la transition ductile-fragile des zircaloy hydrures*. 1997, Châtenay-Malabry, Ecole centrale Paris.
8. Martin-Rengel, M., F.G. Sánchez, J. Ruiz-Hervías, L. Caballero, and A. Valiente, *Revisiting the method to obtain the mechanical properties of hydrided fuel cladding in the hoop direction*. Journal of Nuclear Materials, 2012. **429**(1-3): p. 276-283.
9. Rico, A., M. Martin-Rengel, J. Ruiz-Hervias, J. Rodriguez, and F. Gomez-Sanchez, *Nanoindentation measurements of the mechanical properties of zirconium matrix and hydrides in unirradiated pre-hydrided nuclear fuel cladding*. Journal of nuclear materials, 2014. **452**(1-3): p. 69-76.

10. Bertolino, G., G. Meyer, and J.P. Ipina, *Effects of hydrogen content and temperature on fracture toughness of Zircaloy-4*. Journal of Nuclear Materials, 2003. **320**(3): p. 272-279.
11. Lanin, A., I. Zalivin, V. Turchin, and E. Boiko, *Mechanical properties of zirconium, titanium, and yttrium hydride alloys*. Strength of Materials, 1984. **16**(6): p. 869-876.
12. Gill, B., J. Bailey, and P. Cotterill, *The effects of hydride precipitates on the mechanical properties of zirconium-hydrogen alloys*. Journal of the Less Common Metals, 1975. **40**(1): p. 129-138.
13. Puls, M., S.-Q. Shi, and J. Rabier, *Experimental studies of mechanical properties of solid zirconium hydrides*. Journal of Nuclear Materials, 2005. **336**(1): p. 73-80.
14. Lin, J.-l., X. Han, B.J. Heuser, and J.D. Almer, *Study of the mechanical behavior of the hydride blister/rim structure in Zircaloy-4 using in-situ synchrotron X-ray diffraction*. Journal of Nuclear Materials, 2016. **471**: p. 299-307.
15. Le Saux, M., J. Besson, S. Carassou, C. Poussard, and X. Averty, *Behavior and failure of uniformly hydrided Zircaloy-4 fuel claddings between 25 C and 480 C under various stress states, including RIA loading conditions*. Engineering Failure Analysis, 2010. **17**(3): p. 683-700.
16. Daum, R., S. Majumdar, D. Bates, A. Motta, D. Koss, and M. Billone. *On the embrittlement of Zircaloy-4 under RIA-relevant conditions*. in *Zirconium in the Nuclear Industry: Thirteenth International Symposium*. 2002. ASTM International.
17. Daum, R.S., D.W. Bates, D.A. Koss, and A.T. Motta, *The influence of a hydride layer on the fracture of zircaloy-4 cladding tubes*. 2002, Argonne National Lab., IL (US).
18. Yamanaka, S., M. Kuroda, D. Setoyama, M. Uno, K. Takeda, H. Anada, F. Nagase, and H. Uetsuka, *Analysis of the fracture behavior of a hydrided cladding tube at elevated temperatures by fracture mechanics*. Journal of alloys and compounds, 2002. **330**: p. 400-403.
19. Motta, A.T. and L.-Q. Chen, *Hydride formation in zirconium alloys*. Jom, 2012. **64**(12): p. 1403-1408.
20. Weekes, H., V. Vorontsov, I. Dolbnya, J. Plummer, F. Giuliani, T. Britton, and D. Dye, *In situ micropillar deformation of hydrides in Zircaloy-4*. Acta Materialia, 2015. **92**: p. 81-96.
21. Chan, H., S. Roberts, and J. Gong, *Micro-scale fracture experiments on zirconium hydrides and phase boundaries*. Journal of Nuclear Materials, 2016. **475**: p. 105-112.

22. Kang, S.-K., Y.-C. Kim, K.-H. Kim, J.-Y. Kim, and D. Kwon, *Extended expanding cavity model for measurement of flow properties using instrumented spherical indentation*. International Journal of Plasticity, 2013. **49**: p. 1-15.
23. Dahlberg, C., Y. Saito, M.S. Öztop, and J.W. Kysar, *Geometrically necessary dislocation density measurements associated with different angles of indentations*. International Journal of Plasticity, 2014. **54**: p. 81-95.
24. Seok, M.-Y., Y.-J. Kim, I.-C. Choi, Y. Zhao, and J.-i. Jang, *Predicting flow curves of two-phase steels from spherical nanoindentation data of constituent phases: Isostrain method vs. non-isostrain method*. International Journal of Plasticity, 2014. **59**: p. 108-118.
25. Renner, E., Y. Gaillard, F. Richard, F. Amiot, and P. Delobelle, *Sensitivity of the residual topography to single crystal plasticity parameters in Berkovich nanoindentation on FCC nickel*. International Journal of Plasticity, 2016. **77**: p. 118-140.
26. Saleh, M., Z. Zaidi, M. Ionescu, C. Hurt, K. Short, J. Daniels, P. Munroe, L. Edwards, and D. Bhattacharyya, *Relationship between damage and hardness profiles in ion irradiated SS316 using nanoindentation—Experiments and modelling*. International Journal of Plasticity, 2016. **86**: p. 151-169.
27. Vachhani, S.J., R.D. Doherty, and S.R. Kalidindi, *Studies of grain boundary regions in deformed polycrystalline aluminum using spherical nanoindentation*. International Journal of Plasticity, 2016. **81**: p. 87-101.
28. Zhang, Y., D.P. Mohanty, P. Seiler, T. Siegmund, J.J. Kruzic, and V. Tomar, *High temperature indentation based property measurements of IN-617*. International Journal of Plasticity, 2017. **96**: p. 264-281.
29. Maity, T., K. Prashanth, Ö. Balçi, J. Kim, T. Schöberl, Z. Wang, and J. Eckert, *Influence of severe straining and strain rate on the evolution of dislocation structures during micro-/nanoindentation in high entropy lamellar eutectics*. International Journal of Plasticity, 2018.
30. Saleh, M., A. Xu, C. Hurt, M. Ionescu, J. Daniels, P. Munroe, L. Edwards, and D. Bhattacharyya, *Oblique cross-section nanoindentation for determining the hardness change in ion-irradiated steel*. International Journal of Plasticity, 2019. **112**: p. 242-256.
31. Mao, K., H. Wang, Y. Wu, V. Tomar, and J.P. Wharry, *Microstructure-property relationship for AISI 304/308L stainless steel laser weldment*. Materials Science and Engineering: A, 2018. **721**: p. 234-243.

32. Wang, H., A. Dhiman, H.E. Ostergaard, Y. Zhang, T. Siegmund, J.J. Kruzic, and V. Tomar, *Nanoindentation based properties of Inconel 718 at elevated temperatures: A comparison of conventional versus additively manufactured samples*. International Journal of Plasticity, 2019. **120**: p. 380-394.
33. Rengel, M.M., F. Gomez, A. Rico, J. Ruiz-Hervias, and J. Rodriguez, *Obtention of the constitutive equation of hydride blisters in fuel cladding from nanoindentation tests*. Journal of Nuclear Materials, 2017. **487**: p. 220-228.
34. Suman, S., M.K. Khan, M. Pathak, and R. Singh, *Investigation of elevated-temperature mechanical properties of  $\delta$ -hydride precipitate in Zircaloy-4 fuel cladding tubes using nanoindentation*. Journal of Alloys and Compounds, 2017. **726**: p. 107-113.
35. Kese, K., P. Olsson, A.-M.A. Holston, and E. Broitman, *High temperature nanoindentation hardness and Young's modulus measurement in a neutron-irradiated fuel cladding material*. Journal of Nuclear Materials, 2017. **487**: p. 113-120.
36. Evans, C., *Micromechanisms and micromechanics of Zircaloy-4*. 2014.
37. Cinbiz, M.N., M. Balooch, X. Hu, A. Amroussia, and K. Terrani, *Nanoindentation study of bulk zirconium hydrides at elevated temperatures*. Journal of Alloys and Compounds, 2017. **726**: p. 41-48.
38. Simpson, L. and C. Cann, *Fracture toughness of zirconium hydride and its influence on the crack resistance of zirconium alloys*. Journal of nuclear materials, 1979. **87**(2-3): p. 303-316.
39. Shi, S.-Q. and M. Puls, *Fracture strength of hydride precipitates in Zr-2.5 Nb alloys*. Journal of Nuclear Materials, 1999. **275**(3): p. 312-317.
40. Leitch, B.W. and M.P. Puls, *Finite element calculations of the accommodation energy of a misfitting precipitate in an elastic-plastic matrix*. Metallurgical Transactions A, 1992. **23**(3): p. 797-806.
41. *Standard Specification for Wrought Zirconium and Zirconium Alloy Seamless and Welded Tubes for Nuclear Service (Except Nuclear Fuel Cladding)*. 2017.
42. Pierron, O., D. Koss, A. Motta, and K. Chan, *The influence of hydride blisters on the fracture of Zircaloy-4*. Journal of nuclear materials, 2003. **322**(1): p. 21-35.
43. Chen, W. and B.J. Heuser, *Solubility and kinetic properties of deuterium in single crystal Pd*. Journal of alloys and compounds, 2000. **312**(1-2): p. 176-180.

44. Verma, D. and V. Tomar, *Structural-Nanomechanical Property Correlation of Shallow Water Shrimp (< i> Pandalus platyceros</i>) Exoskeleton at Elevated Temperature*. Journal of Bionic Engineering, 2014. **11**(3): p. 360-370.
45. Verma, D. and V. Tomar, *An investigation into environment dependent nanomechanical properties of shallow water shrimp (Pandalus platyceros) exoskeleton*. Materials Science and Engineering: C, 2014. **44**(0): p. 371-379.
46. Verma, D. and V. Tomar, *An investigation into mechanical strength of exoskeleton of hydrothermal vent shrimp (Rimicaris exoculata) and shallow water shrimp (Pandalus platyceros) at elevated temperatures*. Materials Science and Engineering: C, 2015. **49**(0): p. 243-250.
47. Oliver, W.C. and G.M. Pharr, *An improved technique for determining hardness and elastic modulus using load and displacement sensing indentation experiments*. Journal of materials research, 1992. **7**(6): p. 1564-1583.
48. Broitman, E., *Indentation hardness measurements at macro-, micro-, and nanoscale: a critical overview*. Tribology Letters, 2017. **65**(1): p. 23.
49. Field, J. and M. Swain, *A simple predictive model for spherical indentation*. Journal of Materials Research, 1993. **8**(2): p. 297-306.
50. Kalidindi, S.R. and S. Pathak, *Determination of the effective zero-point and the extraction of spherical nanoindentation stress–strain curves*. Acta Materialia, 2008. **56**(14): p. 3523-3532.
51. Basu, S., A. Moseson, and M.W. Barsoum, *On the determination of spherical nanoindentation stress–strain curves*. Journal of materials research, 2006. **21**(10): p. 2628-2637.
52. Hu, R., C. Prakash, V. Tomar, M. Harr, I.E. Gunduz, and C. Oskay, *Experimentally-validated mesoscale modeling of the coupled mechanical–thermal response of AP–HTPB energetic material under dynamic loading*. International Journal of Fracture, 2017. **203**(1-2): p. 277-298.
53. Prakash, C., I.E. Gunduz, C. Oskay, and V. Tomar, *Effect of interface chemistry and strain rate on particle-matrix delamination in an energetic material*. Engineering Fracture Mechanics, 2018. **191**: p. 46-64.
54. Somekawa, H. and C.A. Schuh, *High-strain-rate nanoindentation behavior of fine-grained magnesium alloys*. Journal of Materials Research, 2012. **27**(9): p. 1295-1302.

55. Fields DS, B.W., *Determination of strain hardening characteristics by torsion testing*. American Society for Testing Materials, 1957. **57**: p. 1259–1272.
56. Calabri, L., N. Pugno, C. Menozzi, and S. Valeri, *AFM nanoindentation: tip shape and tip radius of curvature effect on the hardness measurement*. Journal of Physics: Condensed Matter, 2008. **20**(47): p. 474208.
57. Weck, P.F., E. Kim, V. Tikare, and J.A. Mitchell, *Mechanical properties of zirconium alloys and zirconium hydrides predicted from density functional perturbation theory*. Dalton Transactions, 2015. **44**(43): p. 18769-18779.
58. Lichinchi, M., C. Lenardi, J. Haupt, and R. Vitali, *Simulation of Berkovich nanoindentation experiments on thin films using finite element method*. Thin solid films, 1998. **312**(1-2): p. 240-248.
59. Geelhood, K.J., C.E. Beyer, and W.G. Luscher, *PNNL stress/strain correlation for Zircaloy*. 2008, Pacific Northwest National Lab.(PNNL), Richland, WA (United States).
60. Tsai, J. and C.T. Sun, *Constitutive model for high strain rate response of polymeric composites*. Composites Science and Technology, 2002. **62**: p. 1289-1297.
61. Carpenter, G., *The dilatational misfit of zirconium hydrides precipitated in zirconium*. Journal of Nuclear Materials, 1973. **48**(3): p. 264-266.
62. Tabor, D., *The hardness of metals*. 2000: Oxford university press.
63. De Menibus, A.H., Q. Auzoux, O. Dieye, P. Berger, S. Bosonnet, E. Foy, V. Macdonald, J. Besson, and J. Crépin, *Formation and characterization of hydride blisters in Zircaloy-4 cladding tubes*. Journal of Nuclear Materials, 2014. **449**(1-3): p. 132-147.
64. Pan, Z. and M. Puls, *Internal friction peaks associated with the behaviour of hydrogen in Zr and Zr–2.5 Nb*. Materials Science and Engineering: A, 2006. **442**(1-2): p. 109-113.
65. Cinbiz, M.N., *The effect of stress state on zirconium hydride reorientation*. 2015.
66. Evans, W. and G. Parry, *DEFORMATION BEHAVIOR OF ZIRCALOY-2 CONTAINING DIRECTIONALLY ORIENTED ZIRCONIUM HYDRIDE PRECIPITATES*. Electrochemical Technology (US) Absorbed by J. Electrochem. Soc., 1966. **4**.
67. Kim, J.-S., T.-H. Kim, D.-H. Kook, and Y.-S. Kim, *Effects of hydride morphology on the embrittlement of Zircaloy-4 cladding*. Journal of Nuclear Materials, 2015. **456**: p. 235-245.

68. Hosford, W.F. and R.M. Caddell, *Metal forming: mechanics and metallurgy*. 2011: Cambridge University Press.
69. Yang, X., H. Guo, Z. Yao, and S. Yuan, *Strain rate sensitivity, temperature sensitivity, and strain hardening during the isothermal compression of BT25y alloy*. *Journal of Materials Research*, 2016. **31**(18): p. 2863-2875.

# **CHAPTER 3. AMAGE MODELING OF HYDRIDED STRUCTURE BASED ON EXTENDED GURSON-TVERGAARD-NEEDLEMAN MODEL**

Hao Wang, Vikas Tomar\*

School of Aeronautics and Astronautics, Purdue University-IN, 47907, USA

\*Corresponding author, Phone: (765)-494-3006 Fax: (765) 494-0307 Email: tomar@purdue.edu

Manuscript under Preparation.

## **Abstract**

In this work, a modified Gurson-Tvergaard-Needleman model was used to study the fracture behavior of hydrided zircaloy-4 structures. The model accounts the damage effects from both precipitate debonding in zircaloy matrix and hydride cracking. The ABAQUS user defined subroutine UMAT was used to implement the extended GTN model into ABAQUS/Standard. Axial tensile and ring compression tests were studied by using 3D FEM simulations. The simulations satisfactorily reproduced experimental stress-strain/load-displacement curves. Furthermore, the model successfully predicted the width reduction and the hydride cracking porosity at the fracture surface in axial tensile tests. Good agreement between calculated and experimental results was also achieved for crack initiation prediction in ring compression tests.

**Keywords:** Zircaloy, Hydride, Damage, FEM, GTN Model.

### 3.1 Introduction

Through the life of a fuel rod, there are numerous processes that can potentially impact the integration of the cladding. For instance, during transient events in nuclear reactor operations, the temperature of cladding increases rapidly up to 600°C and a biaxial stress state is induced in the cladding due to the pellet-cladding mechanical interaction (PCMI). The cladding can also be damaged during the handling in casks transportation or stress assisted cracking during the long-term storage. Besides all these processes, the formation of hydrides in cladding during drying may be another very important factor to be considered. In high burnup zircaloy claddings, hydrogen content can reach up to 600 wppm. Due to the thermal diffusion, even higher hydrogen concentration can be observed at the colder outer surface of claddings. Once the solubility limit of hydrogen is reached, the dissolved hydrogen will precipitate as second phase hydride platelets. Most hydride platelets will form the circumferential oriented rim structure near the outer surface of the cladding. While, driven by the hoop stress in the cladding, some hydride platelets may precipitate along the radial direction. These hydrides are extremely brittle and may significantly degrade the mechanical properties of the cladding, which is known as the hydrogen embrittlement effect [1-5].

In the past few decades, the influence of hydrides on the mechanical properties of nuclear fuel cladding has been extensively studied by performing mechanical tests on irradiated and unirradiated hydrided cladding samples. Several different failure models were developed to predict cladding failure in fuel behavior simulation codes, including critical strain criterion, critical strain energy density criterion, and critical strain rate criterion. However, due to the complex microstructure evolution and mechanical loading in cladding, these models cannot fully represent the PCMI induced cladding failure. Therefore, physical based models have been implemented to provide more insights to the material damage and failure mechanisms recently. Rashid et al. [6-8] proposed a damage-based multiphase model considering the cladding being composed of four different phases, undamaged zircaloy-4 matrix, cracked zircaloy-4 matrix, undamaged hydride precipitates, and cracked hydride precipitates. Udagawa et al. [9] used a continuum damage model to predict the failure of cladding during the reactivity initiated accident (RIA). A stored potential energy function based damage model has been developed to describe the damage behavior of zircaloy-4 with arbitrarily orientated hydrides by Chen et al. [10]. Gurson model [11] has also been used extensively to simulate the damage and failure

process of zircaloy structures. Grange et al. [12] successfully applied the Gurson-Tvergaard-Needleman (GTN) model to simulate the ductile fracture of hydrided zircaloy-4 sheets at room temperature. Williams et al. [13] used the GTN model with isotropic perfect plasticity to reproduce the failure of Zr-2.5Nb pressure tube. It has also been used to predict the failure of  $\alpha$ -annealed and  $\beta$ -treated zircaloy-2 and zircaloy-4 by Cockeram et al. [14]. Recently, Saux et al. [15] proposed a modified GTN model to simulate the fracture process of zircaloy-4 with circumferential hydrides under various loading directions and temperatures.

In this work, the extended GTN model [15] was used to study the fracture behavior of hydrided zircaloy-4 structures. Detailed model description is shown in section 3.2. The ABAQUS user defined subroutines UMAT was used to implement the model into ABAQUS/Standard. Single element tests were performed in both 2D and 3D to validate the user subroutine, which is give in section 3.3. In section 3.4, the model is further applied for 3D FEM analysis for axial tensile and ring compression tests. More details of the model, such as partial derivatives and consistent tangent moduli formula are given in the Appendix.

## 3.2 Model Description

### 3.2.1 Pressure Dependent Plasticity Model

Here, the elastic limit of material is defined by the yield function  $\Phi$ , which involves the first and second invariants of the stress tensor. The yield function can be written as [16-18],

$$\Phi(p, q, H^\alpha) = 0. \quad (60)$$

In Eq. (60),  $p$  and  $q$  are the hydrostatic pressure and the von Mises equivalent stress respectively, which are defined as,

$$p = -\frac{1}{3}\sigma_{ii}, \quad (61)$$

$$q = \sqrt{\frac{3}{2}S_{ij}S_{ij}}. \quad (62)$$

In Eq. (60),  $H^\alpha$ ,  $\alpha=1,2,\dots$  are the internal state variables, such as hardening and void volume fraction. The total strain rate can be decomposed into elastic and plastic parts,

$$\dot{\boldsymbol{\varepsilon}} = \dot{\boldsymbol{\varepsilon}}^e + \dot{\boldsymbol{\varepsilon}}^p. \quad (63)$$

Then, following the Hook's law, stress tensor can be calculated from the elastic strain,

$$\boldsymbol{\sigma} = \mathbf{C} : \boldsymbol{\varepsilon}^e. \quad (64)$$

In Eq. (64),  $\mathbf{C}$  is the fourth order elasticity tensor. In the case of isotropic material,  $\mathbf{C}$  can be written as,

$$\mathbf{C} = 2G\mathbf{J}^{\text{sym}} + \left(K - \frac{2}{3}G\right)\mathbf{I} \otimes \mathbf{I}, \quad (65)$$

In Eq. (65),  $K$  is the bulk modulus,  $G$  is the shear modulus,  $\mathbf{I}$  is the second order identity tensor, and  $\mathbf{J}^{\text{sym}}$  is the fourth order symmetric identity tensor.

Considering the associated flow rule, the plastic strain tensor increment direction is normal to the yield surface, which can be written as,

$$\dot{\boldsymbol{\varepsilon}}^p = \dot{\lambda} \frac{\partial \Phi}{\partial \boldsymbol{\sigma}}. \quad (66)$$

In Eq. (66),  $\dot{\lambda}$  is the plastic multiplier, which is a positive scalar factor of proportionality.  $\frac{\partial \Phi}{\partial \boldsymbol{\sigma}}$  gives the flow direction of the plastic strain tensor increment.

The last part in the pressure dependent plasticity model is a set of equations to describe the evolution of internal state variables, which in the form of Eq. (67),

$$\dot{H}^\alpha = h^\alpha(\dot{\boldsymbol{\varepsilon}}^p, \boldsymbol{\sigma}, H^\beta). \quad (67)$$

### 3.2.2 Return Mapping Algorithm and Numerical Integration

Aravas [18] proposed the backward Euler algorithm formulations for the pressure dependent elastoplastic model. In the following, the time step for a variable is indicated by a subscript. Variables at current time step  $t+\Delta t$  are evaluated from known quantities from the previous time step  $t$ . As a convention, the subscript for the current step is omitted. First, the new stress tensor  $\boldsymbol{\sigma}$  can be calculated as,

$$\boldsymbol{\sigma} = \mathbf{C} : (\boldsymbol{\varepsilon}_t^e + \Delta \boldsymbol{\varepsilon}^e) = \mathbf{C} : (\boldsymbol{\varepsilon}_t^e + \Delta \boldsymbol{\varepsilon} - \Delta \boldsymbol{\varepsilon}^p) = \boldsymbol{\sigma}^{\text{tr}} - \mathbf{C} : \Delta \boldsymbol{\varepsilon}^p. \quad (68)$$

In Eq. (68),  $\sigma^{\text{tr}}$  is called the trial stress or the elastic predictor, which is calculated by taking the total strain increment as elastic,

$$\sigma^{\text{tr}} = \mathbf{C} : (\boldsymbol{\varepsilon}_t^e + \Delta \boldsymbol{\varepsilon}). \quad (69)$$

Following the associated flow rule, the plastic strain increment can be written as,

$$\Delta \boldsymbol{\varepsilon}^p = \Delta \lambda \left( \frac{\partial \Phi}{\partial \mathbf{q}} \frac{\partial \mathbf{q}}{\partial \boldsymbol{\sigma}} + \frac{\partial \Phi}{\partial p} \frac{\partial p}{\partial \boldsymbol{\sigma}} \right) = \Delta \lambda \left( \frac{\partial \Phi}{\partial \mathbf{q}} \mathbf{n} - \frac{1}{3} \frac{\partial \Phi}{\partial p} \mathbf{I} \right). \quad (70)$$

In Eq. (70),  $\mathbf{n}$  is a normality tensor parallel to the deviatoric stress,  $\mathbf{n} = 3\mathbf{S}/2q$ . Now, two new variables can be defined, as shown in Eq. (71) and (72),

$$\Delta \varepsilon_q = \Delta \lambda \frac{\partial \Phi}{\partial q}, \quad (71)$$

$$\Delta \varepsilon_p = -\Delta \lambda \frac{\partial \Phi}{\partial p}. \quad (72)$$

By eliminating  $\Delta \lambda$ , Eq. (71) and (72) can be combined as Eq. (73),

$$\Delta \varepsilon_q \frac{\partial \Phi}{\partial q} + \Delta \varepsilon_p \frac{\partial \Phi}{\partial p} = 0. \quad (73)$$

Then the new stress tensor  $\boldsymbol{\sigma}$  can be rewritten as,

$$\begin{aligned} \boldsymbol{\sigma} &= \sigma^{\text{tr}} - \left( 2\mathbf{G}\mathbf{J}^{\text{sym}} + \left( K - \frac{2}{3}G \right) \mathbf{I} \otimes \mathbf{I} \right) : \left( \Delta \varepsilon_q \mathbf{n} + \frac{1}{3} \Delta \varepsilon_p \mathbf{I} \right) \\ &= \sigma^{\text{tr}} - 2G \Delta \varepsilon_q \mathbf{n} - \frac{2}{3} G \Delta \varepsilon_p \mathbf{I} - \left( K - \frac{2}{3} G \right) \Delta \varepsilon_p \mathbf{I} \\ &= \sigma^{\text{tr}} - 2G \Delta \varepsilon_q \mathbf{n} - K \Delta \varepsilon_p \mathbf{I} \end{aligned} \quad (74)$$

The stress can be split into deviatoric and hydrostatic parts,

$$\mathbf{S} = \mathbf{S}^{\text{tr}} - 2G \Delta \varepsilon_q \mathbf{n}, \quad (75)$$

$$p = p^{\text{tr}} + K \Delta \varepsilon_p. \quad (76)$$

It is also clear that the trial deviatoric stress has the same direction with the deviatoric stress,  $\mathbf{n} = 3\mathbf{S}/2q = (3\mathbf{S}^{\text{tr}})/(2q^{\text{tr}})$ . The von Mises equivalent stress can be updated as,

$$q = q^{\text{tr}} + 3G\Delta\varepsilon_q. \quad (77)$$

Now the evolution of the stress tensor and internal state variables of the pressure depend plasticity model can be obtained by solving following non-linear equations,

$$\Delta\varepsilon_q \frac{\partial\Phi}{\partial q} + \Delta\varepsilon_p \frac{\partial\Phi}{\partial p} = 0, \quad (78)$$

$$\Phi(p, q, H^\alpha) = 0, \quad (79)$$

$$p = p^{\text{tr}} + K\Delta\varepsilon_p, \quad (80)$$

$$q = q^{\text{tr}} + 3G\Delta\varepsilon_q, \quad (81)$$

$$\Delta H^\alpha = h^\alpha(\Delta\varepsilon_p, \Delta\varepsilon_q, p, q, H^\beta). \quad (82)$$

These non-linear equations by Newton-Raphson method. According to the work of Aravas [18] and Zhang et al. [19, 20],  $\Delta\varepsilon_q$  and  $\Delta\varepsilon_p$  are chosen and solved as primary unknowns. Eq. (78) and (79) can be solved by using the reduced form of the Newton-Raphson equations after performing Taylor series expansion, as given in Eq. (83) and (84),

$$A_{11}c_p + A_{12}c_q = b_1, \quad (83)$$

$$A_{21}c_p + A_{22}c_q = b_2. \quad (84)$$

Here,  $A_{ij}$  and  $b_i$  are given in Appendix 2. Eq. (83) and (84) are solved for  $c_p$  and  $c_q$ , which are correctors for  $\Delta\varepsilon_p$  and  $\Delta\varepsilon_q$  respectively. Then, the values of  $\Delta\varepsilon_p$  and  $\Delta\varepsilon_q$  can be updated by using Eq. (85) and (86),

$$\Delta\varepsilon_p = \Delta\varepsilon_p + c_p, \quad (85)$$

$$\Delta\varepsilon_q = \Delta\varepsilon_q + c_q. \quad (86)$$

Then  $p$ ,  $q$ , and  $\Delta H^\alpha$  can be updated based on the values of  $\Delta\varepsilon_q$  and  $\Delta\varepsilon_p$  by using Eq. (80)-(82).

### 3.2.3 Derivation of The Consistent Tangent Moduli

To solve non-linear rate-independent elastoplastic problems, Newton's method with an incremental iterative solution procedure is used. At each time step, the non-linear problem is linearized and solved, which requires the tangent stiffness matrix of the structure. Typically, in FEM, this tangent stiffness matrix is computed from the consistent tangent moduli (CTM) of the material, which is obtained by differentiating the incremental constitutive relation with respect to the total incremental strain ( $\partial\Delta\boldsymbol{\sigma}/\partial\Delta\boldsymbol{\epsilon}$ ). It has been shown that the CTM guarantees the quadratic rate of asymptotic convergence of Newton iterative solution schemes [21, 22]. Zhang et al. [19, 20] derived an explicit CTM formula for Euler backward algorithm by separating the hydrostatic and deviatoric components. Details of the derivation are given below.

The deviatoric part of the stress tensor is,

$$\mathbf{S} = \mathbf{S}^{\text{tr}} - 2G\Delta\boldsymbol{\epsilon}_D^p, \quad (87)$$

In Eq. (87),  $\mathbf{S}^{\text{tr}}$  is the deviatoric part of the trial stress tensor,  $\Delta\boldsymbol{\epsilon}_D^p$  is the deviatoric component of plastic strain increment. Rearranging Eq. (87), it becomes,

$$\mathbf{S}^{\text{tr}} = \left(1 + \frac{3G}{q}\Delta\epsilon_q\right)\mathbf{S} = 2G\boldsymbol{\epsilon}_D^{\text{tr}}. \quad (88)$$

By taking inner product with itself, Eq. (88) gives,

$$\left[1 + \left(\frac{3G}{q}\right)\Delta\epsilon_q\right]\sqrt{\frac{3}{2}\mathbf{S}:\mathbf{S}} = 2G\sqrt{\frac{3}{2}\boldsymbol{\epsilon}_D^{\text{tr}}:\boldsymbol{\epsilon}_D^{\text{tr}}}, \quad (89)$$

$$q + 3G\Delta\epsilon_q = q^{\text{tr}}. \quad (90)$$

Differentiating of Eq. (90) yields,

$$\partial q = \partial q^{\text{tr}} - 3G\partial\Delta\epsilon_q = 3G\left[\frac{\mathbf{S}^{\text{tr}}}{q^{\text{tr}}}\partial\boldsymbol{\epsilon}_D^{\text{tr}} - \partial\Delta\epsilon_q\right]. \quad (91)$$

By taking the variation of Eq. (87) with respect to all quantities,

$$\left(1 + \frac{3G}{q} \partial \Delta \varepsilon_q\right) \partial \mathbf{S} + \mathbf{S} \frac{3G}{q} \left(\partial \Delta \varepsilon_q - \frac{\Delta \varepsilon_q}{q} \partial q\right) = 2G \partial \boldsymbol{\varepsilon}_D^{\text{tr}}. \quad (92)$$

By substituting Eq. (91) into Eq. (92) and rearranging, Eq. (92) can be rewritten as,

$$\partial \mathbf{S} = \left(2G \frac{q}{q^{\text{tr}}} \mathbf{J} + \frac{4G^2}{q^{\text{tr}}} \Delta \varepsilon_q \mathbf{n} \otimes \mathbf{n}\right) : \partial \boldsymbol{\varepsilon}_D^{\text{tr}} - 2G \mathbf{n} \partial \Delta \varepsilon_q, \quad (93)$$

In Eq. (93),  $\mathbf{J}$  is the fourth order unit tensor. For all cases in which direct strains are defined by a kinematic solution,

$$\partial \boldsymbol{\varepsilon}_D^{\text{tr}} = \left[\mathbf{J} - \frac{1}{3} \mathbf{I} \otimes \mathbf{I}\right] : \partial \boldsymbol{\varepsilon}, \quad (94)$$

$$\partial p = -K \mathbf{I} : \partial \boldsymbol{\varepsilon} + K \partial \Delta \varepsilon_p. \quad (95)$$

By differentiating Eq. (74) and using Eqs. (93) and (94), it gives,

$$\partial \boldsymbol{\sigma} = \mathbf{Z} : \partial \boldsymbol{\varepsilon} - K \mathbf{I} \partial \Delta \varepsilon_p - 2G \mathbf{n} \partial \Delta \varepsilon_q, \quad (96)$$

with

$$\mathbf{Z} = 2G \frac{q}{q^{\text{tr}}} \mathbf{J} + \left(K - \frac{2G}{3} \frac{q}{q^{\text{tr}}}\right) \mathbf{I} \otimes \mathbf{I} + \frac{4G^2}{q^{\text{tr}}} \Delta \varepsilon_q \mathbf{n} \otimes \mathbf{n}. \quad (97)$$

For the general pressure-dependent elastoplasticity model, Aravas [18] proposed the following equations,

$$\bar{A}_{11} \partial \Delta \varepsilon_p + \bar{A}_{12} \partial \Delta \varepsilon_q = (\mathbf{B}_{11} \mathbf{I} + \mathbf{B}_{12} \mathbf{n}) : \partial \boldsymbol{\sigma}, \quad (98)$$

$$\bar{A}_{21} \partial \Delta \varepsilon_p + \bar{A}_{22} \partial \Delta \varepsilon_q = (\mathbf{B}_{21} \mathbf{I} + \mathbf{B}_{22} \mathbf{n}) : \partial \boldsymbol{\sigma}. \quad (99)$$

Coefficients  $\bar{A}_{ij}$  and  $B_{ij}$  are given in Appendix 3. Now by substituting  $\partial \boldsymbol{\sigma}$  into Eqs. (95) and (96), it can be written as,

$$\partial \Delta \varepsilon_p = (\mathbf{C}_{11} \mathbf{I} + \mathbf{C}_{12} \mathbf{n}) : \mathbf{Z} : \partial \boldsymbol{\sigma}, \quad (100)$$

$$\partial\Delta\varepsilon_q = (C_{21}\mathbf{I} + C_{22}\mathbf{n}) : \mathbf{Z} : \partial\boldsymbol{\sigma}. \quad (101)$$

Coefficients  $C_{ij}$  are given in Appendix 4. By substituting Eqs.(100) and (101) into Eqs.(96), it yields an expression for the CTM for the backward Euler algorithm,

$$\partial\boldsymbol{\sigma} = \mathbf{M} : \mathbf{Z} : \partial\boldsymbol{\varepsilon}, \quad (102)$$

where

$$\mathbf{M} = \mathbf{J} - \mathbf{M}^I - \mathbf{M}^n, \quad (103)$$

$$\mathbf{M}^I = K(C_{11}\mathbf{I} \otimes \mathbf{I} + C_{12}\mathbf{I} \otimes \mathbf{n}), \quad (104)$$

$$\mathbf{M}^n = 2G(C_{21}\mathbf{n} \otimes \mathbf{I} + C_{12}\mathbf{n} \otimes \mathbf{n}). \quad (105)$$

Finally, by plugging in  $\mathbf{M}$  and  $\mathbf{Z}$ , the CTM can be explicitly expressed as,

$$\mathbf{D} = d_0\mathbf{J} + d_1\mathbf{I} \otimes \mathbf{I} + d_2\mathbf{n} \otimes \mathbf{n} + d_3\mathbf{I} \otimes \mathbf{n} + d_4\mathbf{n} \otimes \mathbf{I}, \quad (106)$$

with the five constants,

$$d_0 = 2G \frac{q}{q^{\text{tr}}}, \quad (107)$$

$$d_1 = K - \frac{2G}{3} \frac{q}{q^{\text{tr}}} - 3K^2 C_{11}, \quad (108)$$

$$d_2 = \frac{4G^2}{q^{\text{tr}}} \Delta\varepsilon_q - 4G^2 C_{22}, \quad (109)$$

$$d_3 = -2GKC_{12}, \quad (110)$$

$$d_4 = -6GKC_{21}. \quad (111)$$

It's worth to notice that  $\mathbf{D}$  is symmetric if  $C_{12} = 3C_{21}$  [20, 23].

### 3.2.4 GTN Yield Function And Internal State Variables

By studying the plastic flow of a spherical cell with a concentric spherical void, Gurson [11] provided a yield function for a porous plastic solid,

$$\Phi = \left(\frac{q}{\sigma_f}\right)^2 + 2q_1 f \cosh\left(\frac{3}{2} \frac{q_2 p}{\sigma_f}\right) - (1 + q_1^2 f^2) = 0. \quad (112)$$

In Eq. (112),  $q$  is the macroscopic von Mises equivalent stress,  $p$  is the macroscopic pressure,  $\sigma_f$  is the flow stress of the fully dense matrix as a function of the equivalent plastic strain, and  $f$  is the void volume fraction.  $q_1$  and  $q_2$  are two parameters introduced by Tvergaard to get better prediction from the numerical analysis.

There are two internal state variables in the Gurson model, one is the void volume fraction  $f$ , and the other one is the matrix equivalent plastic strain  $\varepsilon_{eq}^m$ . The evolution of the void volume fraction can be written as,

$$\dot{f} = \dot{f}_{gr} + \dot{f}_{nucl}. \quad (113)$$

It means the growth of the total void volume fraction includes both the growth of existing voids ( $\dot{f}_{gr}$ ) and the nucleation of new voids ( $\dot{f}_{nucl}$ ). The growth of existing voids is controlled by volumetric strain increments, given in Eq. (114),

$$\dot{f}_{gr} = (1 - f)\dot{\varepsilon}_p. \quad (114)$$

The nucleation of new voids is controlled by the equivalent plastic strain of the matrix, given in Eq. (115),

$$\dot{f}_{nucl} = A\dot{\varepsilon}_{eq}^m. \quad (115)$$

In Eq. (115),  $A$  is a parameter that controls the nucleation process of voids. Chu et al. [24] provided a specific form for  $A$  which ensures the void nucleation follows a normal distribution,

$$A = \frac{f_N}{S_N\sqrt{2\pi}} \exp\left[-\frac{1}{2}\left(\frac{\varepsilon_{eq}^m - \varepsilon_N}{S_N}\right)^2\right]. \quad (116)$$

Here,  $f_N$  is the volume fraction of particles or inclusions as void nucleus,  $\varepsilon_N$  is the mean strain for void nucleation, and  $S_N$  is the corresponding standard deviation. Typically, no void

nucleation and growth are assumed in compressive stress ( $p > 0$ ). Then the evolution of internal state variables can be written in following finite difference form,

$$\Delta H_1 = h_1 = \Delta \varepsilon_{eq}^m = \frac{-p \Delta \varepsilon_p + q \Delta \varepsilon_q}{(1-f)\sigma_f}, \quad (117)$$

$$\Delta H_2 = h_2 = \Delta f = (1-f)\Delta \varepsilon_p + A \Delta \varepsilon_{eq}^m. \quad (118)$$

Later, Tvergaard et al. [25] modified the Gurson model,

$$\Phi = \left(\frac{q}{\sigma_f}\right)^2 + 2q_1 f^* \cosh\left(\frac{3}{2} \frac{q_2 p}{\sigma_f}\right) - (1 + q_1^2 f^{*2}) = 0. \quad (119)$$

In Eq. (119),  $f^*$  is the representative void volume fraction to account the void coalescence effect.

$$f^* = \begin{cases} f & f \leq f_c \\ f_c + \frac{(f - f_c)(f_u^* - f_c)}{f_f - f_c} & f > f_c \end{cases} \quad (120)$$

Eq. (120),  $f_c$  is the critical void volume fraction for void coalescence,  $f_f$  is the real void volume fraction at final failure,  $f_u^*$  is the value of the representative void volume fraction  $f^*$  at final failure.

### 3.2.5 Damage Description of Hydrided Structure

As discussed previously, the total void volume contains contributions from both nucleation of new voids and growth of existing voids. There are two sources for void nucleation in hydrided zircaloy, one is the interface debonding between Laves phase precipitates and the zircaloy matrix [5], and the other one is hydride cracking induced micro-cracks [26]. Gologanu et al. [27] proposed an extended GTN model for ellipsoidal voids and showed that micro-crack can be considered as a void with the same projected area. Then, following the model proposed by Saux et al. [15], the total void nucleation can be written as,

$$\dot{f}_{nucl} = \dot{f}_{nucl}^L + \dot{f}_{nucl}^H. \quad (121)$$

Eq. (121),  $\dot{f}_{\text{nucl}}^L$  is the void nucleation from Laves phase precipitates debonding, and  $\dot{f}_{\text{nucl}}^H$  is the void nucleation from hydride cracking. Assuming both  $\dot{f}_{\text{nucl}}^L$  and  $\dot{f}_{\text{nucl}}^H$  follow the void nucleation function described in Eq. (116), then Eq. (115) can be written as,

$$\dot{f}_{\text{nucl}} = [A_L(f_N^L, \varepsilon_N^L, S_N^L) + A_H(f_N^H, \varepsilon_N^H, S_N^H)]\dot{\varepsilon}_{\text{eq}}^m. \quad (122)$$

The nucleation function parameters  $f_N$ ,  $S_N$ , and  $\varepsilon_N$  can be different for Laves phase precipitates debonding and hydride cracking. Therefore, superscripts L and H are used to separate them for each case. The mechanical degradation caused by hydride cracking has been accounted through the void nucleation.

Experimental observation shows that cracks in circumferential hydrides will propagate through hydride thickness and stop at hydride-matrix interface [26, 28, 29]. Therefore, the hydride cracking induced micro-cracks should not be counted in the void growth calculation. Then Eq. (114) should be modified as,

$$\dot{f}_{\text{gr}} = (1 - f_p)\dot{\varepsilon}_p. \quad (123)$$

Here,  $f_p$  is the void volume fraction which needs to be counted in the void growth calculation. More specifically, it can be estimated by subtracting the hydride cracking induced void volume from the total void volume,

$$f_p = f - f_{\text{nucl}}^H. \quad (124)$$

So far, the damage description of hydrided structure has been completed.

### 3.3 GTN UMAT Validation

The default strain measure in ABAQUS/Standard is the “integrated” strain, which is obtained by integrating the strain rate numerically in a material frame [30]. This strain measure is appropriate for elastic-(visco)plastic or elastic-creeping materials. The Gurson model was implemented in ABAQUS v6.14 by using the UMAT subroutine [30]. Validations are needed to check the numerical results of present implementation. Two test cases are performed based on the suggestion of Zhang et al. [31], one is the uni-axial tensile of a 2D plane strain element and the other one is the hydrostatic tension of a 3D cubic element.

### 3.3.1 A Single Plane Strain Element Under Tensile Loading

First, a plane strain element was tested under uni-axial loading condition. The element size is 4mm×4mm. The loading and boundary conditions are shown in Figure 26 (a). Using the equations given in previous sections and enforcing the consistency condition to determine  $d\lambda$ , Zhang et al. [31] gives the following equations to describe the problem:

$$\frac{d\varepsilon_y^p}{d\varepsilon_y} = \omega \frac{3(\sigma_y - \sigma_z)}{\sigma_f^2}, \quad (125)$$

$$\frac{d\sigma_f}{d\varepsilon_y} = \frac{E}{1 - \nu^2} \left[ 1 - \omega \frac{3(\sigma_y - \sigma_z)}{\sigma_f^2} \right], \quad (126)$$

$$\frac{df}{d\varepsilon_y} = \omega \Lambda_f, \quad (127)$$

$$\frac{d\varepsilon_{eq}^m}{d\varepsilon_y} = \omega \Lambda_\varepsilon, \quad (128)$$

where

$$\omega = \frac{E\phi_{\sigma_y}}{1 - \nu^2} / \left[ \frac{E\phi_{\sigma_y}}{1 - \nu^2} \frac{3(\sigma_y - \sigma_z)}{\sigma_f^2} - \phi_f \Lambda_f - \phi_{\sigma_f} \frac{d\sigma_f}{d\varepsilon_{eq}^m} \Lambda_\varepsilon \right], \quad (129)$$

$$\phi_{\sigma_y} = \frac{q_1 q_2 f}{\sigma_f} \sinh\left(-\frac{3q_2 p}{2\sigma_f}\right) + \frac{2(\sigma_y - \sigma_z)}{\sigma_f^2}, \quad (130)$$

$$\phi_f = 2q_1 \cosh\left(-\frac{3q_2 p}{2\sigma_f}\right) + 2q_1^2 f, \quad (131)$$

$$\phi_{\sigma_f} = \frac{-2q^2}{\sigma_f^3} + \frac{3q_1 q_2 f p}{\sigma_f^2} \sinh\left(-\frac{3q_2 p}{2\sigma_f}\right), \quad (132)$$

$$\Lambda_\varepsilon = \frac{3\sigma_y(\sigma_y - \sigma_z)}{(1 - f)\sigma_f^3}, \quad (133)$$

$$\Lambda_f = \frac{3(1 - f)(\sigma_y - 2\sigma_z)}{\sigma_f^2} + A\Lambda_\varepsilon, \quad (134)$$

$$q = \sqrt{\sigma_y^2 + \sigma_z^2 - \sigma_y \sigma_z}, \quad (135)$$

$$p = -\frac{\sigma_y + \sigma_z}{3}. \quad (136)$$

In above equations, E and v are Young's modulus and Poisson's ratio,  $\epsilon_y$  and  $\epsilon_y^p$  are total strain and plastic strain in the y direction, A is the void nucleation function.

A 4-node linear plane strain element (CPE4) in ABAQUS was used for the finite element analysis. The material constants are detailed in Table 10. The exact solution of the problem can be numerically obtained by integrating above equations by using a forward Euler method. To ensure the accuracy, the total increment was set as 200,000. The comparisons between FE results obtained by user defined subroutines and the exact results are shown in Figure 26 (b, c). Figure 26 (b) shows the von Mises stress in the plane strain element as a function of the total strain along the y-direction. Figure 26 (c) shows the total void volume fraction evolution as a function of the total strain. As shown, the results of the FE analysis agree very well with the exact solutions.

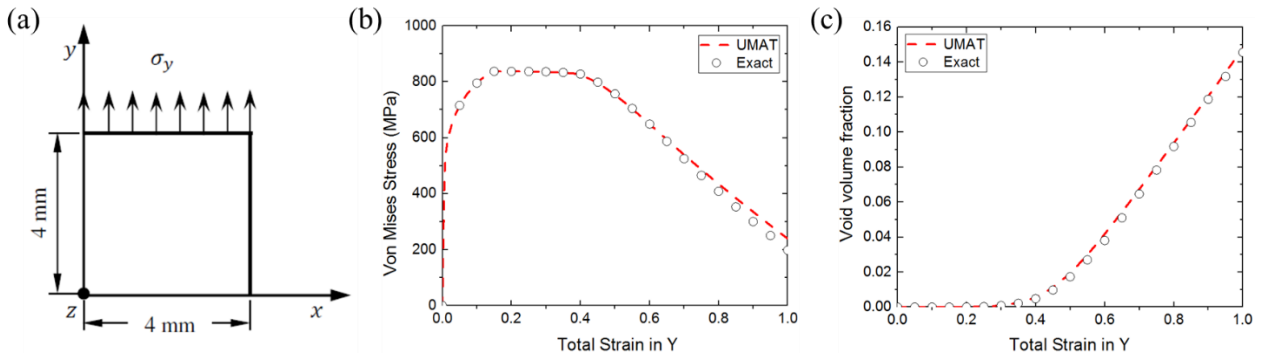


Figure 26. (a) A 2D plane strain element under the uniaxial tensile test, (b) the von Mises stress as a function of strain in Y direction, (c) the void volume fraction as a function of strain in Y direction.

Table 10. Model parameters used for calibrations.

E(GPa)	v	q <sub>1</sub>	q <sub>2</sub>	q <sub>3</sub>	f <sub>0</sub>	f <sub>N</sub>	ε <sub>N</sub>	S <sub>N</sub>	f <sub>c</sub>	f <sub>f</sub>
80	0.342	1.5	1.0	2.25	0	0.04	0.5	0.1	0.0045	0.15

### 3.3.2 A 3D Cubic Element Under Tensile

Second, a 3D cubic element was tested under hydrostatic condition. The element size is 4mm×4mm×4mm. The loading and boundary conditions are shown in Figure 27 (a). By using the similar method, equations for this case can be written as [18, 31]:

$$\frac{d\sigma_x}{d\varepsilon_v} = \frac{K\Lambda}{\Lambda + 9\beta^2 K'} \quad (137)$$

$$\frac{d\varepsilon_{eq}^m}{d\varepsilon_v} = \frac{3\beta^2 K}{\Lambda + 9\beta^2 K} \frac{\varpi}{1-f} \quad (138)$$

$$\frac{df}{d\varepsilon_v} = \left[ 3(1-f) + \frac{A\varpi}{1-f} \right] \frac{3\beta^2 K}{\Lambda + 9\beta^2 K} \quad (139)$$

Here K is the bulk modulus,  $\varepsilon_v$  is the volumetric strain, some other parameters are listed as following,

$$\varpi = \frac{3\sigma_x}{\sigma_f}, \quad (140)$$

$$\Lambda = \frac{\beta\varpi}{1-f} \left[ \frac{d\sigma_f}{d\varepsilon_{eq}^m} \beta\varpi - A \frac{\phi_f}{2} \sigma_f \right] - 3\sigma_f \beta \frac{\phi_f}{2} (1-f), \quad (141)$$

$$\beta = \frac{1}{2} q_1 q_2 f \sinh\left(\frac{1}{2} q_2 \varpi\right), \quad (142)$$

$$\phi_f = 2q_1 \cosh\left(\frac{1}{2} q_2 \varpi\right) - 2q_1^2 f. \quad (143)$$

Here, A is the void nucleation function.

A 8-node brick element (C3D8) in ABAQUS was used for the finite element analysis. The material constants are same as the plane strain test. The comparisons between FE results obtained by user defined subroutines and the exact results are shown in Figure 27 (b, c). Figure 27 (b) shows the von Mises stress in the plane strain element as a function of the total strain along the y-direction. Figure 27 (c) shows the total void volume fraction evolution as a function of the total strain. As shown, the results of the FE analysis agree very well with the exact solutions.

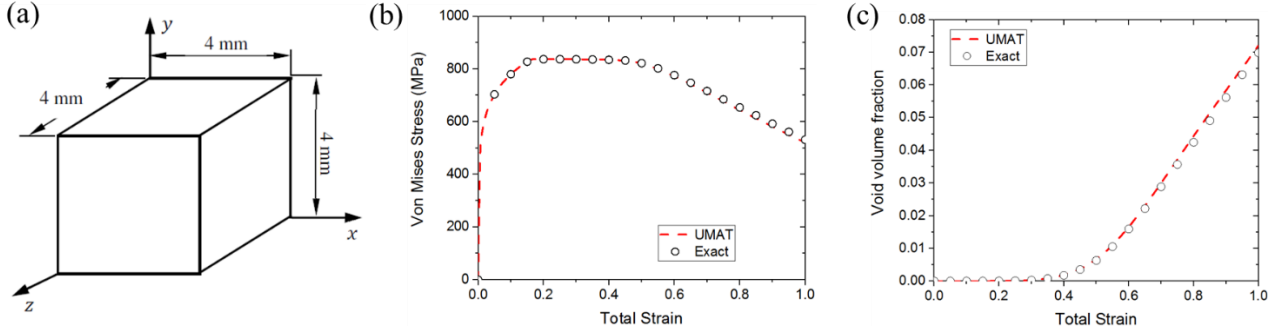


Figure 27. (a) A 3D cubic element used for the hydrostatic tensile test, (b) the von Mises stress as a function of strain in Y direction, (c) the void volume fraction as a function of strain in Y direction.

### 3.4 Application of The Model

The model was used to simulate two test cases, one is the axial tensile test and the other one is the ring compression test. These cases represent the two typical loading scenarios of cladding during services, loading along axial and hoop directions. It has been observed in many studies that the hydride cracking mainly happens at low temperatures. At high temperatures (above 200°C), hydrided zircaloy structures can still remain ductile. Moreover, the hydride induced failures mostly happen during the dry cask storage period. Therefore, only room temperature tests are studied here.

#### 3.4.1 Axial Tensile Test

The model was used to simulate an axial tensile test of zircaloy-4 specimen with circumferential hydrides, and the results are compared with experimental data presented by Saux et al. [26]. A 3D tensile test specimen was created, and dimensions of the specimen is shown in Figure 28 (a). The specimen is fixed on the bottom surface and pulled on the top surface. Eight-node brick elements (C3D8) in ABAQUS was used for the finite element analysis. It is known that the mesh size plays an important role to the analysis of material damage. The mesh size can be related to the metallurgical parameters of the material, such as grain size or inclusion density [32, 33]. The mesh size for recrystallized zircaloy-4 was suggested to be 50×50×50 μm [34]. While, in order to satisfy both analysis accuracy and computational efficiency, a mesh size of

100×100×100 μm has also been used for hydrided zircaloy-4 analysis [15]. Here, the element size between two gauges was chosen to be 100×100×100 μm, as shown in Figure 28 (b). Isotropic material property was considered for the hydrided zircaloy-4 specimen. The material constants and model parameters are detailed in Table 11.

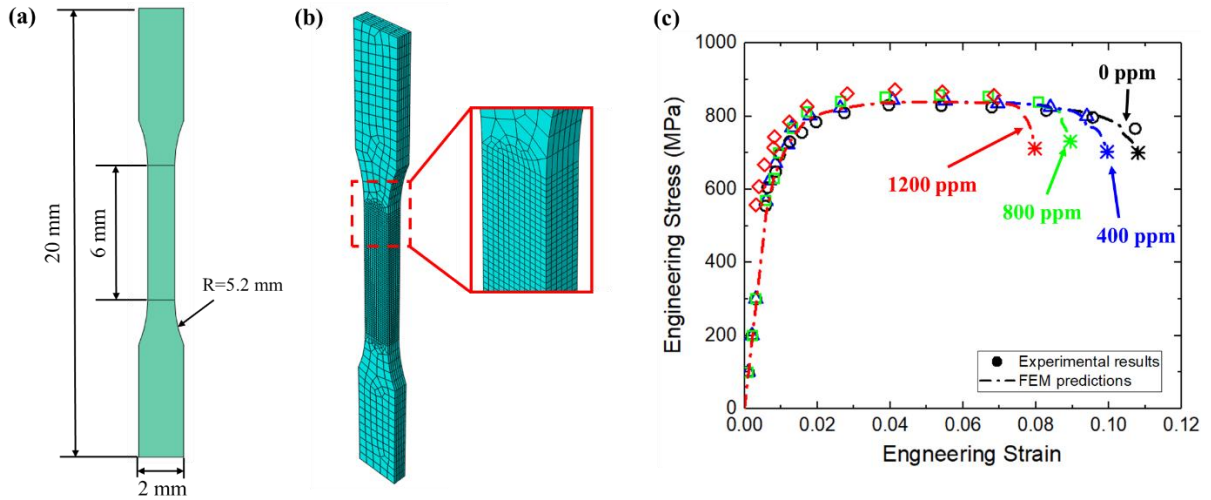


Figure 28. (a) Dimensions of the axial tensile specimen, (b) mesh of the FEM model, (c) comparison of stress-strain curves between experimental results and FEM predictions.

Figure 28 (c) depicts a direct comparison between experimental results and FEM predictions. The strain is determined from the change of distance between gauges. The stress-strain curves have been correctly reproduced for specimen with a hydrogen content up to 800 wppm. The model successfully captures the hydride embrittlement effect that the fracture strain decreases with the increase of hydrogen concentration.

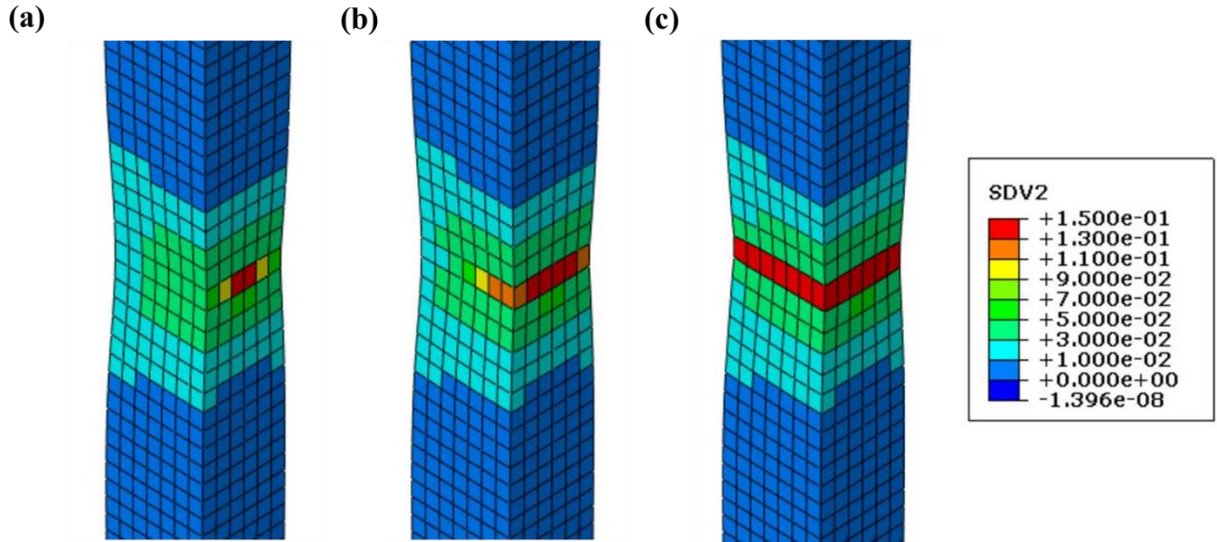


Figure 29. Distribution of total void volume fraction at different stages (mid-plane cross-section of the tensile specimen): (a) crack initiation in the center of specimen, (b) crack propagation, (c) final failure.

Figure 29 shows the total void volume fraction field at different stages of the tensile test. Figure 29 (a) depicts the porosity field at crack initiation. Due to the local necking effect, stress triaxiality is higher in the center of the specimen which leads to a faster void growth. When the critical void volume fraction is reached, void coalescence starts and forms micro-cracks. Then, these micro-cracks propagate outward through the specimen (as shown in Figure 29 (b)) and lead to final failure of the specimen (as shown in Figure 29 (c)). Figure 30 (a) shows the porosity induced by hydride cracking at final failure for different hydrogen content condition. It can be seen, the porosity contribution from hydride cracking increases as hydrogen concentration increasing. At 400 wppm, the hydride cracking porosity is only about 13% of the total porosity. While at 1200 wppm, the hydride cracking porosity grows up to around 33% of the total porosity. Experimental observation shows that cracks in circumferential hydrides will propagate through hydride thickness and stops at the hydride-matrix interface [26, 28, 29]. Then the high stress field around crack tip will induce void growth, coalescence and ductile failure of surrounding matrix. Therefore, the increase of hydride cracking porosity can significantly accelerate the fracture process of the specimen and cause a ductile to brittle transition.

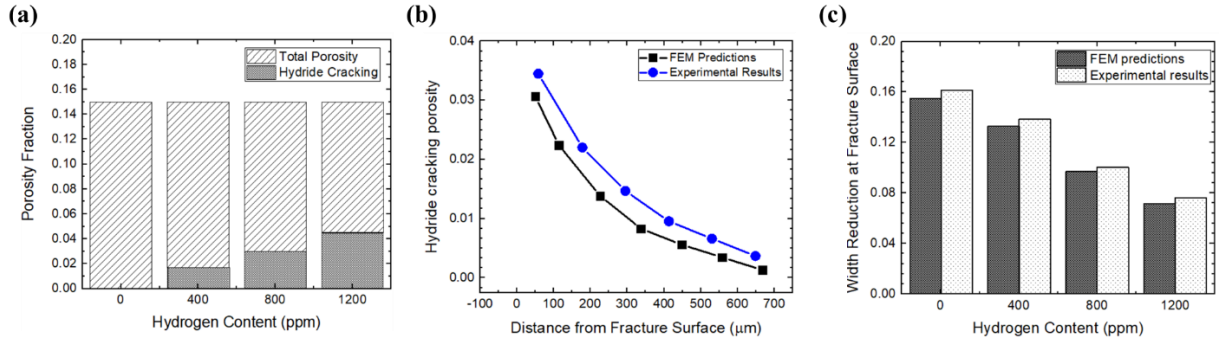


Figure 30. (a) comparison between total void volume fraction and porosity induce by hydride cracking at final failure, (b) hydride cracking porosity as a function of the distance from fracture surface (1200 wppm), (c) width reduction at the failure surface as a function of hydrogen concentration in the specimen.

Figure 30 (b) compares the hydride cracking porosity as a function of the distance from fracture surface between both the experimental observation and the FEM prediction. The FEM result is slightly lower than the experimental observation. Such difference can be induced by parameters of the void nucleation function. Figure 30 (c) shows width reduction at failure surface as a function of hydrogen concentration from both experiments and FEM simulations. It can be seen that simulations slightly underestimate the width reductions at the failure surface. This difference can be attribute to the absence of anisotropic material properties in the FEM model. Moreover, the inaccurate plastic stress-strain curves may also contribute to such difference.

Table 11. Model parameters used for axial tensile test and ring compression test ( $C_H$  is the hydrogen content in wppm).

Zircaloy matrix void nucleation	$f_N^L$		$\varepsilon_N^L$		$S_N^L$
	0.005		0.15		0.05
Hydride cracking	$f_N^H$		$\varepsilon_N^H$		$S_N^H$
	$6.675 \times 10^{-5} C_H$		$-1.438 \times 10^{-4} C_H + 0.333$		$-2.5 \times 10^{-5} C_H + 0.06$
Void coalescence	$q_1$	$q_2$	$q_3$	$f_c$	$f_f$
	1.5	1	2.25	0.0045	0.15

### 3.4.2 Ring Compression Test

Then, the model was used to simulate ring compression tests of hydrided zircaloy-4 specimen, and the results are compared with experimental data presented by Kim et al. [35]. The cladding tube has an outer diameter of 9.5mm, and the thickness is 0.57mm. Due to the symmetry, only half of the ring was modeled, as shown in Figure 31 (a). To reduce the computation cost of the FEM model, the length of the ring specimen was changed from 10mm in experiments to 4mm in the FEM model. Figure 31 (b) shows the mesh of the model. Eight-node brick elements (C3D8) in ABAQUS was used for the FEM analysis. It was suggested to have at least 10 elements through the thickness of the ring specimen for through wall crack analysis [36]. Therefore, the element size through the wall thickness was selected as 50 $\mu$ m, which gives 11 elements along the wall thickness. The element size along the axial direction was selected as 100  $\mu$ m to achieve a balance between accuracy and computational cost. Figure 31 (c) depicts the boundary conditions for the half ring model, the mid-surface was only allowed to move along the loading direction (y-direction). Two rigid planes were created to model the upper and lower loading platen. Hard contact with a friction coefficient of 0.25 was used between the rigid planen and the ring specimen. The model parameters are detailed in Table 11.

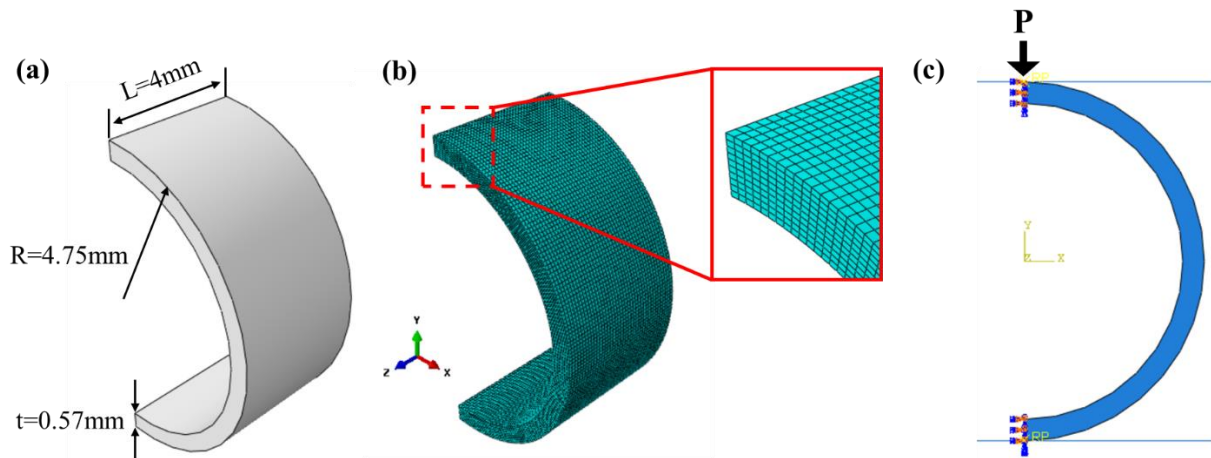


Figure 31. Details of the ring compression test model: (a) geometry of the specimen, (b) mesh of the specimen, (c) boundary conditions.

Figure 32 (a) shows the device and deformed specimen during a ring compression test. The stress state in the specimen during a ring compression test is more complicated than an axial tensile test.

Figure 32 (b) depicts the pressure field in a deformed specimen. The red color indicates a positive pressure, which means compression (C) in the specimen. While the blue color indicates a negative pressure, which means tension (T) in the specimen. It can be seen that the tension and compression always appear together on the opposite side of the ring specimen. The maximum tension and compression were found to be in regions at 0 and 90 degrees. For convenience, these regions are ordered clockwise from 1 to 4, as shown in

Figure 32 (b). Normally, material failures are caused by tension, therefore cracks are expected to initiate on the outer surface of spot 1 and 3, and the inner surface of spot 2 and 4.

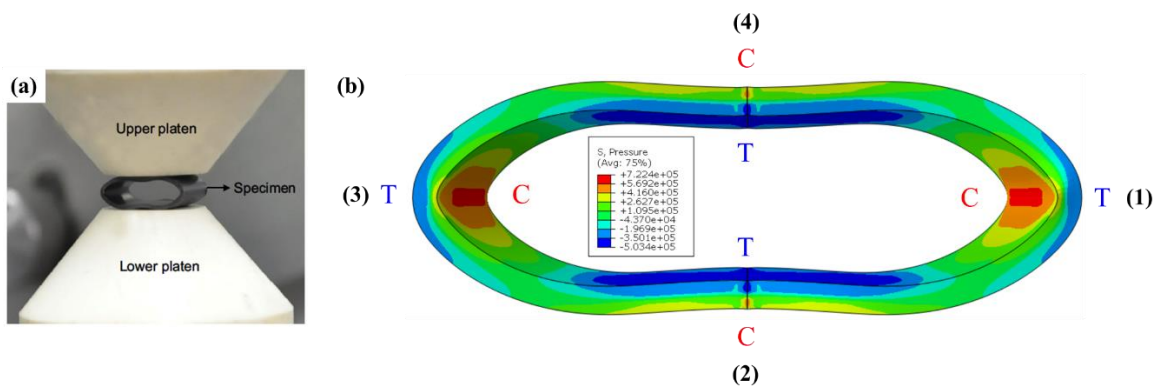


Figure 32. (a) Ring compression test device and specimen, (b) pressure distribution in the specimen during a ring compression test (mirror display from half ring model).

The load-displacement curve of ring compression tests is sensitive to the specimen dimension. Thus, the load was normalized by dividing the length of the specimen. The displacement was measured from the upper loading platen. Figure 33 shows the comparison of load-displacement curves between experimental measurements and FEM predictions. The GTN model successfully reproduced the experimental load-displacement curves. The result also shows an obvious reduction in ductility with the increasing of hydrogen concentration in the structure.

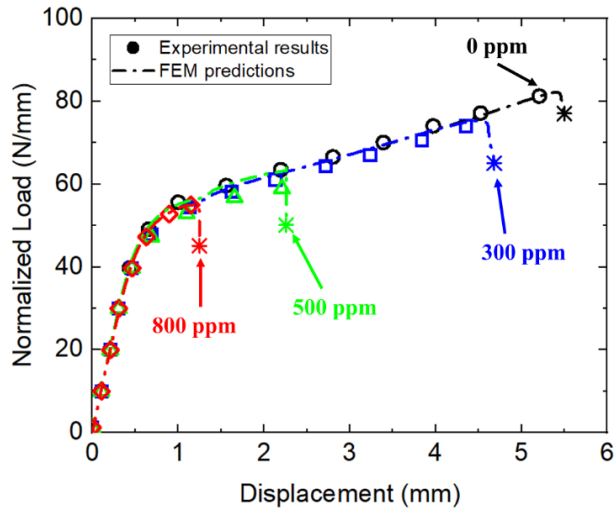


Figure 33. Normalized load–displacement curve of zircaloy-4 ring compression tests with circumferential hydrides at room temperature.

As hydrogen concentration increases from 300 wppm to 500 wppm, the specimen fracture displacement drops significantly, which indicates a ductile to brittle transition in the structure. Thus, detailed investigations are needed to understand the relation between the failure process and hydrogen content of the structure. To demonstrate the fracture behavior of a specimen with low hydrogen content, Figure 34 is taken from Kim et al. [35], which shows the deformation and crack profile of a specimen with hydrogen content of 176 wppm. As shown in Figure 34 (a), the specimen remains ductile with such hydrogen content. As deformation goes, cracks form on the outer surface of spot 1 and 3. Figure 34 (b) shows detailed hydride morphology and crack profiles at all 4 spots.

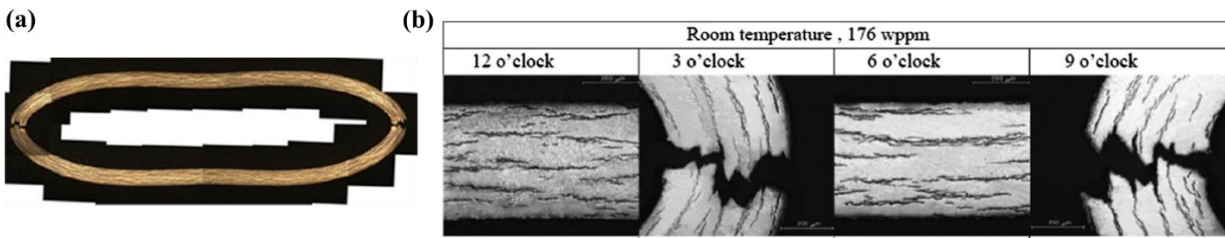


Figure 34. Fracture of a hydrided zircaloy-4 specimen with low hydrogen content after ring compression tests, (a) ductile deformation with cracks at horizontal spots, (b) hydride morphology and crack development at different spots [35].

Figure 35 (a, c) depict the FEM predicted crack profile from different view for a specimen with hydrogen content of 300 wppm. The FEM model predicts that cracks will initiate at horizontal spots which agrees with the experimental observation. Figure 35 (b) displays a cross section of the specimen cut by X-Y plane. It shows that the crack initiates from the outer surface and grows along the radial direction. Figure 35 (c) displays a cross section of the specimen cut by X-Z plane. It clearly shows that a semi-elliptical surface crack is formed during the ring compression test. The major axis of the semi-elliptical surface crack is along the axial direction, which indicates the crack grows faster in the axial direction. Such anisotropic crack growth is controlled by the stress state in the structure. As shown in

Figure 32 (b), the tension stress on the outer surface of spot 1 and 3 leads to a faster crack growth along the axial direction. While, along the radial direction, from outer surface to inner surface, the stress state changes from tension to compression. Such transition in stress state significantly slows down the crack propagation in the radial direction.

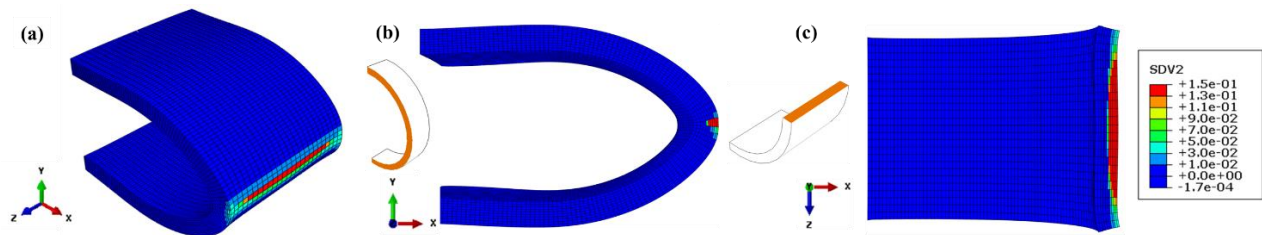


Figure 35. FEM predicted crack profile for a specimen with hydrogen concentration of 300 wppm, the crack initiates on the outer surface at spot 1.

Figure 36 (a, b) is taken from Kim et al. [35], which shows the deformation and crack profile of a specimen with hydrogen content of 562 wppm. Comparing Figure 36 (a) with Figure 34 (a), as hydrogen concentration increases from 176 wppm to 562 wppm, the ductility of the specimen reduces dramatically. Moreover, instead of cracking only at horizontal spots (spot 1 and 3), cracks first initiate on the inner surface at vertical spots (spot 2 and 4). Detailed hydride morphology and crack profiles are shown in Figure 36 (b). The crack at spot 4 penetrates the whole structure and causes the final failure. However, as deformation continues, cracks start to form at horizontal spots as well. The reason for crack formation at different spots will be discussed later.

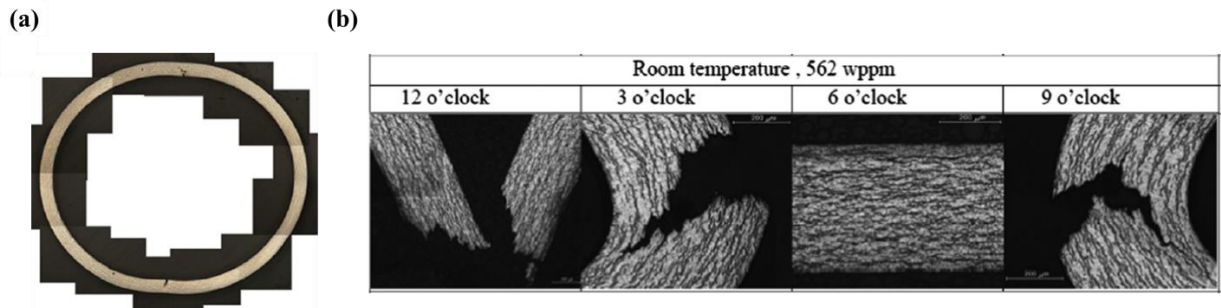


Figure 36. Fracture of a hydrided zircaloy-4 specimen with high hydrogen concentration after ring compression tests, (a) brittle fracture with cracks at vertical spots, (b) hydride morphology and crack development at different spots [35].

Figure 37 (a, c) depict the FEM predicted crack profile from different view for a specimen with hydrogen content of 500 wppm. The FEM model predicts that cracks will initiate on the inner surface of vertical spots at early deformation stage. The crack is also a semi-elliptical surface crack with major axis along the axial direction. As deformation keeps growing, cracks also start to appear on the outer surface of horizontal spots. Finally, cracks are developed at all 4 spots. This result agrees with experimental observations.

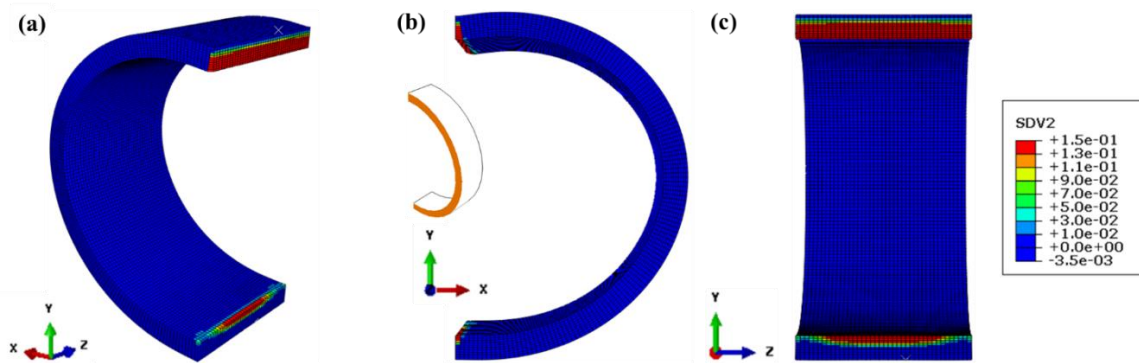


Figure 37. FEM predicted crack profile for a specimen with hydrogen concentration of 500 wppm, crack initiate on the inner surface at spot 2 and 4.

Both experimental results and FEM predictions illustrate that the crack initiation spot strongly relates to the hydrogen concentration of the specimen. For specimens with low hydrogen concentration and high ductility, the crack initiates on the outer surface at horizontal

spots (spot 1 and 3). While, for specimen with high hydrogen concentration and low ductility, the crack initiates on the inner surface at vertical spots (spot 2 and 4) at early deformation stage. Such results indicate that the inner surface at vertical spots may have higher stress at early deformation stage. A FEM simulation was performed to study the pressure ratio change between the horizontal and vertical spots during the ring compression test. Figure 38 (a) shows the two points picked for analysis. Point 1 is on the outer surface at spot 1. Point 2 is on the inner surface at spot 2. Elastoplastic material property without damage was used for this model. Figure 38 (b) depicts the pressure ratio  $P_2/P_1$  as a function of the displacement. It clearly shows that the pressure at point 2 is much higher than point 1 at early deformation stage. However, as the deformation goes, the difference between pressure at point 1 and 2 reduces. When the displacement gets larger than 4mm, the pressure ratio becomes smaller than 1, which indicates the pressure at point 1 becomes larger than the pressure at point 2. This result explains the relation between the hydrogen concentration and crack initiation spot of the ring specimen.

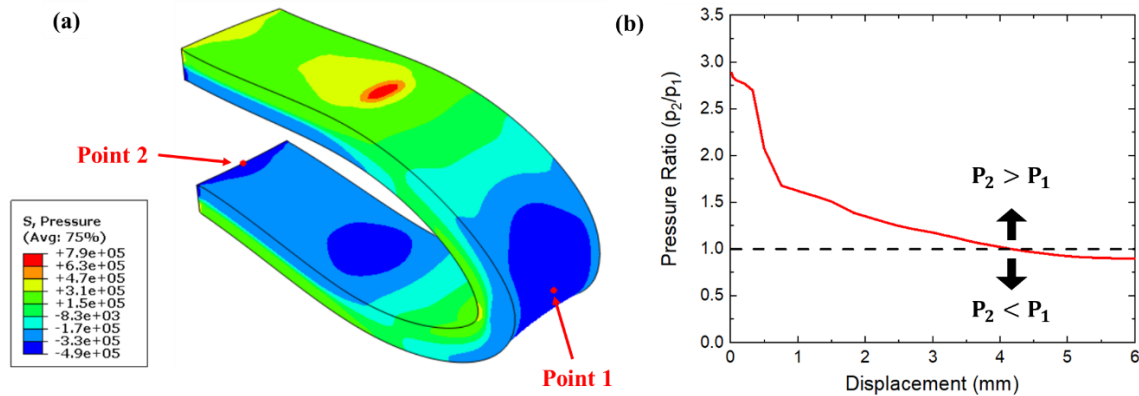


Figure 38. (a) FEM model and points selected for pressure ratio analysis, (b) the pressure ratio ( $P_2/P_1$ ) as a function of the displacement.

### 3.5 Conclusions

In this work, the extended GTN model [11, 25] was chosen as the micro-mechanical model to study the fracture behavior of hydrided zircaloy-4 structures. This model accounts the damage effects from both precipitate debonding in zircaloy matrix and hydride cracking [15]. The extended GTN model was implemented into ABAQUS via the user defined subroutine UMAT for ABAQUS/Standard. The subroutine was developed based on the backward Euler integration

algorithm proposed by Aravas [18] and Zhang et al. [31]. The validation of the subroutine was checked by comparing the FEM results with the numerical integrated analytical solutions.

The model was further used to study the fracture behavior of hydrided zircaloy-4 structures under axial tensile tests and ring compression tests. 3D FEM models were created to perform the analysis. The simulations satisfactorily reproduced experimental stress-strain/load-displacement curves. Furthermore, the model successfully predicted the width reduction and the hydride cracking porosity at the fracture surface in axial tensile tests. Good agreement between calculated and experimental results was also achieved for crack initiation prediction in ring compression tests.

It's worth to notice that this model only correctly describes the effect of hydrides which are parallel to the tensile direction, for instance circumferential hydrides under the hoop tension condition. The fracture mechanism in radial hydrides (hydride platelets which are perpendicular to the loading direction) is different. Instead of only cracking through the thickness, the micro-cracks will propagate along hydride length direction and generate larger cracks. In future works, the model needs to be further modified to capture such anisotropic growth of micro-cracks.

### 3.6 References

1. Arsene, S. and J. Bai, *A new approach to measuring transverse properties of structural tubing by a ring test*. Journal of testing and evaluation, 1996. **24**(6): p. 386-391.
2. Arsène, S., *Effet de la microstructure et de la température sur la transition ductile-fragile des zircaloy hydrures*. 1997, Châtenay-Malabry, Ecole centrale Paris.
3. Martin-Rengel, M., F.G. Sánchez, J. Ruiz-Hervías, L. Caballero, and A. Valiente, *Revisiting the method to obtain the mechanical properties of hydrided fuel cladding in the hoop direction*. Journal of Nuclear Materials, 2012. **429**(1-3): p. 276-283.
4. Rico, A., M. Martin-Rengel, J. Ruiz-Hervias, J. Rodriguez, and F. Gomez-Sanchez, *Nanoindentation measurements of the mechanical properties of zirconium matrix and hydrides in unirradiated pre-hydrided nuclear fuel cladding*. Journal of nuclear materials, 2014. **452**(1-3): p. 69-76.
5. Bertolino, G., G. Meyer, and J.P. Ipina, *Effects of hydrogen content and temperature on fracture toughness of Zircaloy-4*. Journal of Nuclear Materials, 2003. **320**(3): p. 272-279.

6. Rashid, J., *Spent fuel transportation applications-Assessment of cladding performance: A synthesis report*. EPRI Report, 2007. **1015048**.
7. Rashid, J., M. Rashid, R. Dunham, and A. Machiels, *Failure criteria for Zircaloy cladding using a damage-based metal/hydride mixture model*. EPRI, Palo Alto, CA, 2004. **1009693**.
8. Rashid, J., M. Rashid, A. Machiels, R. Dunham, and P.A. EPRI, *A new material constitutive model for predicting cladding failure*. Proceedings of Top Fuel, 2009: p. 6-10.
9. Udagawa, Y., T. Mihara, T. Sugiyama, M. Suzuki, and M. Amaya, *Simulation of the fracture behavior of Zircaloy-4 cladding under reactivity-initiated accident conditions with a damage mechanics model combined with fuel performance codes FEMAXI-7 and RANNS*. Journal of Nuclear Science and Technology, 2014. **51**(2): p. 208-219.
10. Chen, Q., J.T. Ostien, and G. Hansen, *Development of a used fuel cladding damage model incorporating circumferential and radial hydride responses*. Journal of Nuclear Materials, 2014. **447**(1-3): p. 292-303.
11. Gurson, A.L., *Continuum theory of ductile rupture by void nucleation and growth. Part I. Yield criteria and flow rules for porous ductile media*. 1975, Brown Univ., Providence, RI (USA). Div. of Engineering.
12. Grange, M., J. Besson, and E. Andrieu, *An anisotropic Gurson type model to represent the ductile rupture of hydrided Zircaloy-4 sheets*. International Journal of Fracture, 2000. **105**(3): p. 273-293.
13. Williams, B., S. St Lawrence, and B. Leitch, *Comparison of the measured and predicted crack propagation behaviour of Zr-2.5 Nb pressure tube material*. Engineering Fracture Mechanics, 2011. **78**(18): p. 3135-3152.
14. Cockeram, B. and K. Chan, *In situ studies and modeling of the deformation and fracture mechanism for wrought Zircaloy-4 and Zircaloy-2 as a function of stress-state*. Journal of Nuclear materials, 2013. **434**(1-3): p. 97-123.
15. Le Saux, M., J. Besson, and S. Carassou, *A model to describe the mechanical behavior and the ductile failure of hydrided Zircaloy-4 fuel claddings between 25° C and 480° C*. Journal of Nuclear Materials, 2015. **466**: p. 43-55.
16. Chen, W.-F. and D.-J. Han, *Plasticity for structural engineers*. 2007: J. Ross Publishing.
17. Dunne, F. and N. Petrinic, *Introduction to computational plasticity*. 2005: Oxford University Press on Demand.

18. Aravas, N., *On the numerical integration of a class of pressure-dependent plasticity models*. International Journal for numerical methods in engineering, 1987. **24**(7): p. 1395-1416.
19. Zhang, Z., *Explicit consistent tangent moduli with a return mapping algorithm for pressure-dependent elastoplasticity models*. Computer methods in applied mechanics and engineering, 1995. **121**(1-4): p. 29-44.
20. Zhang, Z., C. Thaulow, and J. Ødegård, *A complete Gurson model approach for ductile fracture*. Engineering Fracture Mechanics, 2000. **67**(2): p. 155-168.
21. Simo, J.C. and T.J. Hughes, *Computational inelasticity*. Vol. 7. 2006: Springer Science & Business Media.
22. Simo, J.C. and R.L. Taylor, *Consistent tangent operators for rate-independent elastoplasticity*. Computer methods in applied mechanics and engineering, 1985. **48**(1): p. 101-118.
23. Arun, S., *Finite element modelling of fracture and damage in austenitic stainless steel in nuclear power plant*. 2015.
24. Chu, C. and A. Needleman, *Void nucleation effects in biaxially stretched sheets*. Journal of engineering materials and technology, 1980. **102**(3): p. 249-256.
25. Tvergaard, V. and A. Needleman, *Analysis of the cup-cone fracture in a round tensile bar*. Acta metallurgica, 1984. **32**(1): p. 157-169.
26. Le Saux, M., J. Besson, S. Carassou, C. Poussard, and X. Averty, *Behavior and failure of uniformly hydrided Zircaloy-4 fuel claddings between 25 C and 480 C under various stress states, including RIA loading conditions*. Engineering Failure Analysis, 2010. **17**(3): p. 683-700.
27. Gologanu, M., J.-B. Leblond, and J. Devaux, *Approximate models for ductile metals containing non-spherical voids—case of axisymmetric prolate ellipsoidal cavities*. Journal of the Mechanics and Physics of Solids, 1993. **41**(11): p. 1723-1754.
28. Puls, M., *Fracture initiation at hydrides in zirconium*. Metallurgical transactions A, 1991. **22**(10): p. 2327-2337.
29. Puls, M.P., *The effect of hydrogen and hydrides on the integrity of zirconium alloy components: delayed hydride cracking*. 2012: Springer Science & Business Media.
30. Abaqus, V., *6.14 Documentation*. Dassault Systemes Simulia Corporation, 2014. **651**.

31. Zhang, Z. and E. Niemi, *A class of generalized mid-point algorithms for the Gurson–Tvergaard material model*. International Journal for Numerical Methods in Engineering, 1995. **38**(12): p. 2033-2053.
32. Bron, F. and J. Besson, *Simulation of the ductile tearing for two grades of 2024 aluminum alloy thin sheets*. Engineering Fracture Mechanics, 2006. **73**(11): p. 1531-1552.
33. Rousselier, G., *Ductile fracture models and their potential in local approach of fracture*. Nuclear engineering and design, 1987. **105**(1): p. 97-111.
34. Grange, M., J. Besson, and E. Andrieu, *Anisotropic behavior and rupture of hydrided Zircaloy-4 sheets*. Metallurgical and Materials Transactions A, 2000. **31**(3): p. 679-690.
35. Kim, J.-S., T.-H. Kim, D.-H. Kook, and Y.-S. Kim, *Effects of hydride morphology on the embrittlement of Zircaloy-4 cladding*. Journal of Nuclear Materials, 2015. **456**: p. 235-245.
36. Garrison, B.E., *Failure Properties and Phenomena for Zircaloy-4 from Ring Compression Testing*. 2018.

## CHAPTER 4. CONCLUSION

The main objective of this work is performing a combined experimental and computational investigation to study the thermomechanical properties of zircaloy-4. Three different experimental methods were used to measure thermomechanical properties : (1) the extended Raman thermometry method for microstructure dependent thermal conductivity measurements of zircaloy-4, (2) nanoindentation experiment for measurements of quasi-static elastoplastic constitutive relations of zircaloy hydride at various temperatures, (3) dynamic nano-scale impact experimental measurements for fitting a viscoplastic constitutive model of zircaloy hydride at various temperatures. FEM simulations were used to obtain the true effective stress-strain relation from nanoindentation experiments and predict the fracture strength of zircaloy hydride. The ductile to brittle transition in hydrided zircaloy structures has also been investigated. An extended GTN model was used to study the fracture behavior of hydrided zircaloy structures at macro-scale. The key findings from the present study are summarized below.

1. Raman thermometry has been extended to the thermal conductivity measurement of metallic samples through the use of a thin silicon coating on samples to provide measurable Raman signals. A heat transfer model was derived to relate the substrate thermal conductivity to the laser induced temperature increase on the silicon coating surface. Combining this heat transfer model with the Raman thermometry method, the thermal conductivity of zircaloy-4 measured in this study was found to range from 11-13  $\text{Wm}^{-1}\text{K}^{-1}$ , which is close to literature reported values ranging from 12~15  $\text{Wm}^{-1}\text{K}^{-1}$ . The small difference may be due to the thermal resistance at the interface between the silicon coating and the substrate, which is not considered in current heat transfer model.
2. The microstructure of zircaloy-4 samples were characterized by using SEM. LIGs were identified based on grain structures (parallel platelets or basketweave grains). The experimental observation shows LIGs with larger mean true spacing have slightly higher thermal conductivity values. This can be induced by the thermal resistance of GB and inhomogeneous composition/impurity distribution. This trend is consistent with the prediction of the Kapitza resistance model that a larger grain size will lead to a higher thermal conductivity in polycrystalline materials.

3. A power law viscoplasticity model was established based on nanoindentation and nano-scale impact dataset to represent the plastic behavior of  $\delta$ -phase zircaloy hydride. Both the strength coefficient (K) and the strain hardening exponent (n) of  $\delta$ -hydride decrease as temperature increasing. This implies the softening behavior of hydride at elevated temperatures. The strain rate exponent (m) of hydride remains almost as a constant as temperature goes up to 300°C. The observed trend indicates the lack of change in ductility of hydrides at high temperatures.
4. Combining the proposed viscoplastic constitutive model of  $\delta$ -hydride and FEM simulations, by reproducing the global tensile fracture stress reported in literature, the fracture strength of  $\delta$ -hydride was predicted. The fracture strength of  $\delta$ -hydride decreases linearly with temperature increasing, and there is no rapid change near the ductile to brittle transition temperature range (150°C~200°C). Therefore, the fracture strength change of  $\delta$ -hydride is not the root cause of the ductile to brittle transition of hydrided zircaloy structures.
5. The variation of yield stress difference between hydride and zircaloy matrix can be a plausible reason for the ductile to brittle transition of hydrided zircaloy structures. The FEM calculated strain energy ratio shows the plastic deformation of zircaloy matrix dominates the deformation of the hydrided zircaloy structure at high temperatures, which could reduce the tensile stress buildup and cracking in hydride precipitates.
6. The extended GTN model was used to study the fracture behavior of hydrided zircaloy structures at macro-scale. This model accounts the damage effects from both precipitate debonding in zircaloy matrix and hydride cracking. The model was implemented into ABAQUS via the user defined subroutine UMAT for ABAQUS/Standard. The 3D FEM simulations satisfactorily reproduced experimental stress-strain/load-displacement curves in both axial tensile tests and ring compression tests. Furthermore, the model successfully predicted the width reduction and the hydride cracking porosity at the fracture surface in axial tensile tests. Good agreement between calculated and experimental results was also achieved for crack initiation prediction in ring compression tests.

## CHAPTER 5. FUTURE WORKS

The present research has brought forth a better understanding of the thermomechanical properties of zircaloy-4. A key contribution of the current work has been that new experimental methods and FEM models have been established and developed to study the microstructure dependent thermomechanical properties of materials. However, there are still few limitations in current study. Some proposed improvements and future works are summarized below:

1. In current study, isotropic material properties for both zircaloy and hydride are assumed. In future study, combining the EBSD measured grain orientation and nano-mechanical experimental methods, anisotropic viscoplastic constitutive relations can be established for both phases.
2. Due to the small size of hydride precipitates, only 0.7  $\mu\text{m}$  indenter was used. Therefore, tests with only two strain rates were performed. In future works, indenter with larger tip radius can be used to perform tests at more strain rates.
3. The modified GTN model only correctly describes the effect of hydrides which are parallel to the tensile direction, for instance circumferential hydrides under the hoop tension condition. In future works, the model needs to be further modified to capture the growth of micro-cracks in radial hydrides.
4. The modified GTN model needs to be further developed to account anisotropic material properties in the hydrided zircaloy structures. In order to account for the plastic anisotropy of the material, the von Mises equivalent stress can be replaced by the Hill equivalent stress in the Gurson yield function.

## APPENDIX A. PARTIAL DERIVATIVES FOR GTN MODEL

Define an intermedia variable  $\beta$  as,

$$\beta = \frac{3q_2p}{2\sigma_f}$$

The partial derivatives for the GTN model are,

$$\frac{\partial\phi}{\partial p} = \frac{3q_1q_2f^*}{\sigma_f} \sinh\beta$$

$$\frac{\partial^2\phi}{\partial p^2} = \frac{9q_1q_2^2f^*}{2\sigma_f^2} \cosh\beta$$

$$\frac{\partial\phi}{\partial q} = \frac{2q}{\sigma_f^2}$$

$$\frac{\partial^2\phi}{\partial q^2} = \frac{2}{\sigma_f^2}$$

$$\frac{\partial^2\phi}{\partial p \partial q} = 0$$

$$\frac{\partial^2\phi}{\partial p \partial \Delta\varepsilon_{eq}^m} = -\frac{3q_1q_2f^*\sigma_f'}{\sigma_f^2} (\sinh\beta + \beta \cosh\beta)$$

$$\frac{\partial^2\phi}{\partial q \partial \Delta\varepsilon_{eq}^m} = -\frac{4q}{\sigma_f^3} \sigma_f'$$

$$\frac{\partial^2\phi}{\partial p \partial \Delta f} = \frac{3q_1q_2}{\sigma_f} \frac{df^*}{df} \sinh\beta$$

$$\frac{\partial^2\phi}{\partial q \partial \Delta f} = 0$$

$$\frac{\partial\phi}{\partial \Delta\varepsilon_{eq}^m} = -\frac{\sigma_f'}{\sigma_f^2} \left( \frac{2q^2}{\sigma_f} + 3q_1q_2f^*p \sinh\beta \right)$$

$$\frac{\partial\phi}{\partial \Delta f} = 2 \frac{df^*}{df} (q_1 \cosh\beta - q_3f^*)$$

$$\frac{\partial \Delta\varepsilon_{eq}^m}{\partial \varepsilon_{eq}^m} = \frac{p\Delta\varepsilon_p - q\Delta\varepsilon_q}{(1-f)\sigma_f^2} \sigma_f'$$

$$\frac{\partial \Delta f}{\partial \varepsilon_{eq}^m} = A + A' \Delta\varepsilon_{eq}^m$$

$$\frac{\partial \Delta\varepsilon_{eq}^m}{\partial f} = \frac{-p\Delta\varepsilon_p + q\Delta\varepsilon_q}{(1-f)^2\sigma_f^2}$$

$$\frac{\partial \Delta f}{\partial f} = -\Delta\varepsilon_p$$

$$\frac{\partial \Delta\varepsilon_{eq}^m}{\partial p} = -\frac{\Delta\varepsilon_p}{(1-f)\sigma_f}$$

$$\frac{\partial \Delta f}{\partial p} = 0$$

$$\frac{\partial \Delta\varepsilon_{eq}^m}{\partial q} = \frac{\Delta\varepsilon_q}{(1-f)\sigma_f}$$

$$\frac{\partial \Delta f}{\partial q} = 0$$

$$\frac{\partial \Delta\varepsilon_{eq}^m}{\partial \Delta\varepsilon_p} = -\frac{p}{(1-f)\sigma_f}$$

$$\frac{\partial \Delta f}{\partial \Delta\varepsilon_p} = 1 - f$$

$$\frac{\partial \Delta \varepsilon_{eq}^m}{\partial \Delta \varepsilon_q} = \frac{q}{(1-f)\sigma_f}$$

$$\frac{\partial \Delta f}{\partial \Delta \varepsilon_q} = 0$$

## APPENDIX B. COEFFICIENTS FOR EQUATIONS (83) AND (84)

Defining two intermediate variables P and Q as,

$$P = \frac{\partial \phi}{\partial q}$$

$$Q = \frac{\partial \phi}{\partial p}$$

Then, other coefficients can be given as,

$$A_{11} = P + \Delta \varepsilon_p \left( K \frac{\partial P}{\partial p} + \frac{\partial P}{\partial H_1} \frac{\partial H_1}{\partial \Delta \varepsilon_p} + \frac{\partial P}{\partial H_2} \frac{\partial H_2}{\partial \Delta \varepsilon_p} \right) + \Delta \varepsilon_q \left( K \frac{\partial Q}{\partial p} + \frac{\partial Q}{\partial H_1} \frac{\partial H_1}{\partial \Delta \varepsilon_p} + \frac{\partial Q}{\partial H_2} \frac{\partial H_2}{\partial \Delta \varepsilon_p} \right),$$

$$A_{12} = Q + \Delta \varepsilon_p \left( -3G \frac{\partial P}{\partial q} + \frac{\partial P}{\partial H_1} \frac{\partial H_1}{\partial \Delta \varepsilon_q} + \frac{\partial P}{\partial H_2} \frac{\partial H_2}{\partial \Delta \varepsilon_q} \right) + \Delta \varepsilon_q \left( -3G \frac{\partial Q}{\partial q} + \frac{\partial Q}{\partial H_1} \frac{\partial H_1}{\partial \Delta \varepsilon_q} + \frac{\partial Q}{\partial H_2} \frac{\partial H_2}{\partial \Delta \varepsilon_q} \right),$$

$$A_{21} = K \frac{\partial \phi}{\partial p} + \frac{\partial \phi}{\partial H_1} \frac{\partial H_1}{\partial \Delta \varepsilon_p} + \frac{\partial \phi}{\partial H_2} \frac{\partial H_2}{\partial \Delta \varepsilon_p},$$

$$A_{22} = -3G \frac{\partial \phi}{\partial q} + \frac{\partial \phi}{\partial H_1} \frac{\partial H_1}{\partial \Delta \varepsilon_q} + \frac{\partial \phi}{\partial H_2} \frac{\partial H_2}{\partial \Delta \varepsilon_q},$$

$$b_1 = -\Delta \varepsilon_p P - \Delta \varepsilon_q Q,$$

$$b_2 = -\phi.$$

where

$$\frac{\partial H_1}{\partial \Delta \varepsilon_p} = w_{11} \left[ \frac{\partial h_1}{\partial \Delta \varepsilon_p} + K \frac{\partial h_1}{\partial p} \right] + w_{12} \left[ \frac{\partial h_2}{\partial \Delta \varepsilon_p} + K \frac{\partial h_2}{\partial p} \right],$$

$$\frac{\partial H_2}{\partial \Delta \varepsilon_p} = w_{21} \left[ \frac{\partial h_1}{\partial \Delta \varepsilon_p} + K \frac{\partial h_1}{\partial p} \right] + w_{22} \left[ \frac{\partial h_2}{\partial \Delta \varepsilon_p} + K \frac{\partial h_2}{\partial p} \right],$$

$$\frac{\partial H_1}{\partial \Delta \varepsilon_q} = w_{11} \left[ \frac{\partial h_1}{\partial \Delta \varepsilon_q} - 3G \frac{\partial h_1}{\partial q} \right] + w_{12} \left[ \frac{\partial h_2}{\partial \Delta \varepsilon_q} - 3G \frac{\partial h_2}{\partial q} \right],$$

$$\frac{\partial H_2}{\partial \Delta \varepsilon_q} = w_{21} \left[ \frac{\partial h_1}{\partial \Delta \varepsilon_q} - 3G \frac{\partial h_1}{\partial q} \right] + w_{22} \left[ \frac{\partial h_2}{\partial \Delta \varepsilon_q} - 3G \frac{\partial h_2}{\partial q} \right],$$

$$w_{11} = \Omega^{-1} \left( \delta_{22} - \frac{\partial h_2}{\partial H_2} \right),$$

$$w_{12} = \Omega^{-1} \left( \frac{\partial h_1}{\partial H_2} \right),$$

$$w_{21} = \Omega^{-1} \left( \frac{\partial h_2}{\partial H_1} \right),$$

$$w_{22} = \Omega^{-1} \left( \delta_{11} - \frac{\partial h_1}{\partial H_1} \right),$$

$$\Omega = \left( \delta_{11} - \frac{\partial h_1}{\partial H_1} \right) \left( \delta_{22} - \frac{\partial h_2}{\partial H_2} \right) - \left( \delta_{21} - \frac{\partial h_2}{\partial H_1} \right) \left( \delta_{12} - \frac{\partial h_1}{\partial H_2} \right).$$

**APPENDIX C. COEFFICIENTS FOR EQUATIONS (98) AND (99)**

$$\bar{A}_{11} = P + \Delta\varepsilon_p \left( \frac{\partial P}{\partial H_1} \frac{\partial H_1}{\partial \Delta\varepsilon_p} + \frac{\partial P}{\partial H_2} \frac{\partial H_2}{\partial \Delta\varepsilon_p} \right) + \Delta\varepsilon_q \left( \frac{\partial Q}{\partial H_1} \frac{\partial H_1}{\partial \Delta\varepsilon_p} + \frac{\partial Q}{\partial H_2} \frac{\partial H_2}{\partial \Delta\varepsilon_p} \right),$$

$$\bar{A}_{12} = Q + \Delta\varepsilon_p \left( \frac{\partial P}{\partial H_1} \frac{\partial H_1}{\partial \Delta\varepsilon_q} + \frac{\partial P}{\partial H_2} \frac{\partial H_2}{\partial \Delta\varepsilon_q} \right) + \Delta\varepsilon_q \left( \frac{\partial Q}{\partial H_1} \frac{\partial H_1}{\partial \Delta\varepsilon_q} + \frac{\partial Q}{\partial H_2} \frac{\partial H_2}{\partial \Delta\varepsilon_q} \right),$$

$$\bar{A}_{21} = \frac{\partial \phi}{\partial H_1} \frac{\partial H_1}{\partial \Delta\varepsilon_p} + \frac{\partial \phi}{\partial H_2} \frac{\partial H_2}{\partial \Delta\varepsilon_p},$$

$$\bar{A}_{22} = \frac{\partial \phi}{\partial H_1} \frac{\partial H_1}{\partial \Delta\varepsilon_q} + \frac{\partial \phi}{\partial H_2} \frac{\partial H_2}{\partial \Delta\varepsilon_q},$$

$$B_{11} = \frac{\Delta\varepsilon_p}{3} \left( \frac{\partial P}{\partial p} + \frac{\partial P}{\partial H_1} \frac{\partial H_1}{\partial p} + \frac{\partial P}{\partial H_2} \frac{\partial H_2}{\partial p} \right) + \frac{\Delta\varepsilon_q}{3} \left( \frac{\partial Q}{\partial p} + \frac{\partial Q}{\partial H_1} \frac{\partial H_1}{\partial p} + \frac{\partial Q}{\partial H_2} \frac{\partial H_2}{\partial p} \right),$$

$$B_{12} = -\Delta\varepsilon_p \left( \frac{\partial P}{\partial q} + \frac{\partial P}{\partial H_1} \frac{\partial H_1}{\partial q} + \frac{\partial P}{\partial H_2} \frac{\partial H_2}{\partial q} \right) - \Delta\varepsilon_q \left( \frac{\partial Q}{\partial q} + \frac{\partial Q}{\partial H_1} \frac{\partial H_1}{\partial q} + \frac{\partial Q}{\partial H_2} \frac{\partial H_2}{\partial q} \right),$$

$$B_{21} = \frac{1}{3} \left( Q + \frac{\partial \phi}{\partial H_1} \frac{\partial H_1}{\partial p} + \frac{\partial \phi}{\partial H_2} \frac{\partial H_2}{\partial p} \right),$$

$$B_{22} = - \left( P + \frac{\partial \phi}{\partial H_1} \frac{\partial H_1}{\partial q} + \frac{\partial \phi}{\partial H_2} \frac{\partial H_2}{\partial q} \right).$$

Here,

$$\frac{\partial H_1}{\partial \Delta\varepsilon_p} = w_{11} \left( \frac{\partial h_1}{\partial \Delta\varepsilon_p} \right) + w_{12} \left( \frac{\partial h_2}{\partial \Delta\varepsilon_p} \right),$$

$$\frac{\partial H_1}{\partial \Delta\varepsilon_q} = w_{11} \left( \frac{\partial h_1}{\partial \Delta\varepsilon_q} \right) + w_{12} \left( \frac{\partial h_2}{\partial \Delta\varepsilon_q} \right),$$

$$\frac{\partial H_2}{\partial \Delta\varepsilon_p} = w_{21} \left( \frac{\partial h_1}{\partial \Delta\varepsilon_p} \right) + w_{22} \left( \frac{\partial h_2}{\partial \Delta\varepsilon_p} \right),$$

$$\frac{\partial H_2}{\partial \Delta\varepsilon_q} = w_{21} \left( \frac{\partial h_1}{\partial \Delta\varepsilon_q} \right) + w_{22} \left( \frac{\partial h_2}{\partial \Delta\varepsilon_q} \right),$$

$$\frac{\partial H_1}{\partial p} = w_{11} \left( \frac{\partial h_1}{\partial p} \right) + w_{12} \left( \frac{\partial h_2}{\partial p} \right),$$

$$\frac{\partial H_1}{\partial q} = w_{11} \left( \frac{\partial h_1}{\partial q} \right) + w_{12} \left( \frac{\partial h_2}{\partial q} \right),$$

$$\frac{\partial H_2}{\partial p} = w_{21} \left( \frac{\partial h_1}{\partial p} \right) + w_{22} \left( \frac{\partial h_2}{\partial p} \right),$$

$$\frac{\partial H_2}{\partial q} = w_{21} \left( \frac{\partial h_1}{\partial q} \right) + w_{22} \left( \frac{\partial h_2}{\partial q} \right),$$

## APPENDIX D. COEFFICIENTS FOR EQUATIONS (100) AND (101)

$$C_{11} = [(\bar{A}_{22} + 3GB_{22})B_{11} - (\bar{A}_{12} + 3GB_{12})B_{21}]/\Delta,$$

$$C_{12} = [(\bar{A}_{22} + 3GB_{22})B_{12} - (\bar{A}_{12} + 3GB_{12})B_{22}]/\Delta,$$

$$C_{21} = [(\bar{A}_{11} + 3KB_{11})B_{21} - (\bar{A}_{21} + 3KB_{21})B_{11}]/\Delta,$$

$$C_{22} = [(\bar{A}_{11} + 3KB_{11})B_{22} - (\bar{A}_{21} + 3KB_{21})B_{12}]/\Delta,$$

$$\Delta = (\bar{A}_{11} + 3KB_{11})(\bar{A}_{22} + 3GB_{22}) - (\bar{A}_{12} + 3GB_{12})(\bar{A}_{21} + 3KB_{21}).$$

## PUBLICATIONS

1. **Wang H**, Okuniewski M, Tomar V. Constitutive Modeling of Zircaloy Hydride Based on Strain Rate Dependent Nanoindentation and Nano-Scale Impact Dataset. (Under preparation)
2. **Wang H**, Okuniewski M, Tomar V. *Microstructure Dependent Thermal Conductivity Measurement of Zircaloy-4: Extended Raman Thermometry Method*. (Under preparation)
3. **Wang H**, Tomar V. *Damage Modeling of Hydrided Structure Based on Extended Gurson-Tvergaard-Needleman Model*. (Under preparation)
4. Parakash C, **Wang H**, Dhiman A, Tomar V. *In-Situ Measurement of Dynamic Stress Due To Hyper-Velocity Impact*. (Under preparation)
5. **Wang H**, Dhiman A, Ostergaard H E, *et al*. *Nanoindentation based properties of Inconel 718 at elevated temperatures: A comparison of conventional versus additively manufactured samples*[J]. International Journal of Plasticity, 2019.
6. **Wang H**, Biswas S, Han Y, *et al*. *A phase field modeling based study of microstructure evolution and its influence on thermal conductivity in polycrystalline tungsten under irradiation*[J]. Computational Materials Science, 2018, 150: 169-179.
7. Biswas S, Schwen D, **Wang H**, *et al*. *Phase field modeling of sintering: Role of grain orientation and anisotropic properties*. Computational Materials Science, 2018, 148: 307-319.
8. Mao K, **Wang H**, Wu Y, *et al*. *Microstructure-property relationship for AISI 304/308L stainless steel laser weldment*[J]. Materials Science and Engineering: A, 2018, 721: 234-243.
9. Zhang Y, **Wang H**, Tomar V. *Visualizing stress and temperature distribution during elevated temperature deformation of IN-617 using nanomechanical Raman spectroscopy*[J]. Jom, 2018, 70(4): 464-468.
10. Mohanty D P, **Wang H**, Okuniewski M, *et al*. *A nanomechanical Raman spectroscopy based assessment of stress distribution in irradiated and corroded SiC*[J]. Journal of Nuclear Materials, 2017, 497: 128-138.